UNIVERSITÀ DEGLI STUDI DI PADOVA

Department of Physics and Astronomy
MSc Physics

gDM bounds - A portal to handle experimental limits on particle dark matter searches

Supervisor:
Prof. Michele Doro

Co-supervisor:
Dr. Giacomo D'Amico

Candidate:
Michela De Caria

ACADEMIC YEAR 2023/2024

[...]
signora Libertà,
signorina Anarchia.

ACKNOWLEDGEMENTS

Over the past three long years, I never thought I would find this much love and support. Im truly happy to be here, and fittingly, ending up where I didnt begin, just as real physicians do: they explore and venture further, curious but never lost, because they know how to learn, read, and create maps. I am deeply indebted to Professor Michele Doro for teaching me this invaluable skill. I've learned so much from you that I could fill this entire page. Thank you for introducing me to these fascinating topics, which we can broadly call dark matter research. I believe this is what Ill dedicate the rest of my life to. Thank you for your advice, your belief in me, and most of all, your patience.
A special thank you to Giacomo D'Amico. I have great admiration for your work, and I truly appreciate all the help you gave me with the final results of this thesis. But most of all, I value your sense of humor, you always made me laugh during our gamma lunches.

Words cannot express my gratitude to my family. Mum and dad, you are my examples. I learned a lot from you too. Thank you for all the words of support you gave me in these years, for all the hugs and for all the sacrifice you did for me. I couldn't wish better parents. To my sister Gaia, my lioness. I love you, thank you for always making me smile. You are my lighthouse and my best friend, and with you by my side, I know Ill be drowning in tears of laughter. And to my (not anymore) little brother Francesco. I love you from the bottom of my heart. Thank you for being here for me, with your wise and your original point of view. Thanks for making me laugh and proud of you every day.
I want to say thank you to all the member of my family, for being here not physically but always caring for me and for my well being.
A special and important thank you is for Zia Mary. You are my second mum, as you are being there for me since the day 0. Our long chats were and are always like honey when you have sore throat. Thanks for all the advices, all the laughs and for your unconditional faith in me. Zio Rocco and Zio Brunello, a important thanks is for you too. I know that if I'll be in danger I have to call you. But now I know how to do by myself, you taught me.

I found my second family here in Padova. I owe a big thank you to my amie Nicole and Sara. You know everything. This past year without you would have been a total mess, full of tears. I think I should get you lot of spritz! Youre my best friends, and Ill stop here before we all drown in a sticky pot of sweetness and "eeew". Thanks to Federico Testagrossa, Fede. You were always there, with your thoughtful advice, genuine care, and unique sense of humor. If I'm here today is also for you. Piters, my dear. Thank you for the birrette at your place, the little adventures and our small trips around Ferrara, thanks for all the joy I feel whenever I'm with you.
A special place in my heart is for the young gamma aperitivo group's past and present members. You are the best group of the world. You encouraged me every time, making me feel exactly like if I'm at home. I will miss all the "pausa?" or "lunch 12:45?" messages. In the little moments like these I thought I found a special group of friend first and then colleagues. Thanks. I need to report special

instruction from Davide which, in my opinion, is a really important tuition for my future: "*Daje, daje e daje, la cipolle divende aje*" (for the italian version I suggest you to write an email to Davide: *davide.miceli1993@gmail.com*).

I express my sincerely gratitude also to my friend Mattia: I am happy to say I could always count on you. Thanks for all the walks around Padova, our long and precious talks were something I will always cherish in my heart. Anna and Concetta, thanks for being two of my dearest friend: our summer walks and our breakfast club are always a certainty. I want also to do an important thank you for Marty and Mattia: in these months I got closer to you, discovering two people with whom I could share funny moments, as well as deep conversations. You made my last summer better.

My final thank you, as always, goes to my grandmother. From your blue armchair, you shared all your wisdom with me. I always hope to make you proud as I admire and map this vast, strange, and unknown Universe, for both of us, through my blue glasses.

EXECUTIVE SUMMARY

The principal objective of this thesis is to contribute to the development of the `gDMbounds` project led by Prof. M. Doro. This portal is a valuable resource for studying dark matter (DM) annihilation and decay, providing researchers with predictions and tools to explore new aspects of DM interactions.

My work began by utilizing the *CosmiXs* model to calculate the predicted photon count, denoted as N_γ, from DM annihilation. Focusing on the γ-ray spectrum, I compared it to results from the earlier *PPPC4DMID* model. This study allowed me to identify key differences in the predictions of the two models, highlighting how advances in our understanding of DM physics can refine the expected signals that we aim to observe in experimental data. These constraints are essential for limiting the range of parameters and interactions that DM can exhibit, as determined by current experimental data. The final stage of the thesis involved revisiting the *PPPC4DMID* model to explore its predictive capabilities for DM particle interactions, particularly in terms of the energy spectrum $\frac{dN}{dE}$. By leveraging these predictions, I worked to extend the features of the `gDMbounds` platform. The primary goal was to develop a methodology for predicting one annihilation channel based on another channel that has already been observed and published. For instance, starting with data for the $b\bar{b}$ annihilation channel, I aimed to project the behavior of the $\tau^+\tau^-$ channel. This process involved comparing results across multiple experiments, gradually expanding the study to include all known annihilation channels and a wider range of experimental data. Additionally, I performed a detailed analysis of the telescopes' effective area to evaluate their sensitivity and ability to detect faint signals, which was critical for accurately converting the intrinsic flux predictions into real fluxes.

Finally, I want to point out that this research not only contributes to the specific objectives of the `gDMbounds` project. It also aims to add to the broader scientific understanding of DM interactions, by offering new insights into how theoretical models can be constrained and extended. Hence, the motivation for this study is to explore new possibilities for DM behavior, refine existing models, and provide clear limits that contribute to the wider research on DM interactions, focusing on two different aspects: firstly, it explores different ways in which DM can annihilate, going beyond already known channels. DM may interact in ways that are not yet fully understood, potentially leading to observable phenomena in various experiments. Predicting these "other channels" is critical to broaden our understanding of DM interactions and open new opportunities for detection. Secondly, this work establishes constraints on theoretical models, especially those involving specific interactions (or mixing) between different annihilation channels. Each DM model has its own characteristics and specific predictions about its behavior. Setting these limits helps exclude certain parameters based on experimental data, narrowing down the theories and guiding future research.

SOMMARIO ESECUTIVO

L'obiettivo principale di questa tesi è contribuire allo sviluppo del progetto `gDMbounds` del Prof. M. Doro. Questo portale è una risorsa preziosa per lo studio dell'annichilazione e del decadimento della materia oscura (DM), fornendo ai ricercatori previsioni e strumenti per esplorare nuovi aspetti delle interazioni della DM.

Il mio lavoro è iniziato utilizzando il modello *CosmiXs* per calcolare il numero previsto di fotoni, indicato come N_γ, provenienti dall'annichilazione della DM. Concentrandomi sullo spettro dei raggi γ, ho confrontato i risultati con quelli del precedente modello *PPPC4DMID*. Questo studio mi ha permesso di identificare le principali differenze tra le previsioni dei due modelli, evidenziando come i progressi nella comprensione della fisica della DM possano affinare i segnali attesi. Questi vincoli sono essenziali per limitare il range di parametri e interazioni che la DM può presentare, come determinato dai dati sperimentali attuali.
Nella fase finale, tramite il modello *PPPC4DMID*, ho esplorato le capacità predittive sulle interazioni delle particelle di DM, in particolare in termini di spettro energetico $\frac{dN}{dE}$. Sfruttando queste previsioni, ho lavorato per estendere le funzionalità della piattaforma `gDMbounds`. L'obiettivo principale era sviluppare una metodologia per prevedere un canale di annichilazione a partire da un altro canale già osservato e pubblicato. Ad esempio, partendo dai dati per il canale di annichilazione $b\bar{b}$, ho cercato di proiettare il comportamento del canale $\tau^+\tau^-$. Questo processo ha coinvolto il confronto dei risultati tra diversi esperimenti, ampliando gradualmente lo studio per includere altri canali di annichilazione conosciuti e un'ampia gamma di dati sperimentali. Inoltre, ho eseguito un'analisi dettagliata dell'area effettiva dei telescopi per valutarne la sensibilità e la capacità di rilevare segnali deboli, fattore fondamentale per convertire accuratamente le previsioni di flusso intrinseco in flussi reali.

Infine, desidero sottolineare che questa ricerca non solo contribuisce agli obiettivi specifici del progetto `gDMbounds`, ma mira anche ad ampliare la comprensione scientifica delle interazioni della DM, offrendo nuove intuizioni su come i modelli teorici possano essere vincolati ed estesi. Pertanto, la motivazione di questo studio è esplorare nuove possibilità di comportamento della DM, affinare i modelli esistenti e fornire limiti chiari che contribuiscano alla ricerca più ampia sulle interazioni della DM, concentrandosi su due aspetti principali: in primo luogo, esplora modi diversi in cui la DM può annichilirsi, andando oltre i canali già noti. Predire questi "altri canali" è cruciale per ampliare la nostra comprensione delle interazioni della materia oscura e aprire nuove opportunità di rilevazione. In secondo luogo, questo lavoro stabilisce vincoli sui modelli teorici, in particolare quelli che coinvolgono interazioni specifiche tra diversi canali di annichilazione. Ogni modello di DM ha le sue caratteristiche e previsioni specifiche e stabilire questi limiti aiuta a escludere determinati parametri sulla base di dati sperimentali, restringendo le possibili teorie e guidando la direzione delle ricerche future.

TABLE OF CONTENTS

Chapter 1
INTRODUCTION

The nature of Dark Matter (DM) is one of the fundamental open questions in the modern physics research. To date, we genuinely don't known its microscopic composition nor its coupling to ordinary matter so that we truly infer the existence of DM via its gravitational manifestation exclusively. There is substantial evidence showing that DM does not interact through the electromagnetic force. If it did, electromagnetic friction would have caused it to gather in the same regions as ordinary matter. Additionally, by examining galactic rotation curves, we've determined that DM is distributed around galaxies in the form of a spherical halo.

One of the most compelling pieces of evidence for the interacting behavior of dark matter, and its existence, comes from the measurement of spatial anisotropies in the Cosmic Microwave Background (CMB). These measurements were first observed by the COBE satellite, refined by WMAP, and most precisely measured by the Planck satellite. [1]. CMB is the microwave radiation that permeates the Universe and it corresponds to the Last Scattering Surface (LSS) which happened during *Recombination Epoch* in the history of the Universe. This occurred $\sim$380,000 years after the Big Bang, marking the last significant interaction between baryonic matter and DM. Certainly, the composition of Universe in that epoch influenced the scale of anisotropies: models that consider only gravitational interactions, i.e. collisionless, match the observed data perfectly, while any friction interaction would cause significant discrepancies.

Planck detector measurements successfully determine the energy composition of today's Universe. By analyzing the matter configuration at the recombination epoch and extrapolating it to the present day, it yield the following values [1]:

$$\Omega_{\mathrm{DM}} h^2 = \frac{\rho_{\mathrm{DM}}}{\rho_{\mathrm{crit}}} = 0.1198 \pm 0.0012, \tag{1.1}$$

$$\Omega_{\mathrm{SM}} h^2 = 0.02233 \pm 0.00015, \tag{1.2}$$

where $\rho_{\mathrm{crit}} = \frac{3H_0^2}{8\pi G} = 10^{-6}\,\mathrm{GeV\,cm^{-3}}$ is the critical density, G is the Newton gravitational constant and $h = 10^{-2} H_0\,\mathrm{km\,s^{-1}\,Mpc^{-1}} = 0.6737 \pm 0.0054$ is the reduced Hubble parameter at redshift zero. Hence nearly the 27% the total energy density of the Universe is DM and the total amount of Universe's mass, namely the 85% is dark.

In the following chapter we will see firstly DM historical experimental evidences; in the second part we will discuss DM the most suitable density profiles, while in the third and last section we will explore some of the most known DM candidates.

1.1 DM Storical Experimental Evidences

The evidence of DM originated from astrophysical observations, across different scales: cluster scales, galactic scales, and cosmological (horizon) scales.
The "classic" proof of DM's existence comes from the F. Zwicky's study (1933) [2] on the dispersion velocity of Coma Cluster's galaxies, where he observed that its gravitational mass was at least 500 times greater than the luminous mass, leading to the so called *"Missing Mass Problem"*. This breakthrough was supported by the seminal work of astronomers Vera Rubin and Kent Ford in 1970, as documented in their influential paper [3], and later confirmed by A. Bosma's study in 1981 [4]. Bosma's research focused specifically on the H I distribution across several galaxies, examining where the gas is concentrated, how its density varies across different regions, and the velocity at which this gas moves. These observations are crucial for understanding galactic rotation and mass distribution. Both studies corroborated the earlier conclusions of Fritz Zwicky, showing that the observed velocity dispersion was far too large to be accounted for by luminous matter alone.
Additional compelling marks for the existence of DM has been provided by various sources: strong lensing (Tyson, Kochanski, DellAntonio 1998) and weak lensing (Refregier 2003), observations of hot gas in galaxy clusters (Lewis, Buote and Stocke 2003), the study of the Bullet Cluster (Clowe et al. 2006). Furthermore, from a cosmological point of view, we have insights from Big Bang nucleosynthesis (BBN) (Fields, Sarkar 2008), large scale structure constraints (Allen et al. 2003), and, as already cited, measurements of CMB's anisotropies (Komatsu et al. 2010).
We will go deeper into the three primary historical pieces of evidence for the existence of DM: the missing mass problem together with the galaxy rotation curves, the gravitational lensing, and we will see further the imprint of DM on the CMB's spectrum.

1.1.1 The Missing Mass Problem

The observation of Coma Cluster's galaxies revealed that the dispersion velocities of stars remain constant, or even increase, at distances far from the galactic center, contrary to what would be expected if only visible matter were present. This discrepancy is correlated with the mass of clusters thanks to the virial theorem. In fact we can estimate the mass of galaxy clusters by relating the kinetic energy (which can be measured through the velocities) to the gravitational potential energy of clusters. Zwicky found that the mass inferred visible matter was greatly exceed those which would be expected by summing the masses of all the cluster galaxies. The outcome strongly suggesting the presence of DM: this is the *missing mass problem*.
The determination of the masses of galaxy clusters relies on the assumption that they are bound, self-gravitating systems. If these clusters were not gravitationally bound, they would quickly disperse. We assume firstly that cluster distribution is spherical and stationary and, of course, that galaxies are held together by gravity, so that one limit on the mass of clusters comes from the binding condition:

$$2 < K > + < U >= 0 \tag{1.3}$$

Figure 1.1: Coma Cluster optical emission ($z = 0.0231$). Credit: Optical: SDSS.

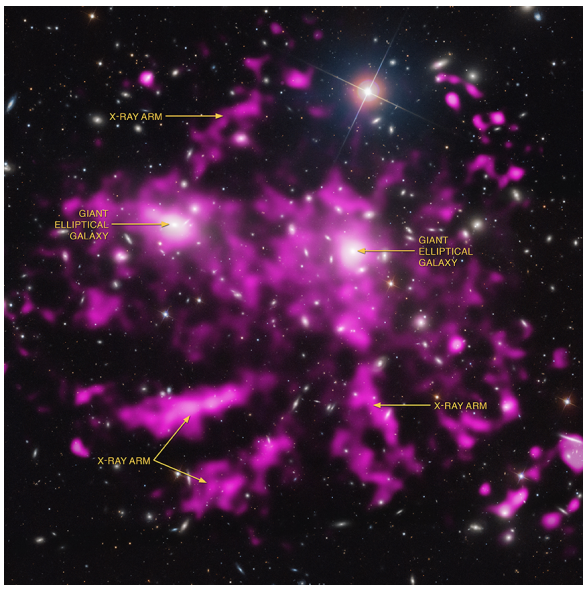

Figure 1.2: A composite image of Coma Cluster.
Credit: X-ray: NASA/CXC/MPE/J.Sanders et al, Optical: SDSS.

where $< K >= \frac{1}{2} M_{tot} \sigma^2$ is the kinetic energy of the cluster: σ is the mass-weighted radial dispersion velocity, and M_{tot} is the measurable (or visible) mass; while $U = -\alpha G \frac{M_{tot} M}{R_m}$ is the potential (attractive) energy, where $\alpha = \frac{3}{5}$ is a numerical factor and it reflects how the mass is spread out in the cluster and R_m refers to the median radius of the distribution of radii within the cluster.[1] Combining these two in (1.3) we obtain the average galaxy's mass:

$$M = \frac{\sigma^2 R_m}{\alpha G} = 7.0 \times 10^{14} M_\odot \left(\frac{\sigma}{1000 \text{ km/s}} \right)^2 \left(\frac{R_m}{\text{Mpc}} \right). \tag{1.4}$$

Here we assumed $\sigma \sim 1000$km/s and $R_m \sim 1 Mpc$, while historically Zwicky estimated that the number of galaxies contained in Coma Cluster was 1000 within a radius of $r \sim 2 \times 10^6$ light years, whereas the observed velocity dispersion was $\sigma \sim 700$km/s. He obtained a conservative lower limit (excluding galaxies with recession velocity of 5100km/s) of $4.5 \times 10^{13} M_\odot$ on the mass of the cluster corresponding to an average mass-per-galaxy of $4.5 \times 10^{10} M_\odot$. Assuming then an average absolute luminosity for cluster galaxies of 8.5×10^7 of the Sun's luminosity, Zwicky showed that this led to a surprisingly high mass-to-light ratio of about 500.[2]. Cluster analyses reveal surprisingly high masses compared to their luminosity, with mass-to-light ratios in solar units ranging from 1 to 12, with only around 10% of the cluster mass being visible in the light of the galaxies. Observations of diffuse light in clusters, like Coma, show that such light is not sufficient to account for a large increase in the mass-to-light ratio. Thus this is a considerable direct and indirect evidence for invisible matter.

[1] We are assuming that the positions of galaxies and the orientation of their velocity vectors are uncorrelated.

[2] The most accurate of these determinations involve comparing numerical or analytical models for the galaxy distribution in a cluster with the observed spatial and velocity distributions ([5], [6], [7])

1.1.2 Galactic Rotation Curves

In the chapter IV part B of [8], the authors use the expression "*the 1970s Revolution*" to make a reference at Kent Ford and Vera Rubin's work on the observations of rotation curves of galaxies. Indeed, after Zwicky's studies of 1933 and 1937 on Coma Cluster and the S. Smith's calculations on Virgo Cluster mass-to-light ratio (1936), the scientific community experienced a period of confusion where *the DM hypothesis was not commonly accepted, nor was it disregarded* [8]. It is in this moment that radioastronomers developed an image tube spectrograph, used to perform spectroscopic observations of the Andromeda Galaxy (M31). By measuring the Doppler shift of the spectra produced by HII regions and assuming circular motion, they obtained the velocity dispersion rotation curve and they noticed that at large radii the velocity dispersion remained approximately constant. This did not agree with the theoretical expectations.

We have to do a step backward. The rotation curves of galaxies is the circular velocity profile of the stars and gas in a galaxy, as a function of their distance from the galactic center. Stars rarely collide so their motion is dictated by just their gravitational interactions. If we consider a self-gravitating spherical galaxy, the centripetal force that keeps the star in orbit must be equal to the gravitational attraction force due to the mass distribution inside a sphere of radius r (i.e. the system is virialized); hence, from standard Newtonian gravity, the circular velocity is:

$$v_c(r) = \sqrt{\frac{GM(r)}{r}} \tag{1.5}$$

As we can notice that $v_c \propto r^{-1/2}$: if we consider the mass as formed by only the visible matter, for distances beyond the Galactic disk $r \geq R_{disk}$, Gauss Law tells us that $M(r) \sim const$ (assuming all the baryonic mass is concentrated in the disk); while $r \leq R_{disk}$, the mass would increase as $M \sim r^3$. The resulting rotational velocity curve increases linearly with the radius inside the disk and then decreases as the square root of the radius outside the disk.

The remarkable work [9] led by V. Rubin observed that circular velocity distribution, instead, had behaviour in opposition to the one just mentioned: there is a "flattening" of the curves for $r \geq R_{disk}$ so that $v_c \sim const$ and therefore $M(r) \sim r$. Various other studies, like [4] (1981) by A. Bosma and [10] (1985) by T.S. van Albada showed the very same accurate result. Since then, further evidence has continued to strengthen these conclusions as we can see in [11]: the Fig. 1.3 shows the rotation curve of NGC 3198 spiral galaxy, where the red dots are the actual velocity of its outer parts and the line denoted as disk are the expected velocity. A DM halo is necessary to substain the velocity in the outer parts.

Finally, we can obtain an order-of-magnitude estimate for the mass and size scale of the Milky Ways DM halo. Previously we assumed that the DM has a spherically symmetric distribution[3] shape centered around the Galaxy in contrast to the baryonic matter, which is concentrated in the disk. Here-

[3] Why a spherical halo? Since DM particles interact only weakly with each other and therefore, not dissipating energy through friction, they do not collapse inside the disk, forming spherical halos; on the contrary, the baryons dissipate energy through electromagnetic friction.

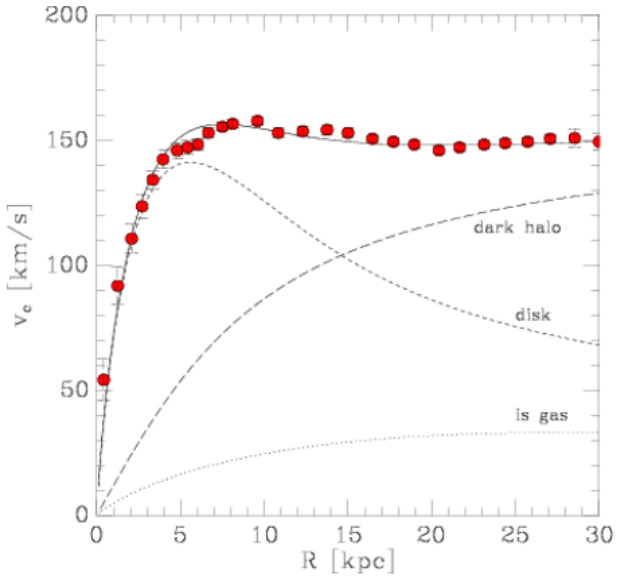

Figure 1.3: Maximum disk decomposition of the rotation curve of NGC 3198. The contributions due to the stellar disk, the interstellar gas, and the dark halo are indicated. Credit: [11].

after, the DM density distribution assumes the form:

$$\rho(r) = \frac{M(r)}{r^3} \sim \frac{1}{r^2}. \tag{1.6}$$

From stellar kinematics we have an estimation of $M_{halo} \sim 10^{12} M_{\odot}$ and the local DM density $\rho_0 \sim 0.3$ GeV/cm^3 and so from:

$$M_{halo} \sim 4\pi \int_0^{R_{halo}} dr r^2 \rho(r), \tag{1.7}$$

we obtain a rough calculation of $R_{halo} \sim 100$kpc, that indicates that the DM halo extends out an order of magnitude beyond the baryonic disk.

1.1.3 Gravitational Lensing

Gravitational lensing occurs when light from a distant source, such as a galaxy or star, passes near a massive object, like a galaxy cluster or a black hole, on its way to Earth. This massive object acts as a lens, bending and distorting the light. This effect can lead to image distortion, where the distant object may appear stretched, elongated, or even duplicated and sometimes, if the alignment is just right, the distorted image can form circular or arc-like patterns.

In 1970 Fritz Zwicky proposed that galaxy clusters could also act as gravitational lenses due to their massive size. This has been confirmed through observations of structures like the Bullet Cluster (in the Fig. 1.4): it is a merging galaxy cluster 1E0657-558 which consists of two primary galaxy concentrations separated by about $0.72 Mpc$. Looking at X-ray emission plasma from both subclusters, we can notice that on the western side a prominent bow shock (the bullet), indicating that the smaller one is moving away at $\sim 4700 km/s$ from the main cluster. In the article [12] Clowe and its colleagues showed that since the line of sight velocity component between these two is $\sim 600 km/s$, the cores

passed through each other $\sim 100 Myr$ ago. During a merger of two clusters, the X-ray emitting plasma dissipates energy because of the baryonic friction, and tends to agglomerate, in contrast with galaxies, who behave as collisionless particles. DM does not interact with the plasma in the same way as ordinary matter so it was not slowed by the impact. Therefore, during the collision the DM clumps from the two clusters moved ahead of the hot gas, producing the separation of the dark and normal matter. This results in a discrepancy between the visible mass (dominated by X-ray plasma) and the gravitational potential.

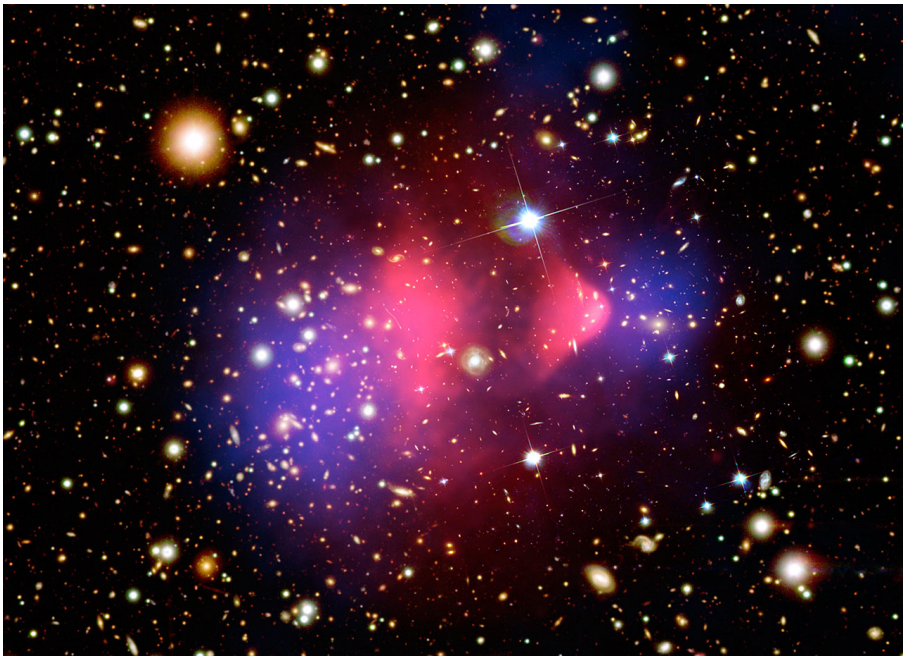

Figure 1.4: Composite image of the Bullet Cluster. Most of the matter in the clusters (blue) is clearly separate from the hot gas (visible in X-ray as a reddish-pink glow). Credit: X-ray: NASA/CXC/CfA/M.Markevitch, Optical and lensing map: NASA/STScI, Magellan/U.Arizona/D.Clowe, Lensing map: ESO WFI.

1.1.4 DM Signatures in the CMB

As already revealed, we can detect the presence of DM from the spectrum of the CMB. Its existence was predicted by G. Gamow in 1948 and it was actually discovered in 1965 by phycisians A. Penzias and R. Wilson., as the excess antenna temperature which, within the limits of their observations, was isotropic, unpolarized, and free from seasonal variations; they measured a temperature excess of $\sim 3.5 \pm 1.0 K$. Today we know from [13] that the cosmic radiation has a nearly perfect blackbody spectrum in the microwave, with a temperature of:

$$T = 2.7255 \pm 0.0006 \mathrm{K}, \tag{1.8}$$

and this corresponds to 410 photons per cubic centimeter or to the flux of 10 trillion photons per second per squared centimeter.

To gain a clearer understanding of the origins of the CMB, we will qualitatively examine the Standard

Cosmological Model, which describes the evolution of the Universe since the Big Bang.
Initially, the Universe was filled with a primordial plasma, characterized by thermodynamic equilibrium and high temperatures kept all particles relativistic, undergoing continuous expansion. To maintain equilibrium with this expanding fluid, the interaction rates (Γ_i) of the various particles had to be sufficiently high to overshoot the expansion rate of the Universe (i.e. Hubble parameter H). As the Universe expands, its temperature decreases, making some reactions less likely and reducing interaction rates. This results in $\Gamma_i < H$ causing the i-particles to decouple (or freeze-out) from the fluid and cease to interact efficiently with it. At an energy of approximately $0.26eV$(redshift $z_{ls} = 1000$), during the *recombination* era, electrons that survived annihilation begin to recombine with atomic nuclei (mainly protons and α particles). This process decreases the interaction rate between radiation and matter, making it less than the rate of the Universe's expansion. Consequently, photons start traveling freely through space, having escaped the last scattering surface. This freedom of travel gives the CMB its nearly perfect blackbody spectrum and provides valuable information about the last interactions between matter and photons.
However the CMB exhibits intrinsic tiny temperature fluctuactions, the *anisotropies*, (in different patches of the sky - to 1 part in 100,000) in its angular distribution, which are characterized by a power spectrum, as illustrated in the Fig. 1.5. These anisotropies correspond to regions of slightly different densities, representing the seeds of all future structure i.e. the stars and galaxies of today.

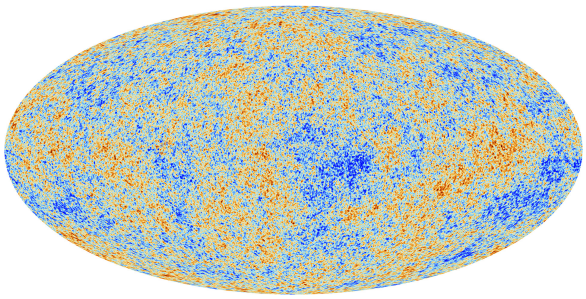

Figure 1.5: Sky map of primordial temperature fluctuations in Galactic coordinates. Credit: l'ESA.

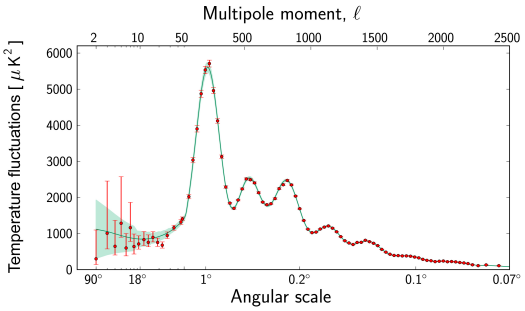

Figure 1.6: The power spectrum of the CMB. The Multipole moment l is proportionally inverse to θ, the polar angle i.e. the angular scale; on the y-axis is the power spectrum, which is the quadratic average of the coefficients of the harmonic spherical decomposition of the temperature fluctuations. Credit: l'ESA.

The functional form of the CMB power spectrum is very sensitive to both the various cosmological parameters and to the shape, strength and nature of primordial fluctuations. The peaks in this power spectrum, known as *acoustic peaks*, are the result of sound waves traveling through the primordial plasma, creating regions of varying density. The graph 1.6 shows large angular scales of ninety degrees on the left and progresses to smaller scales on the right. The multipole moments corresponding to these angular scales are marked at the top of the graph. The red dots represent

Planck measurements, with error bars that account for measurement uncertainties becoming more pronounced at larger angular scale. The green curve on the graph shows the best fit of the 'standard cosmological model', while the pale green shading around the curve indicates the range of predictions from variations of the model that align with the data. While the observations at small and intermediate angular scales are in excellent agreement with the model predictions, the data at large angular scales (between 90 and 6 degrees) show fluctuations approximately 10% weaker than those predicted by the cosmological model. Here it comes DM: it influences cosmic structure formation through its gravitational effects, affecting the density distribution and gravitational potential. In turn it modifies the propagation of acoustic waves in the early Universe, shifting and altering the height of the acoustic peaks in the CMB spectrum: high DM presence tends to move peaks to smaller scales and affects their amplitude.

1.2 DM density profiles

The evolution of cosmic structures from primordial density fluctuations is influenced by various physical processes, such as gas dynamics, radiative cooling, and photoionization. Comparing theoretical predictions with the observed Universe, where dissipative effects are significant, adds complexity.
N-body simulations are a key tool for studying structure formation, evolving DM from initial conditions while incorporating effects like gas dynamics and radiative transfer. However, accurately simulating all baryonic effects, such as star formation, feedback processes, and the detailed interaction between baryons and DM, remains challenging and is not always fully captured in these simulations. The reliability of N-body simulations depends on mass and length resolution. Mass resolution is determined by the smallest particle mass considered, while length resolution is limited by the softening scale to avoid infinities in gravitational force.
Recent simulations suggest a universal and general DM density profile (though results vary) it is the Zhao-Hernquist profile and it has this shape:

$$\rho(r) = \rho_0 \left(\frac{r}{R}\right)^{-\gamma} \left[1 + \left(\frac{r}{R}\right)^{\alpha}\right]^{\frac{\gamma-\beta}{\alpha}} \tag{1.9}$$

where r is the distance from DM halo center, R and ρ_0 are called scale radius and they are caracteristic of DM density and α, β, γ are free parameters. Different profile models and their parameters are listed in Table 1.1.

Table 1.1: Parameters for various DM density profile models.

Model	α	β	γ	R (kpc)
Kravtsov et al. (Kra)	2.0	3.0	0.4	10.0
Navarro, Frenk, and White (NFW)	1.0	3.0	1.0	20.0
Moore et al. (Moore)	1.5	3.0	1.5	28.0
Isothermal (Iso)	2.0	2.0	0	3.5

Another profile that describes a cuspy innermost halo is the Einasto profile:

$$\rho(r) = \rho_0 \exp\left(-\frac{2}{\alpha}\left[\left(\frac{r}{R}\right)^{\alpha} - 1\right]\right). \tag{1.10}$$

It is characterized by a peak for small radii.

In contrast, observations of dwarf spheroidal galaxies (dSphs) suggest a different profile, known as the Burkert profile, which shows a density plateau in the inner halo (it is what is called "core" profile):

$$\rho(r) = \rho_0 \left[\frac{1}{1+\frac{r}{R}}\left(1+\frac{r^2}{2R^2}\right)\right]. \tag{1.11}$$

Another flat-profile variant similar to the Burkert profile is the pseudo-isothermal profile:

$$\rho(r) = \rho_0 \left[1+\left(\frac{r}{R}\right)^2\right]^{-1} \tag{1.12}$$

These profiles are illustrated in Fig. 1.7, showing the distinction between "cusp" and "core" profiles, which are important for understanding the central density distribution of DM halos.

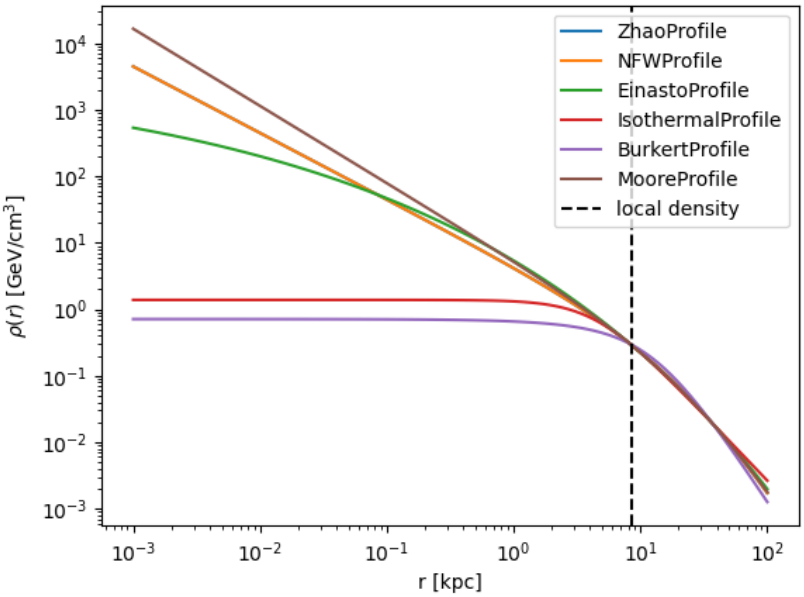

Figure 1.7: Comparison of different DM density profiles: NFW, Einasto, Burkert, Moore and pseudo-isothermal. They were obtain using *gammapy* [14].

1.3 Particle DM Candidates

The evidence for DM primarily relies on its gravitational interactions. However, since gravity is a universal force, this evidence does not specifically reveal the nature of DM. Understanding the identity of DM is crucial for several reasons: in astrophysics, it affects how cosmic structures form and influences the Universes past and future evolution, while in particle physics, DM is a major indicator of

potential new particles and might be connected to unresolved questions of Particle Physics Standard Model (PPSM). There are numerous frameworks beyond PPSM the ranging from well-established theories to more speculative ideas, that include plausible DM candidate particles. However, we can deduce some general model-independent remarks about the allowed mass range for DM halo. For this purpose, it is worth mentioning the TASI Lectures by M. Lisanti [15], which provide a concise overview of both the upper and lower limits for DM masses.

The most general lower bound is known as the *Tremaine-Gunn Bound* [16], which is derived under the assumption that DM is a fermion, and thus obeys Fermi-Dirac statistics. Nonetheless, the conclusion is that DM cannot be composed of low-mass fermions. This is because the Pauli exclusion principle (or *Pauli blocking effect* [17]) restricts the number of such particles in a given phase space. If the individual particle mass is too low, the total mass will be insufficient to produce the necessary gravitational effects. Indeed, according to the exclusion principle, on average each volume of phase space can contain no more than one fermionic particle:

$$M_{halo} = m_{DM} V \int d^3 p f(p) \lesssim m_{ferm} V \int d^3 p \sim m_{ferm} R_{halo}^3 (m_{ferm} v)^3, \tag{1.13}$$

where the $V_{halo} = 4/3\pi R_{halo}^3$ is the usual spherical shape. Then, substituting in the virial velocity:

$$m_{DM} \gtrsim (G^3 M_{halo} R_{halo}^3)^{-1/8}, \tag{1.14}$$

where a narrow constraint follows from phase-space densities of dwarf galaxies: $m_{DM} \gtrsim 0.7 keV$.

Conversely if, for instance, DM consists of ultra-light scalar particles, Bose statistics allows for an unlimited number of particles to occupy the same phase space point. In this scenario, the high occupation number means the DM can be treated as a classical field. In this way it is deduced the lower bound on DM mass. The most stringent constraints arise from halos around dwarf galaxies, leading to an estimate that an ultra-light scalar DM particle must have a mass $m_{DM} \gtrsim 10^{-21} eV$. Ultra-light scalar DM particles near this lower limit are referred to as "*fuzzy*" DM.

The Cowsik-McClelland bound [18] is the most general upper bound on the DM mass. It is derived from a simple cosmological requirement, by ensuring that their contribution to the overall energy density of the Universe does not exceed the observed value. If DM particles were significantly heavier than this bound, their number density would be too low to account for the observed DM abundance without exceeding the Universe's critical density.

The number density of a non relativistic DM particles n_χ is given by:

$$n_\chi \sim \frac{g_\chi T^3}{\pi^2} \left(\frac{m_\chi}{T}\right)^{3/2} e^{-m_\chi/T}, \tag{1.15}$$

where g_χ is the number of internal degrees of freedom of the DM particle, T is the temperature of the Universe at freeze-out and m_χ is the mass of the DM particle.

Now we defined previously the relic abundance of DM, Ω_χ, as:

$$\Omega_\chi h^2 = \frac{\rho_\chi}{\rho_{crit}} h^2 = \frac{m_\chi n_\chi}{\rho_{crit}} h^2, \tag{1.16}$$

where we recognize $\rho_\chi = m_\chi n_\chi$ as the energy density of DM, ρ_{crit} as the critical density of the Universe and h as the dimensionless Hubble parameter.
Substituting the expression for n_χ, we get:

$$\Omega_\chi h^2 \sim \frac{g_\chi T^3}{\pi^2} \left(\frac{m_\chi}{T}\right)^{3/2} e^{-m_\chi/T} \frac{m_\chi}{\rho_c} h^2 \tag{1.17}$$

The requirement that $\Omega_\chi h^2 \leq 0.1198$ (the observed DM abundance we saw in the eq.(1.1)) gives us:

$$m_\chi \lesssim \frac{T}{\left(\frac{\pi^2 \rho_c}{g_\chi T^3 h^2}\right)^{2/3}} e^{m_\chi/T} \Rightarrow m_\chi \lesssim \text{few MeV}, \tag{1.18}$$

in the limit where the temperature T is small compared to the mass m_χ (where the exponential factor dominates).

1.3.1 General properties of DM

We will summarize the necessary microscopic properties[4] of the DM particle before going through a more detailed discussion of some of the most compelling or popular candidates. Stronger constraints on the properties of DM particle aspirants typically arise from two key requirements: DM relics must have been produced in the early Universe and they must exhibit the correct density i.e. the eq. (1.1).
Dusting off the Standard Cosmological Model, we can give a general classification for DM particle candidates is hot, warm, or cold (HDM, WDM, CDM) based on their relativistic properties at the time of decoupling in the early Universe. HDM particles were relativistic with temperatures on the order of eV, while CDM particles were non-relativistic (NR) with temperatures on the order of GeV. WMD falls in between, with temperatures and properties reflecting a combination of these characteristics, depending on their production mechanisms, such as thermal freeze-out or other processes.
After the decoupling of photons the pressure they provided was missing so, due to fluctuations in density, the first structures started to aggregate, giving the birth to "*hierarchical clustering formation*". The way they will appear depends, of course, on the particle DM's velocity:

- in the case of HDM, since we have a relativistic particle, it would kill the density fluctuations on scale smaller than super clusters. Only when it becomes non relativistic the matter aggregation can begin, following a top-down process, with structures on the scale of clusters forming first in flat sheets and later by their fragmentation and instabilities also smaller scale structures as galaxies could begin to form; an example of this class is neutrino. HDM particles, due to their high velocities, have a large free-streaming length that would result in overly diluted DM clustering, contradicting observations;

[4] Although slightly dated, it is worth mentioning the review by M. Taoso et al. [19], which provides a comprehensive *ten-point test* to constrain DM candidates based on experimental results.

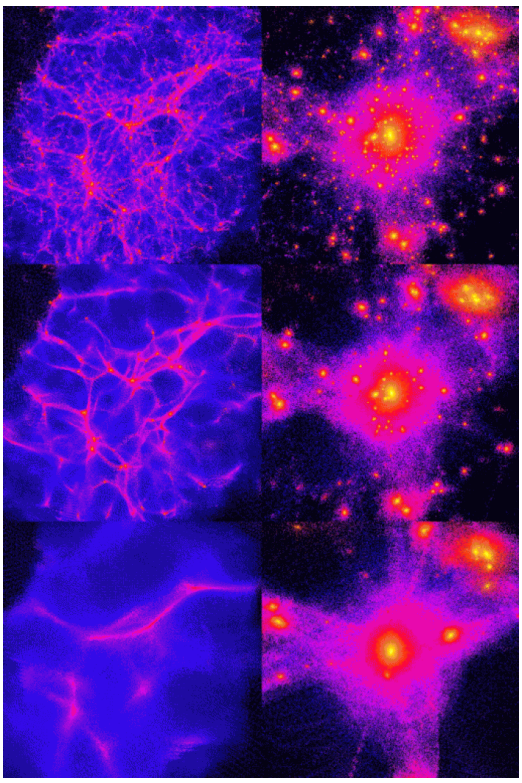

Figure 1.8: From the top simulations of CMD (WIMPs), WMD (mostly CDM with some neutrinos as well) HDM (neutrinos). In the left panel we are in early times redshift; in right one we have the very same structure but at present time $(z = 0)$. Small scale structures are predominant in the CDM scenario and lacks in the HDM scenario. Credit Ben Moore, University of Zurich.

- in the case of CDM, since the particle is not relativistic, the small scale density fluctuations are not dumped and structures began forming hierarchically (bottom up process), with small scale structures forming first and then, by the process of clustering, began to assemble into larger scale systems. This is the process which led to the formation of DM halos; these then attracted the baryonic matter which, collapsing, lost energy through dissipative processes leading to formations of stars an gas clouds; the most important representative are neutralino and Kaluza-Klein state(WIMPs); there are other particles behaving as CDM but, due to their non thermal origin, are less massive: they are called axions;

- in the case of WDM, it can be said that they are particles with masses around keV scale and one of the candidates is gravitino $\tilde{G}$.

This argument well describes both the Large Scale Structure we observe and the CMB density fluctuations: a simulation can be seen in the Fig. 1.8.
Hence, generally speaking, we search for **CDM** which has to be **non baryonic matter**, due to CMB properties; nevertheless this does not impose overly strict constraints on the possible forms of interactions of DM particles, it does imply that DM particles must be **electrically neutral**. If they were not, they would emit photons and thus become detectable. To cite [20], we are searching for "*invisible matter*". Commonly, at least, some 90% of DM **does not dissipate** its energy. Therefore, DM particles should also be either absolutely **stable**, or extremely long lived (a recent analysis finds a

lower bound of at least 160 Gyr). Finally the DM should interact with gravity and in principle could talk also with ordinary PPSM matter preferably only weakly, where weak may stand for the familiar weak force, or instead some other (sub)weak force defined by some non-negligible coupling to SM particles; of course such interactions do not involve emission of photons, otherwise DM halos would shine and be visible. DM particles could also interact with themselves, if of the order at most of the strong interaction, so of the order of the MeV.

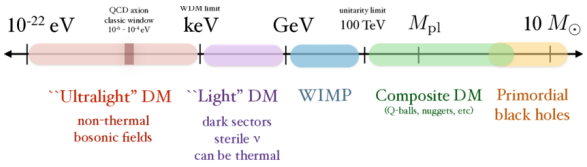

(a) The approximate mass range of allowed DM candidates, comprising both particle candidates and primordial black holes. Credit: [21]

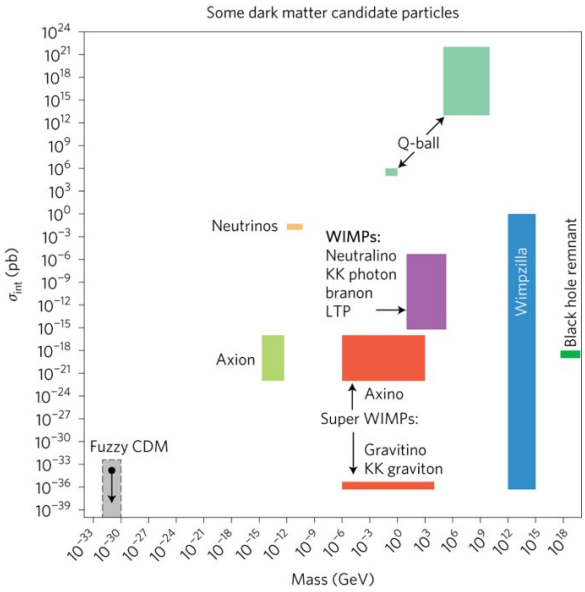

(b) Proposed particle candidates for dark DM span more than 60 orders of magnitude in cross-section and about 45 orders of magnitude in mass. Credit: [22].

Figure 1.9: Overview of particle DM candidates.

Fig. 1.9 offers an overview of the DM particle candidates that will be explored in the following sections, with a particular emphasis on the class of WIMPs. For a comprehensive summary of DM particle candidates, their properties, and the motivations behind them, see Table 1 in [23]. Following the terminology used by G. Bertone et al. [24], let's explore the *Non-Baryonic Candidate Zoo*.

1.3.2 WIMPs

The WIMP framework has long been favored, as it naturally emerges in many extensions of the PPSM that deal with the *hierarchy problem*, while also offering a straightforward explanation for the observed relic abundance through the so-called "WIMP miracle". WIMPs have masses in the range $m_{DM} \sim 10GeV - TeV$ and tree-level interactions with the W and Z gauge bosons but, of course, not with gluons or photons.

We have already qualitatively introduced the *freeze-out* mechanism for DM production. This process is quantitatively driven by the the Boltzmann equation:

$$\frac{dn_\chi}{dt} + 3Hn_\chi = - < \sigma v > (n_\chi^2 - n_{\chi,eq}^2), \tag{1.19}$$

where n is the number density of the DM particle indicated by the Greek letter χ, $<\sigma v>$ is the thermally averaged self-annihilation cross section and finally $n_{\chi,eq}$ is the number density in thermal equilibrium. For the derivation of 1.19 I refer you to Appendix A.
In the right side of eq. 1.19, the $<\sigma v>$ accounts for dilution from expansion, while the n_χ^2 term arises from processes $\chi\chi \to SMSM$ that destroy DM particles and the $n_{\chi,eq}^2$ term arises from the reverse process $SMSM \to \chi\chi$, which creates DM particles. The thermal relic density is determined by solving the Boltzmann equation numerically, however we can roughly discuss what happens. The non-relativistic ($T \lesssim m_\chi$) number density of a given particle species, i.e. the eq. (1.15), depends on the Universe's composition and temperature. It decreases exponentially, stropping when the particle self-annihilation rate drops below the Hubble expansion rate (freeze-out process). For particles at the GeV scale, freeze-out occurs at $T_F \sim \frac{m_\chi}{25}$, rendering the particles NR and cold. If these particles constitute DM, their co-moving density remains constant after freeze-out. We can now estimate the relic density for $m_\chi \sim$ GeV:

$$\rho_\chi h^2 \approx 0.12 \rho_{\text{crit}} \left(\frac{80}{g_*}\right)^{1/2} \left(\frac{m_\chi}{25 T_F}\right) \left(\frac{2.2 \times 10^{-26} \text{cm}^3/\text{s}}{\langle \sigma v \rangle}\right). \tag{1.20}$$

This result implies that if the particle χ constitutes all the DM, the velocity-averaged annihilation cross-section at freeze-out is:

$$\langle \sigma v \rangle \approx 2.2 \times 10^{-26} \text{cm}^3/\text{s}. \tag{1.21}$$

Such value is close to the leading order scattering cross-section at the weak scale: in scenarios where DM consists of a yet unknown particle species with mass at the weak scale, a freeze-out annihilation cross-section at the weak scale naturally emerges. This phenomenon is often referred to as the "*WIMP miracle*". But how much is it a miracle? In scenarios that deviate from the typical WIMP miracle, the value of ρ_χ is determined primarily by the ratio $\frac{\langle \sigma v \rangle}{m_\chi^2}$. Hence, by varying the annihilation cross-section while maintaining a fixed product, a wider range of possible DM masses can be allowed. This approach suggests that even with different values of $\langle \sigma v \rangle$ thermal DM models can accommodate a broader mass range.
Originally developed to address issues like the electroweak hierarchy problem and the unification of interactions (GUT), Supersymmetry (SUSY) [25] also provides a framework for WIMP DM. SUSY predicts a new set of particles with spin differing by $\pm 1/2$ from SM particles, effectively doubling the number of elementary particles. A key feature of SUSY is R-parity, a quantum number that assigns $R = 1$ to SM particles and $R = -1$ to SUSY particles, ensuring that the lightest SUSY particle (LSP) is stable. The most studied WIMP candidate among the LSPs is the lightest neutralino, which is a mass eigenstate composed of the superpartners of the photon, W and Z bosons, and Higgs fields.
Additionally theories involving extra dimensions (UED), such as Kaluza-Klein (KK) models [26] [27], predict the existence of Kaluza-Klein states for each SM particles. These states arise from the compactification of extra dimensions and, in particular, the lightest KK particle (LKP) is predicted to be stable hence, could be a suitable WIMP DM candidate.

1.3.3 Other candidates

Here I will present a brief shortlist of other particle DM candidates but for a further investigation of this Non Baryonic Zoo (for instance little Higgs, primordial black holes, mirror matter, Q-balls, D-matter, brane DM, etc as depicted in the Fig. 1.9b), I recommend the the review by G. Bertone, [24]:

- **Neutrinos**: Neutrinos are abundant throughout the Universe, interact minimally with matter, and have relatively small masses. Observations of the CMB by Planck [1] indicate that the CMB photon number density is $n_\gamma^{CMB} \approx 410\,\mathrm{cm}^{-3}$. After decoupling from the primordial thermal bath, the number density of neutrinos is given by $n_\nu = \frac{3}{11} n_\gamma^{CMB}$. This results in a total relic density expressed as $\Omega_\nu h^2 = \sum_{i=1} \frac{m_i}{93\,\mathrm{eV}}$, where m_i denotes the mass of the i-th neutrino. Experiments have placed upper limits on neutrino masses: Tritium β-decay experiments find $m_\nu \leq 2.05\,\mathrm{eV}$ at 95% C.L. [28], while solar neutrino oscillation measurements by Super-Kamiokande suggest a mass limit around $0.05\,\mathrm{eV}$ [29]. Consequently, the upper bound on relic density is $\Omega_\nu h^2 \geq 0.07$, indicating that neutrinos cannot account for all DM. An alternative proposal involves introducing a fourth family of neutrinos, though such particles would need to be detected experimentally. Additionally, as relativistic, collisionless particles, neutrinos (HDM) have a significant free-streaming length of about 40 Mpc, which smooths out density fluctuations below this scale. This characteristic undermines scenarios of early galaxy formation by erasing fluctuations, leading to a top-down structure formation model that contradicts observations, as already mentioned.

- **Axions and ALPs**: CP violation in strong interactions, evidenced by the small electric dipole moment of the neutron (nEDM), leads to a significant constraint on the CP-violating parameter θ. To explain this small value, the axion, a light pseudo Nambu-Goldstone boson resulting from the spontaneous symmetry breaking of the Peccei-Quinn symmetry, $U(1)_{PQ}$, is proposed. Produced in the early Universe via the misalignment mechanism, axions have masses ranging from 10^{-5} to 10^{-2} eV and weakly interact with matter. They can oscillate into photons, making them detectable despite not yet being discovered. Additionally, spontaneous symmetry breaking generates axion-like particles (ALPs) in various theoretical frameworks. ALPs are also considered candidates for DM due to their stability, weak interactions, and potential production in the early Universe, aligning with properties of CDM.

- **FIMPs**: Feebly Interacting Massive Particles represent a distinct class of DM candidates with interactions much weaker than those of standard WIMPs. In these scenarios, the usual thermal freeze-out process is ineffective, as their annihilation cross-section is too low to achieve equilibrium. Instead, FIMPs are generated through a freeze-in mechanism, where an initially negligible population is slowly produced by decays or scatterings of heavier particles in the early Universe. This production is typically mediated by suppressed couplings to the PPSM,

resulting in very small interaction rates. Due to their extremely weak interactions and small couplings, detecting FIMPs is challenging.

- **Sterile neutrinos**: they are non-thermal relics that could arise if the PPSM neutrino sector is extended by adding light right-handed singlets and have masses in keV to MeV scale. These particles are called "sterile" because they do not interact via the electroweak force, except through mixing with active neutrinos. Since they are not in equilibrium with the PPSM, their interactions must be highly suppressed to avoid overclosing the Universe. Their decay into active neutrinos and photons makes them detectable through X-ray observations, although direct detection is unlikely due to their extremely weak interactions.

- **Light scalar DM**: Lee and Weinberg established that fermionic DM candidates with standard Fermi interactions would be limited to masses above a few GeV due to relic density constraints. However, lighter candidates are possible if other particle types are considered. For example, scalar particles with masses in the 1-100 MeV range have been proposed, particularly to explain the 511 keV γ-ray line observed by the INTEGRAL satellite, possibly originating from light DM annihilating into positrons. Additionally, decaying particles like axinos or sterile neutrinos have also been suggested as sources for this signal.

- **Super-heavy DM - Wimpzillas**: from the unitarity bound derives the concept of an upper limit for DM particles, leading to a typical mass constraint of around $340TeV$. Superheavy DM candidates like *"wimpzillas"*, with masses above $10^{10}GeV$, evade this bound since they were never in thermal equilibrium during freeze-out. Their relic density depends on production mechanisms like gravitational production post-inflation. These candidates are also linked to ultra-high-energy cosmic rays exceeding the GZK cutoff (occuring at $\sim 5 \times 10^{19}eV$ and above which protons interact at resonance with CMB photons with a center-of-mass of $1.232GeV$), suggesting top-down models where wimpzilla decay or annihilation might explain these events.

Chapter 2
DARK MATTER: EXPERIMENTAL APPROACHES

This chapter reviews current search strategies for DM and the key insights we can gain from indirect detection (ID) methods. But firstly we will explore all the different experimental techniques for DM searches: direct detection (DD), collider DM production, and of course indirect searches, highlighting their distinct approaches and strengths. Following that, it will be provided an overview of the leading telescopes and experiments actively contributing to the hunt for ID DM, focusing on IACTs: we will see in details the physics behind the production mechanism of γ-rays and how this class of detectors operates in order to measure them.

2.1 Dark Matter Detection

In the section 1.3, we discussed some of the allowed particle DM candidates, noting how some arise from ad-hoc theories while others do not; nevertheless, most of these candidates are still consistent with experimental evidence.
One of the leading DM candidates with strong observational prospects is the WIMP (from now on, we will also refer to them with the χ letter). Experimental attempts to identify χ can be classified into (as shown in the Fig. 2.1a): *direct detection* (DD) experiments, designed to observe SMχ scattering, aim to identify the recoil of WIMPs off the atoms or nuclei of terrestrial detectors; *collider experiments*' objective is to detect the DM particles produced in the collisions searching for missing transverse energy; finally, *indirect detection* (ID) experiments seek detection of DM via decay or annihilation into SM particles. Whilst all these experimental search strategies rely on detecting the interactions of DM particles with SM particles, their approaches are orthogonal and complementary.
Specifically:

- DD experiments (illustrated in graph **b)** of Fig. 2.1a), as previously said, aim to detect the interactions between DM particles and the detector material. These interactions manifest as either elastic or inelastic scattering events involving atomic nuclei or electrons. The key observable in these experiments is the nuclear recoil energy, typically in the *keV* range, which must be accurately measured. To achieve this, the detectors are designed with extreme sensitivity and are placed in environments where background contaminationarising from cosmic rays, environmental radioactivity, and internal noiseis minimized. This reduction in background noise is crucial for distinguishing genuine DM signals from spurious events, thereby enhancing the reliability and accuracy of the detection.

- Collider searches (graph **c)** of the Fig. 2.1a) aim to detect signals from DM particles produced when colliding SM particles in controlled laboratory conditions. In particular, the final goal would be to directly produce DM particles in high energy protonproton collisions through the

process inverse to DM annihilation. Of course, even when DM particles are produced, they typically do not leave signatures in the LHC detector: the only way to establish their existence is through missing momentum signatures. The DM particle carries away transverse momentum, leading to apparent violation of energy-momentum conservation among the visible SM particles in the event. At LHC it can also be probed the interaction between the SM and DM particles by searching for the mediator of the collision, as shown in the **d)** diagram of Fig. 2.1a.

- ID experiments (depicted in the **a)** diagram of Fig. 2.1a) search for fluxes of SM products by observing very high energy (VHE) messengers like γ rays, charged leptons and neutrinos, produced by the annihilation or decay of DM particles throughout the Cosmos. In particular, γ rays play a pronounced role as they propagate forward essentially unperturbed through the galaxy and therefore directly point to their sources. This technique benefits from the vast abundance of DM in the Universe which, as seen, constitute about five times the energy density of baryonic matter across cosmological scales.
  In this thesis, we will place particular emphasis on this detection method, which will be explored further in the following section.

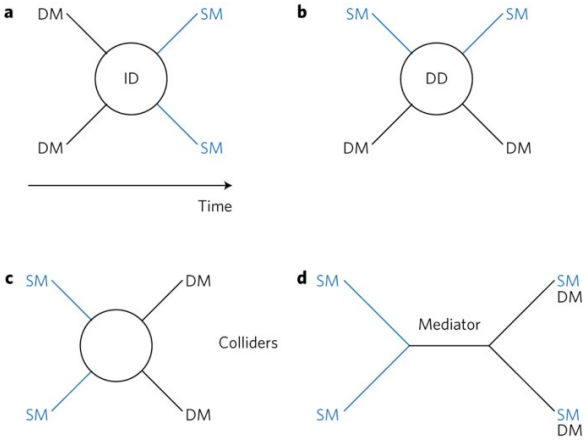

(a) Schematic illustration of DM interactions and their corresponding detection techniques. Credit: [30].

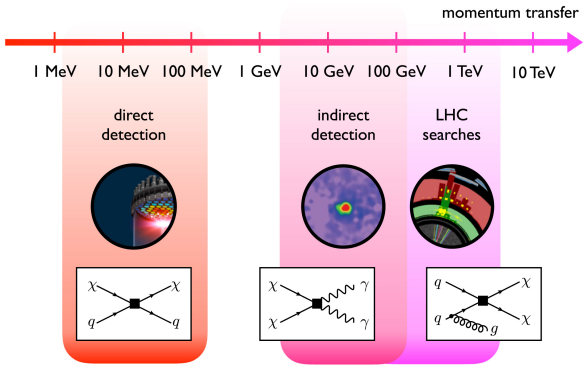

(b) Range of momenta probed in DD, ID and collider searches. Credit: [31].

Figure 2.1: Overview of DM detection methods.

In general ID, DD and collider searches probe different couplings in DM sector but it worth highlights the inter-balance between the different DM search strategies, in particular for high mass DM candidates, where signals stand out from background noise.
ID can provide information on DM mass (e.g., through a monochromatic signal from photon pairs or cutoff position in the spectrum), annihilation channels, and spatial distribution in the galaxy from spectral shape. However, ID faces significant challenges. Since DM is known to interact weakly with SM particles, the expected rate of particle production is low. Additionally, many detection channels suffer from significant background noise due to astrophysical sources, making it difficult to distinguish DM signals from ordinary particle production in the Universe. DD is particularly effective

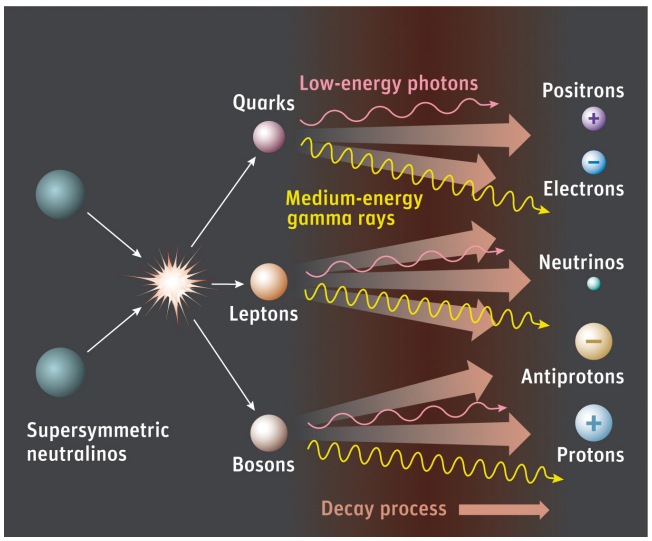

Figure 2.2: Sketch of possible neutralino (χ) annihilation channels and particle yield. Credit: [32].

when DM interactions involve lighter mediators, whereas LHC constraints are stronger in scenarios where DM is light but interacts via heavier new physics. In the first case, the DM production cross-section at a collider decreases rapidly with higher collision energy, but low-energy probes like DD do not suffer from this limitation. On the other hand, if DM is very light and relies on heavier mediators, LHC constraints become more powerful since low recoil energies make DD experiments less sensitive, while the LHC remains unaffected by such threshold effects. Hence, combined analyses especially in complex models like SUSY yield more comprehensive parameter space coverage.

2.2 Indirect DM Detection using γ-ray signatures

ID, as previously introduced, aim to detect products resulting from DM interactions, focusing on signals originating from the DM already present in the cosmos. Specifically, these searches target SM particles or radiation produced through DM decay or annihilation, seeking for anomalies in the fluxes of cosmic messenger particles: charged particles (electrons and positrons, antiprotons, antideuterium), photons (γ-rays, X-rays, synchrotron radiation) or neutrinos, as one can see in the Fig. 2.2. X-rays and γ-rays play an essential role in ID searches for DM, as high-energy photons are promising messengers. Several telescopes have been specifically designed to observe these signals, covering different energy ranges from keV to PeV. Fig. 2.3 provides an overview of various X-ray and γ-ray telescopes, highlighting the broad spectrum they cover and their operational timelines. These instruments, from past missions like Comptel and EGRET to upcoming ones such as ATHENA and e-Astrogam, are essential for detecting potential X-rays signals from DM. While, for instance, γ-rays can be traced back to regions with high DM density, such as the Galactic Center (GC), and observing excesses in these regions can offer insights into DM properties.
In the Table 2.1 is provided an overview of the ID experiments, with benefits and some of the next defiances.

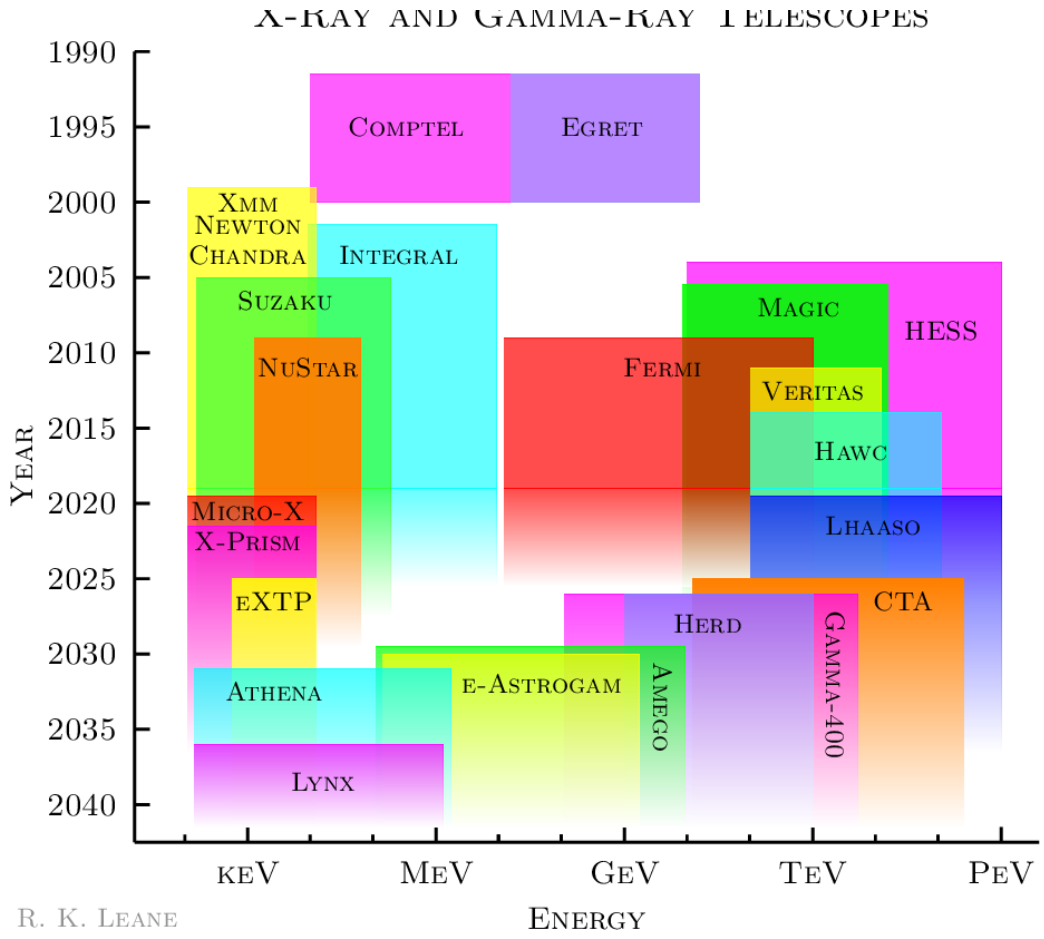

Figure 2.3: Timeline of X-ray and γ-ray telescopes, classified according to the energy range they observe. Credit: [33]

Particle	**Experiments**	**Advantages**	**Challenges**
Gamma-ray photons	Fermi LAT, H.E.S.S., MAGIC, VERITAS, HAWC, CTA, AGILE, GAMMA-400	point back to sources, spectral signatures	backgrounds, attenuation
Neutrinos	IceCube, DeepCore, KM3NET, ANTARES, BAIKAL-GVD, Hyper-Kamiokande, PINGU	point back to sources, spectral signatures	backgrounds, low statistics
Cosmic rays	PAMELA, AMS-02, ATIC, Fermi LAT, Auger, IACTs, CTA, GAPS	spectral signatures, low backgrounds for antimatter searches	diffusion, do not point back to sources

Table 2.1: Astroparticles for indirect searches experiments, advantages, and challenges. Experiment names in blue refer to planned experiments.

Specifically, γ-ray detection have some advantages over charged particles: primarily, since they do not get deflected by magnetic fields during their journey, they can trace back to their point of origin. This characteristic allows us to search for γ-ray signals not only from our local environment in the Galaxy but also from more distant regions like satellite galaxies or even galaxy clusters. In the event of a detected signal, this could serve as a distinctive method to probe the distribution of DM both within our Galaxy and across the Universe. The energy of γ-rays resulting from DM annihilation is

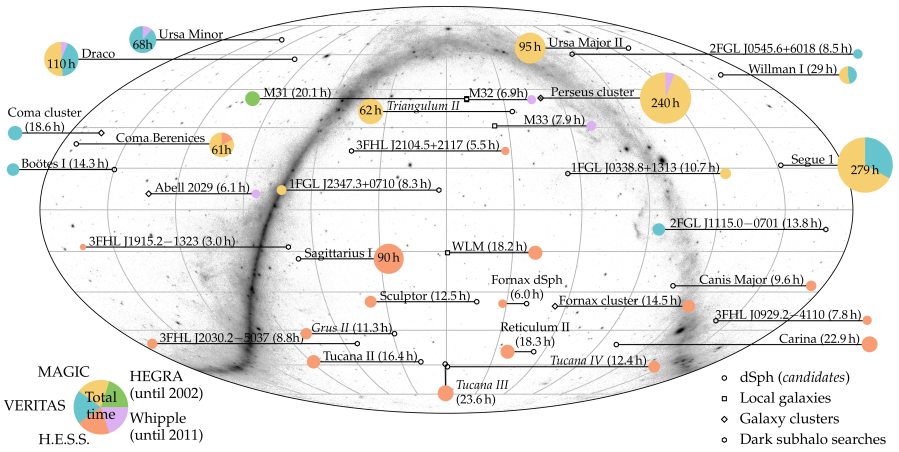

Figure 2.4: Visual summary of the probed targets outside the Galactic plane by different IACTs, along with the respective exposure times.Targets labeled in italics are candidate dSphs that are yet to be confirmed [34].

constrained by the mass of the annihilating particle, offering a specific spectral signature. In particular, given that the favored WIMP masses lie within the range of weak-scale interactions, γ-rays in the GeV to TeV range are especially relevant for studying DM particles. An additional benefit of γ-rays is that, within the local Universe, they do not experience attenuation, preserving the source's spectral information as observed from Earth.

γ rays can either be observed directly from space (with, for example, Fermi-LAT telescope) or via the showers of secondary particles they trigger in the atmosphere, (indirectly) with ground-based experiments (with, for instance, H.E.S.S or MAGIC detectors). Due to the size limitations and cost feasibility, the efficiency of satellite-based detectors is always restricted, while ground-based detectors imply rather small effective areas and an upper bound on the photon energy that can reliably be resolved but they allow for a large field of view and the observation of γ-rays at comparably small energies. We will discuss about the physics of ground-based γ-ray astronomy in the section 2.4.

DM searches using the current generation of IACTs began as early as the late 1990s, focusing on the Galactic center (GC) region and external galaxies. Although the GC is a promising source for a strong γ-ray signal from DM annihilation, it is also affected by significant background emissions up to TeV energies. These challenges have led to growing interest in exploring alternative targets. The Fig. 2.4 presents all published exposures of IACTs targeting potential DM sources in the extragalactic and galactic sky (in RA-DEC coordinates). The size of each pie chart indicates the total observation time dedicated to each target. In total, the map covers 1,329 hours of observations across 32 targets. Of these, MAGIC accounts for 716 hours, H.E.S.S for 292 hours, VERITAS for 271 hours, Whipple for 50 hours, and HEGRA for 20 hours. The background image shows, for context, the Fermi-LAT counts map accumulated over 705 weeks (approximately 13.5 years) above 1 GeV. It is important to note that observations of galaxies and galaxy clusters were conducted for multiple scientific objectives, while dwarf spheroidal galaxies (dSphs) (we will explore them better in the next chapter) were exclusively monitored for DM searches.

The expected DM-induced γ-ray flux for the above mentioned processes, from a direction Ω averaged over the opening angle $\Delta\Omega$ is:

$$\frac{d\Phi_\gamma}{dE_\gamma} = \begin{cases} \frac{\langle\sigma v\rangle}{4\pi}\frac{1}{2m_\chi^2}\sum_i BR_i\frac{dN_i^\gamma}{dE_\gamma}J_{\text{ann}}(\Omega) & \text{DM Annihilation} \\ \frac{1}{4\pi m_\chi}\sum_i \frac{\Gamma_i}{m_\chi}\frac{dN_i^\gamma}{dE_\gamma}J_{\text{dec}}(\Omega) & \text{DM Decay} \end{cases} \tag{2.1}$$

where $\langle\sigma v\rangle$ is the velocity-averaged cross-section, m_χ is the mass of the DM particle[1], and BR_i are the branching ratios into a generic channel f, while $\Gamma_i = \frac{1}{\tau_\chi}$[2] are the decay widths. N_i is the number of photons per annihilation/decay.

It is possible to note how the expression for the flux is composed of a factor that depends on the microscopic nature of the DM particles $\left(\frac{dN_i^\gamma}{dE_\gamma}\right)$, and, for the typically very small DM velocities, is usually sufficiently independent of v(r) that it can be pulled outside the integrals (note, however, that this is not true for strongly velocity-dependent cross-sections like in the case of Sommerfeld enhancement, resonances or p-wave annihilation). It contains the full spectral information. The left part of the (2.1) is the so-called astrophysical factor (or J-factor) $J(\Omega)$, which depends on the distribution of the halo in space. Its expressions, depending on the process considered, are:

$$J_{\text{ann}}(\Omega) = \int_{\Delta\Omega}\int_{\text{l.o.s.}} \rho_\chi^2(l,\Omega)dld\Omega \tag{2.2}$$

$$J_{\text{dec}}(\Omega) = \int_{\Delta\Omega}\int_{\text{l.o.s.}} \rho_\chi(l,\Omega)dld\Omega \tag{2.3}$$

where the acronym l.o.s. stands for *line-of-sight*, meaning that we are integrating along the line connecting the source to the observer, revealing the angular dependence of the signal. The J-factor is a crucial indicator of how promising an astrophysical target is for DM annihilation searches: the larger the J-factor, the more attractive the target becomes. For dwarf galaxies, the J_{ann} are typically around $J_{\text{ann}} \sim 10^{19-20}\,\text{GeV}^2/\text{cm}^5$. For our nearest neighbor, the Andromeda galaxy, it is roughly $J_{\text{ann}} \sim 10^{20}\,\text{GeV}^2/\text{cm}^5$. In comparison, for our own Galactic Center, the J_{ann} can reach $\sim 10^{22-25}\,\text{GeV}^2/\text{cm}^5$ (or $10^{22-24}\,\text{GeV}^2/\text{cm}^5$ within 1ř) [17].

Each DM model has its own characteristic γ-ray spectrum, as described by equation (2.1). The signal strength from an annihilation (or decay) process is primarily governed by the branching ratio BR_i (or decay width Γ_i) of the specific channel. Determining all BR_i (or Γ_i) would involve a detailed understanding of the DM particle interactions. Consequently, a common approach is to simplify the analysis by adopting a benchmark scenario: one sets $BR_i = 1$ for the desired channel i, while assuming it is zero ($\Gamma_j = 0$) for all other channels $j \neq i$.

[1] Note that for the annihilation process we are assuming the amount of χ to be the same as the one of its own antiparticle $\overline{\chi}$ (i.e. DM is a Majorana particle), otherwise we need to add a $1/2$ factor.

[2] Of course, τ_χ is the DM particle lifetime.

To achieve a detection, a sufficient number of photon counts is required, ideally a substantial amount:

$$N_\gamma \sim \int_{\mathrm{E}_\gamma \text{ range}} dE_\gamma \, \phi_\gamma \cdot A_{\mathrm{eff}}(E_\gamma) \cdot T_{\mathrm{obs}} \tag{2.4}$$

where A_{eff} is the *effective area* of the telescope, and T_{obs} the time of observation of the source. The table below 2.2 provides a general guideline for the relevant energy ranges, effective areas, and observation times for current and upcoming γ-ray detectors [35]:

	Fermi-LAT	**H.E.S.S.**	**CTA**
E_γ range	0.1 to 300 GeV	0.1 to 10 TeV	10 GeV to 10 TeV
A_{eff}	$\sim 1\,\mathrm{m}^2$	$\sim 10^5\,\mathrm{m}^2$	$\sim 10^6\,\mathrm{m}^2$
t_{obs}	$\sim 10^8\,\mathrm{s}$	$\sim 10^6\,\mathrm{s}$	$\sim 10^6\,\mathrm{s}$

Table 2.2: Approximate energy ranges, effective areas, and observation times for different gamma-ray observatories.

2.3 Spectral annihilation DM signatures

Let's focus on the DM annihilation spectrum. The DM particles that constitute the DM halo of the Milky Way (MW), as already explained, are expected to annihilate into pairs or into trios of primary SM particles, which is usually referred to as *prompt emission* (such as $b\bar{b}, \mu^+\mu^-$, $\tau^+\tau^-$, W^+W^- and so on), which after decaying and through the processes of showering and hadronizing, give origin to fluxes of energetic cosmic rays: relativistic e^+e^-, protons and antiprotons and also γ-rays and high energy neutrinos (ν). Additional lower energy photons can result from the interaction of the relativistic electrons with magnetic fields (synchrotron radiation), with interstellar material (bremsstrahlung), and with the CMB and stellar radiation fields (inverse Compton scattering). In the following we will focus on the γ-rays, since they are likely the strongest signal from Galactic DM substructure.

Depending on which one has been the primary SM particle, the resulting spectra differ substantially in the details. In particular, the total spectrum of χ particles emitted per annihilation (dN_i^γ/dE) can be written as the sum of the spectra produced for all possible final states f:

$$\frac{dN_i^\gamma}{dE} = \sum_i BR_i \frac{dN_i^\gamma}{dE_\gamma}. \tag{2.5}$$

where BR_i is the branching ratio to final state f and $\frac{dN_i^\gamma}{dE_\gamma}$ is the spectrum of i particles produced for final state f. This input is given by particle physics, meaning that the branching ratios to different final states are model-dependent. The most probable annihilation channels for particle DM (with mass $M_\chi \sim GeV - TeV$ range) are heavy particles such as $b\bar{b}$, W^+W^- and $\tau^+\tau^-$. The emphasis on these channels arises from a combination of mass considerations, coupling strengths, phase space availability, and theoretical basis from particle physics models. In the case of the $b\bar{b}$ mode, being relatively heavy

(around 4.2GeV), we can expect it to be produced in annihilation events where sufficient energy is available; a very same consideration could be done for the mass of τ lepton, being larger than the other leptons' mass. The nature of weak interactions plays a crucial role. DM particles could prefer to annihilate into W boson pairs, because they mediate these interactions.
As precisely shown in the Fig. 2.5 there are essentially three different ways to produce γ-rays: from primary photons, from internal bremsstrahlung and from line signals. Let's see this in details:

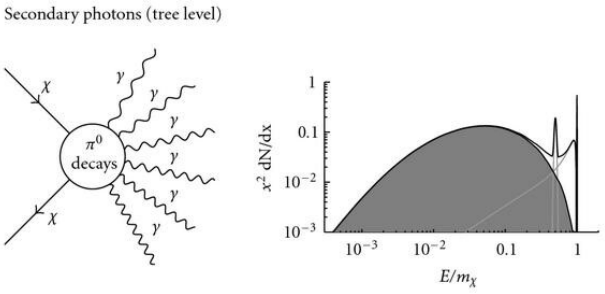

(a) Secondary photons (tree level)

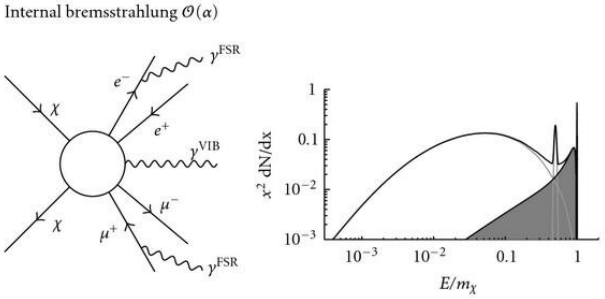

(b) Internal Bremsstrahlung $\mathcal{O}(\alpha)$

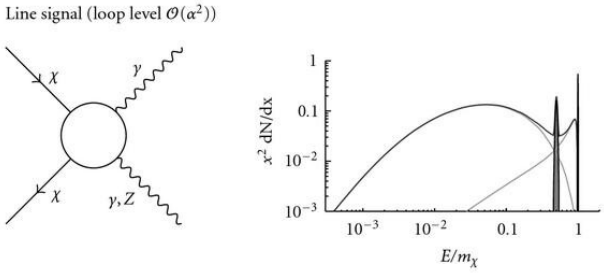

(c) Line signal (loop level $\mathcal{O}(\alpha^2)$)

Figure 2.5: Comparison of different photon production mechanisms from dark matter interactions: (a) Secondary photons from π^0 decays, (b) Internal Bremsstrahlung, and (c) Line signal from loop-level processes. Image taken from: [36].

a) since the DM particle is neutral, there is no direct coupling to photons. Nevertheless, copious amounts of secondary γ-ray photons can be produced through the decay of neutral pions, $\pi^0 \rightarrow \gamma\gamma$, arising in the hadronization of the primary annihilation products. Since the DM particles are nonrelativistic, their annihilation results in a pair of mono-energetic particles with energy equal to m_χ, which fragment and decay into π-meson dominated jets. In this way a single DM

annihilation event can produce several tens of γ-ray photons and the result is a broad spectrum with a cut off around m_χ.

b) Internal Bremsstrahlung (internal as it does not require an external electromagnetic field) is present every time DM annihilate into charged final states at $\mathcal{O}(\alpha)$, at high energies ($E \leq m_\chi$). Its spectrum has its peak at $E \sim m_\chi$ and shows a sharp cut off. Notice that the photons can be either produced in the form of final state radiation (FSR) from external legs or as virtual internal bremsstrahlung (VIB) from the exchange of virtual charged particles. FSR is largely characterized by collinear photons, making it especially significant for light final state particles where $m_f \ll m_v$. This process yields a model-independent spectrum with a distinct cutoff at $E_c = m_v$. An illustrative case of such a spectrum, influenced by FSR, is found in KaluzaKlein DM. Conversely, VIB becomes dominant when the tree-level annihilation rate is reduced, such as in the annihilation of Majorana particles into light fermions, or when the final state consists of bosons with the t-channel particle being nearly degenerate with m_v. VIB typically produces noticeable bump-like features at $E_c \approx m_v$, which may resemble a slightly distorted line when the energy resolution $\Delta E/E$ is around 0.1. The exact shape of VIB spectra is, however, highly model-dependent, which could enable effective discrimination between different DM models given sufficient statistics.

c) The line signal derives from mono-energetic photons produced in final states such as $\gamma\gamma$, γH or γZ, but since DM is neutral, there is no direct coupling to photons hence, γ-rays are a result of suppressed loop-level diagrams $\mathcal{O}(\alpha^2)$ and they are expected to produce far fewer events, for which reason they can not be easily detected; specifically, the $\gamma\gamma$ final state results in a monochromatic narrow line at the DM mass. While, for a γZ final state, the energy line is still monochromatic, but is shifted to lower energies:

$$2m_\chi = E_\gamma + \sqrt{E_\gamma^2 + m_X^2} \longrightarrow E_\gamma \approx m_\chi \left(1 - \frac{m_X^2}{4m_\chi^2}\right)$$

In the Figure 2.6 we can notice all the various γ-ray spectra expected from DM annihilation: the blue lines depict the photon energy spectrum for a $\gamma\gamma$ final state with energy resolutions of $\Delta E/E = 0.15$ (solid) and $\Delta E/E = 0.02$ (dotted). Observing such a γ-ray 'line' would provide striking evidence for DM annihilation. However, as seen, the production of a photon pair is often loop-suppressed and thus relatively minor in many models. The red lines demonstrate the spectrum modification due to photons emitted from VIB. This effect broadens the line towards lower energies, although the spectrum still features a cutoff at the DM mass. The green lines illustrate the box spectrum, which occurs when DM annihilates into a new state ϕ (e.g., $\chi\chi \to \phi\phi$) that subsequently decays into a photon pair ($\phi \to \gamma\gamma$). Additionally, if DM annihilates into leptons, gauge bosons, or quarks, secondary photons may be produced either through final-state radiation or from the decay products. The relative importance of these three γ-ray production channels and the resulting spectrum $\frac{dN_i^\gamma}{dE_\gamma}$ de-

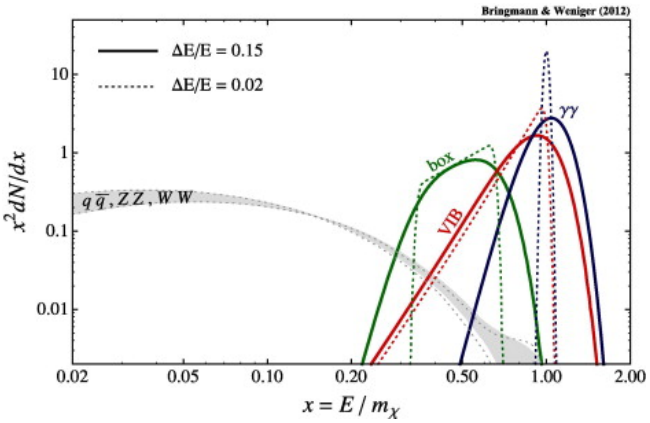

Figure 2.6: Photon energy spectrum for the $\gamma\gamma$ final state, comparing scenarios with (red) and without (blue) virtual internal bremsstrahlung. The green box spectrum represents the case where DM annihilates into a new state that subsequently decays into photons, as detailed in the text. The distinguishes between two different energy resolutions: $\Delta E/E = 0.02$ (dotted lines) and $\Delta E/E = 0.15$ (solid lines). The gray band illustrates the spectrum for photons resulting from DM annihilation into gauge bosons and quarks. Adapted from [37].

pend on the details of the DM particle model under consideration. For any given model, realistic γ-ray spectra can be calculated using sophisticated and publicly available computer programs, such as the `Pythia` in the version 8.135 Monte-Carlo event generator [38]. Specifically, the tool PPPC4DMID (Poor Particle Physics Cookbook for Dark Matter Indirect Detection) [39][3] provides precomputed tables for γ-ray spectra from DM annihilation or decay for a wide range of final states and DM masses. This package is particularly useful for quick and accurate computations of $\frac{dN_i^\gamma}{dE_\gamma}$, supplying ingredients and recipes for computing signals of TeV-scale Dark Matter annihilations and decays. An example of the prompt emission spectra of photons, neutrinos, electrons/positrons, and protons/antiprotons associated with several final states are shown in 2.7, calculated using the PPPC4DMID package which includes electroweak corrections, important for multi-TeV candidates.

A more recent and enhanced version of this approach is offered by the `CosmiXs` framework[4] [41]. CosmiXs builds upon the capabilities of PPPC4DMID by allowing on-the-fly computation of $\frac{dN_i}{dE}$ spectra for a wide variety of DM models and decay channels. It provides a more flexible and user-friendly interface, enabling researchers to explore custom DM scenarios beyond the precomputed tables offered by PPPC4DMID. CosmiXs also incorporates updated models and cross sections, ensuring more accurate predictions for indirect detection signals, making it a powerful tool for both phenomenological studies and experimental comparisons. We will come back at the details in the next chapter.

2.4 Ground-based Cherenkov Telescopes

Very high energy (VHE) γ-rays ($E \geq 100GeV$) are detected by ground-based telescopes through the observation of secondary cascade particles produced when γ-rays interact with the atmosphere. The

[3] Avaiable at this http://www.marcocirelli.net/PPPC4DMID.html
[4] Avaiable at this https://github.com/ajueid/CosmiXs.git

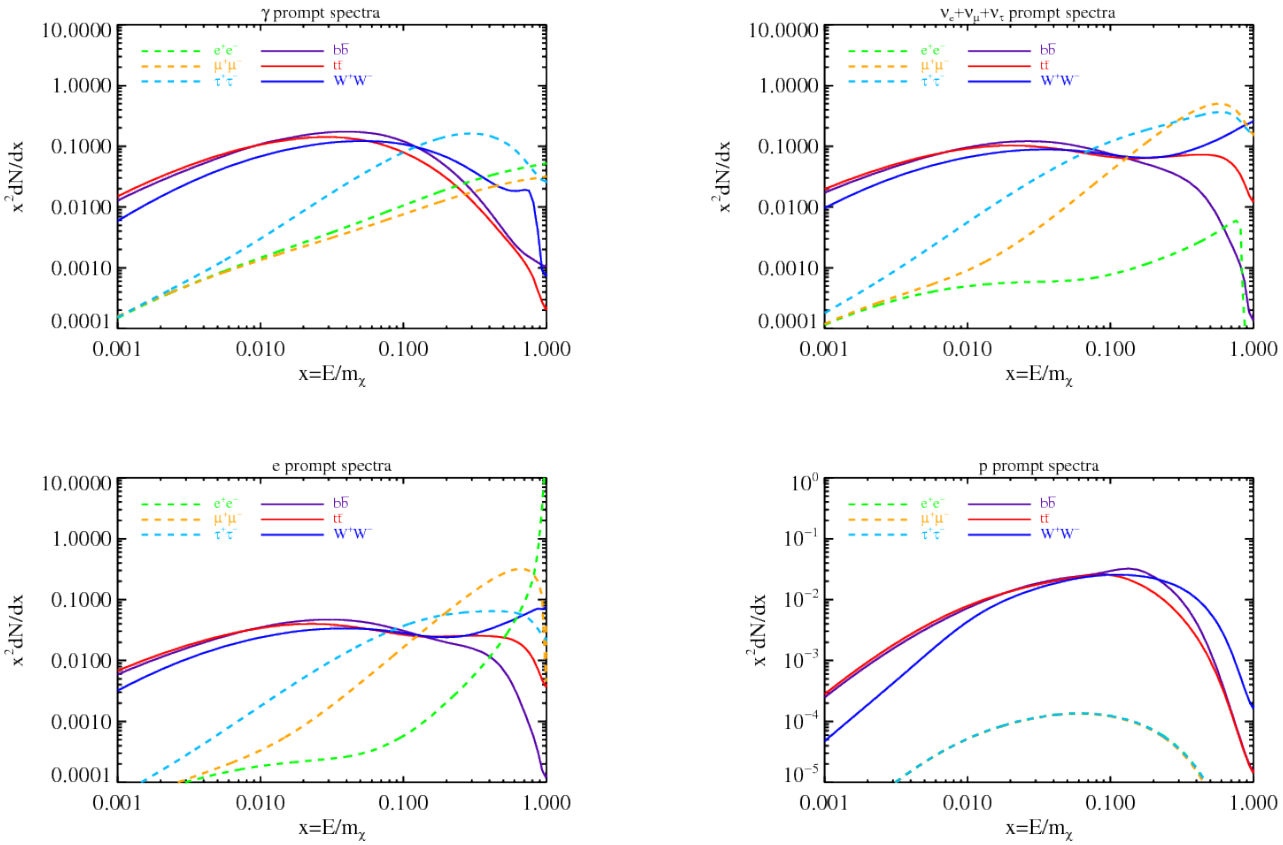

Figure 2.7: Differential energy spectra per annihilation for a DM particle with mass $m_\chi = 500$ GeV, shown as a function of $x = E/m_\chi$. The spectra are displayed for the following final states: photons (top left), sum of all neutrino flavors (top right), electrons (bottom left), and protons (bottom right). These spectra are valid for the decay of a DM particle with mass $2m_\chi$ [40].

key technique behind this approach involves studying these cascade of particles, known as atmospheric showers, which can be either electromagnetic or hadronic in nature.[5] The secondary particles in the cascade emit low-energy photons, ranging from visible to ultraviolet light, through Cherenkov radiation.

Ground-based detectors such as IACTs (Imaging Atmospheric Cherenkov Telescopes) are employed for this purpose. Powerful arrays of IACTs are located in both hemispheres: MAGIC (Major Atmospheric Gamma Imaging Cherenkov Telescopes) and VERITAS (Very Energetic Radiation Imaging Telescope Array System) in the Northern Hemisphere, and HESS (High Energy Stereoscopic System) in the Southern Hemisphere. However, when it comes to ground-level particle detectors, only the Northern Hemisphere is equipped with HAWC (High Altitude Water Cherenkov Observatory) and LHAASO (Large High Altitude Air Shower Observatory).

IACTs have a limited field of view (FOV $\sim 4^\circ - 10^\circ$ diameter) and a duty cycle of $\sim 10 - 15\%$ due to the requirement of dark and clear skies. They achieve an angular resolution of $\sim 0.1^\circ$, 15%, and have a background rejection power of $10^{-3} - 10^{-2}$ with a γ-ray efficiency exceeding 70%. As previously mentioned, the imaging technique involves detecting the Cherenkov light emitted by electromagnetic cascades from the ground, managing to determine both the longitudinal and lateral development of

[5] I remind to the Appendix B for explanation of the physics of these processes.

the electromagnetic showers, as well as the arrival direction and energy of the primary γ-rays. These detectors typically use a parabolic or spherical mirror to focus the Cherenkov photons onto a densely packed array of photomultiplier tubes (PMTs) positioned in the focal plane. The detection technique of IACTs is shown in Fig.2.8.

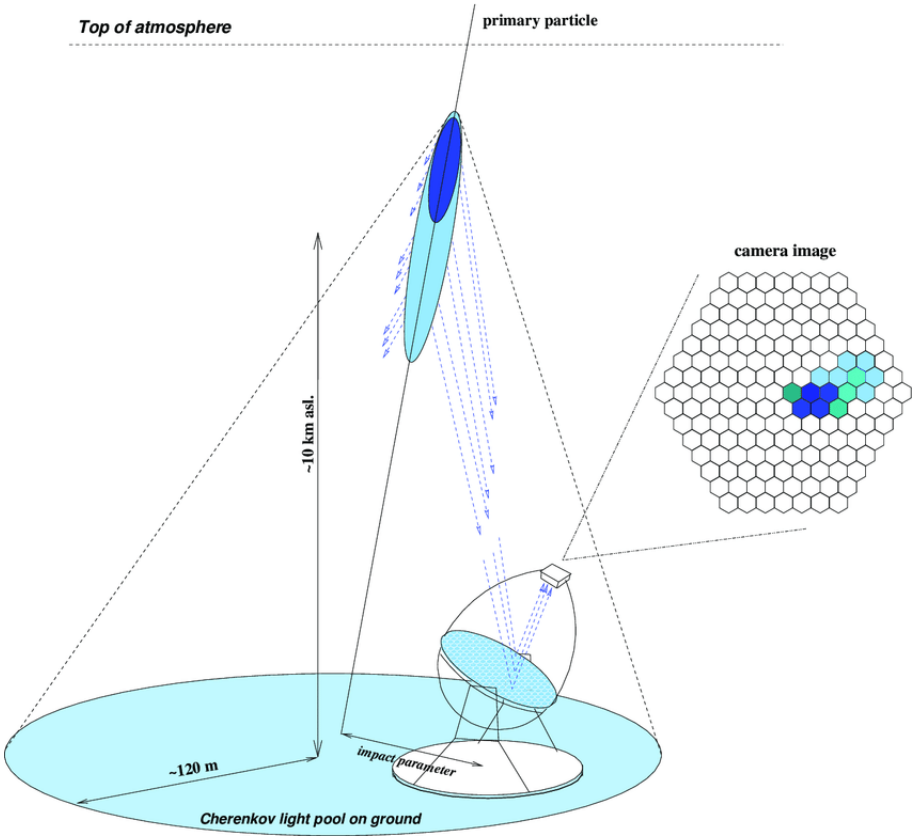

Figure 2.8: Working technique of IACTs.

2.4.1 Cherenkov radiation

Cherenkov radiation was first observed by Cherenkov in 1934 and later theoretically explained by Frank and Tamm in 1937. It occurs when a charged particle travels through a transparent dielectric medium at a velocity greater than $v = \frac{c}{n}$, where c is the speed of light in a vacuum and n is the refractive index of the medium. This phenomenon results in the emission of electromagnetic radiation, including visible light in the UV. The emitted Cherenkov light is observed at a characteristic angle relative to the direction of the particle's motion. This angle, known as the Cherenkov angle θ_c, is given by:

$$\cos\theta_c = \frac{1}{n\beta}, \tag{2.6}$$

where $\beta = \frac{v}{c}$ is the normalized velocity of the particle. The Cherenkov radiation is emitted along the surface of a cone, with the angle θ_c defining the cone's opening. Within this cone, the phase of the radiation emitted by the excited microscopic dipoles in the medium is coherent, as illustrated in Fig. 2.9.

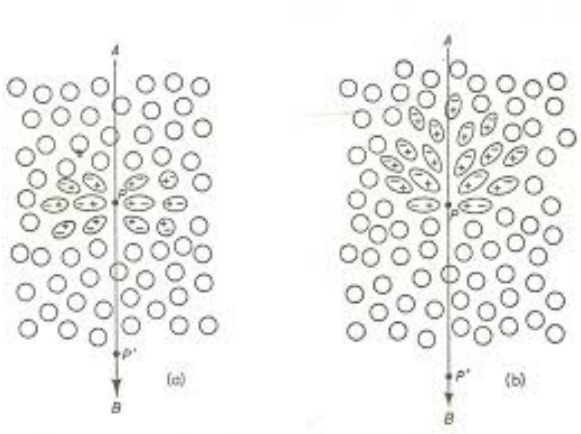

(a) The local polarization produced in a medium during the passage of a particle; on the left the case where the velocity of the particle is $v \leq \frac{c}{n}$, on the right where the velocity of the particle is $v \geq \frac{c}{n}$.

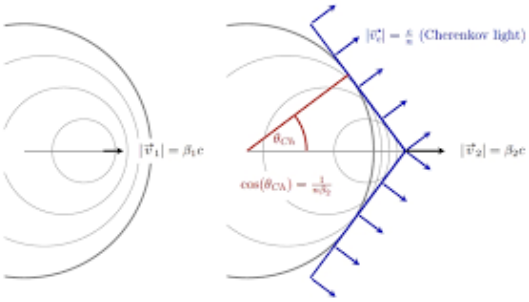

(b) When a charged particle moves through a medium with refractive index n at a velocity $v_1 < \frac{c}{n}$, destructive interference cancels the emitted dipole radiation. However, if the velocity is $v_2 > \frac{c}{n}$, constructive interference occurs, producing a cone of radiation. The wave-fronts propagate perpendicular to the cone's surface due to in-phase perturbations in the medium's polarization along the particles path.

Figure 2.9: Illustration of Cherenkov radiation phenomena.

The number of Cherenkov photons emitted by a charged particle with atomic number Z per unit wavelength λ and per unit path length is given by:

$$\frac{dN}{dx\,d\lambda} = \frac{2\pi\alpha Z^2}{\lambda^2}\left(1 - \frac{1}{\beta^2 n^2(\lambda)}\right), \tag{2.7}$$

where α is the fine structure constant.

Due to the inverse square dependence on the wavelength of Cherenkov photons, the emission is maximized at shorter wavelengths (ultraviolet range) and decreases as the wavelength increases. However, the spectrum observed is modified by atmospheric absorption mechanisms (which are stronger for shorter wavelengths), typically exhibiting a peak in the ultraviolet range.

2.4.2 Detection Principles of IACTs

As previously explained, IACTs operate by collecting the Cherenkov light emitted from extensive air showers induced by γ-rays interacting with the Earth's atmosphere. This light is then focused by large mirrors onto an array of photo-multiplier tubes (PMTs), which detect the photons and provide data on the characteristics of the primary γ-rays, such as their energy and direction.

Now, the Cherenkov light is emitted by the secondary particles produced in the cascade, through the emission of low energy (visible to ultraviolet) photons in a ring of cone of light where the shower axis is the direction of the charged particle and the opening angle is the Cherenkov angle. Since this angle depends inversely on the refraction index (see the Eq. (2.6)) which decreases as the altitude decreases, the lower the altitude, the broader the Cherenkov angle becomes, as one can see in the fig. 2.10. Apparently a Cherenkov telescope might resemble a classical optical telescope, but the difference lays in the core of this type of emission: both telescopes are focused to where the photons are produced, but while optical telescopes are focused to outside atmosphere, i.e. to infinity, Cherenkov

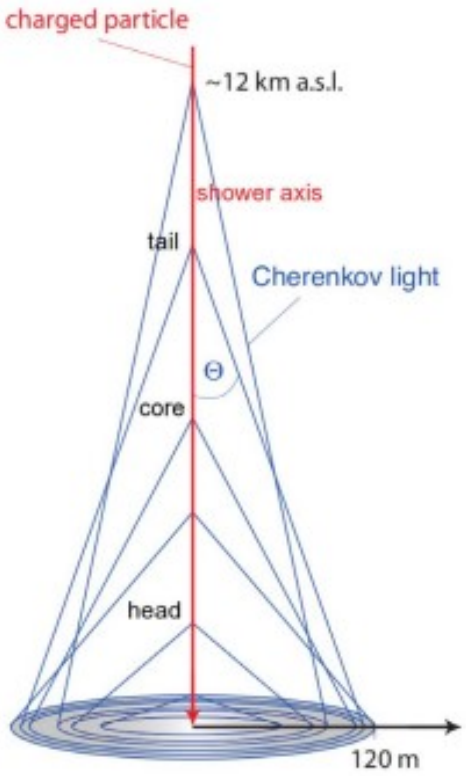

Figure 2.10: The Cherenkov light pool is a composite of Cherenkov emissions occurring at various altitudes. Due to the altitude-dependent refractive index, the Cherenkov angle decreases as the altitude decreases. For example, at an altitude of 10 km above sea level (a.s.l.), the Cherenkov angle is approximately 0.66 rad, while at 8 km a.s.l., it is around 0.74 rad, and at sea level, it increases to about 1.4 rad. Cherenkov light is primarily emitted at around 10 km a.s.l. However, depending on the emission altitude, the emission profile is characterized by three distinct regions: the tail, the core, and the head of the light pool.

telescopes are focused to where the secondary photons are produced i.e. to $\sim 10km$ a.s.l.
Differently from the first-generation atmospheric Cherenkov telescopes (ACT), IACTs are more sophisticated, where a large reflector focuses Cherenkov light onto an array of PMTs arranged in the focal plane, forming a camera that captures images of Cherenkov light from each air shower. When the camera is triggered by a trigger system, the light levels in each pixel are recorded and subsequently analyzed offline. The key advancement with IACTs is the imaging capability: distinguishing between hadronic and γ-ray events can be achieved by analyzing the images of Cherenkov photons focused onto the camera. The difficulties in the early γ-ray observations may be traced back to the massive background of nuclear CR events. In addition, the large spatial extension of air showers in the direction of the primary photon trajectory leads to a very extended image in the camera plane (see fig. 2.11), making the size of the FoV of the camera a critically important parameter of the system. To illustrate, the primary particle interacts within the atmosphere initiating atmospheric showers. The particles produced in the shower which exceed the speed of light emit Cherenkov radiation. Then, if the Cherenkov telescope is placed into the light pool, it collects the photons and reflect them into a pixelized camera, forming an elliptical shape. Its center corresponds to the core of the shower while its extremities are the head and the tail of the shower. Its major axis is the projection of the shower axes into the plane of the camera. In the camera, the signal is converted from EM to electronic form, creating an image that can be characterized using specific parameters, known as Hillas parameters 2.12:

- *size*: the sum of the charges of the surviving pixels in the image. This parameter is related to the energy of the primary particle.

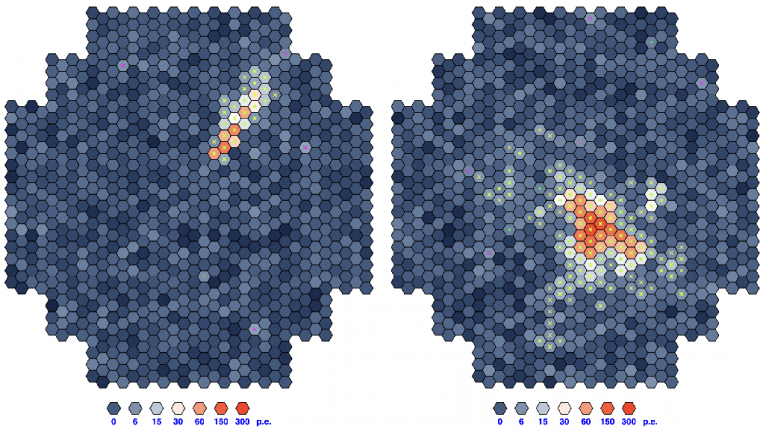

1.0 TeV gamma shower 2.6 TeV proton shower

Figure 2.11: Difference between the images of gamma-induced (left) and hadron-induced (right) showers in the camera of a IACT. Credit: [42].

- *center of gravity*: the weighted average of the X and Y coordinates of the image in the camera. It indicates the central position of the image.
- *length*: the length of the semi-major axis of the ellipse fitted to the image. This parameter is related to the longitudinal development of the shower.
- *width*: the length of the semi-minor axis of the ellipse fitted to the image. It is associated with the lateral development of the shower.
- *dispersion (or dist)*: the angular distance between the expected position of the source and the center of gravity of the image.
- *alpha*: the angle between the major axis of the ellipse and the line connecting the expected position of the source in the camera to the center of gravity of the image.

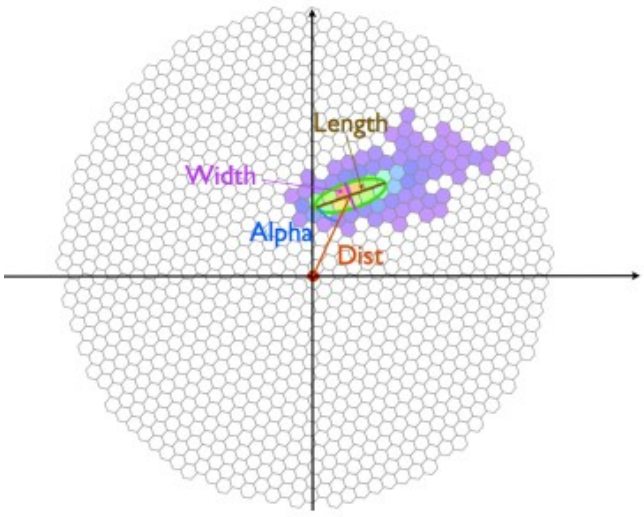

Figure 2.12: Illustration of Hillas parameters.

Chapter 3
METHODOLOGY

As outlined in the executive summary, this thesis aims to contribute to prof. M. Doro's `gDMbounds` project. My work is divided into two main steps:

- starting with the new *CosmiXs* model [41] for the source spectra of annihilation/decaying DM, I focused on the γ-ray spectrum, calculated the predicted photon count N_γ, and then compared these results with predictions from the earlier model by M. Cirelli et al. [39];
- I revisited the *PPPC4DMID* model, leveraging its predictions for dN/dE, to extend the features of the `gDMbounds` portal. Specifically, our primary aim is to predict one specific annihilation channel starting from one observed (and hence published) channel. The starting point was to find the projected $\tau^+\tau^-$ DM channel curve using the observed $b\bar{b}$ DM channel for several experiments. Then, I enlarged the study source by source, exploring all the various annihilation channels as well as other experiments.

This chapter will investigate the technical methodologies and tools employed at each step: it begins with an explanation of the `gDMbounds` portal structure and continues with the description of *gammapy*: the specific python tool for astronomers and astrophysicists I used for this thesis. Then I will provide a brief technical outline of the difference between *PPPC4DMID* and *CosmiXs*, and I will conclude with the core contribution of my work, detailing the general assumptions behind the principal idea and highlighting how the methodology developed in this research serves as a stepping stone for broader applications.

3.1 Overview of the structure of `gDMbounds`

The portal `gDMbounds` was designed as a centralized tool to compile DM annihilation and decay limits from various studies and to process them for quickly generating custom predictions for different instruments and DM models. The repository gDMbounds available on GitHub, was specifically created to aggregate results from analyses of data collected by space-based and ground-based telescopes, serving as a streamlined resource to access and compare these outcomes for a variety of research purposes.
In developing `gDMbounds`, attention was directed towards the review and the examination of articles providing detailed information on the upper and lower bounds of cross-sections for DM annihilation ("upper limits") and decay ("lower limits") processes. For a full list of the studies analyzed and included in the portal it could be visited this link. Operationally graphs depicting $< \sigma v >$ vs m_χ for annihilation processes and τ_χ vs m_χ for decay processes were extracted from these articles. The data

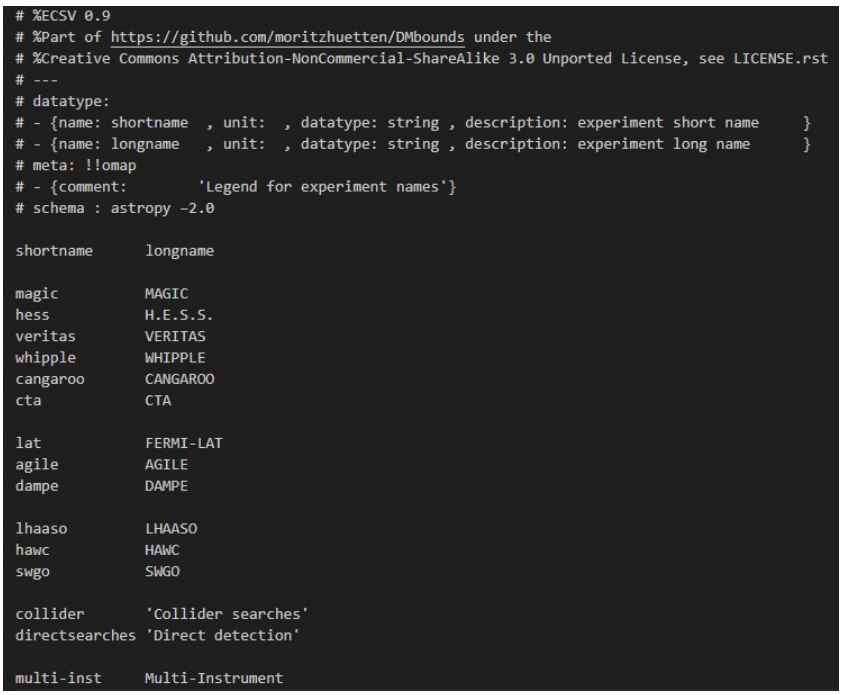

```
# %ECSV 0.9
# %Part of https://github.com/moritzhuetten/DMbounds under the
# %Creative Commons Attribution-NonCommercial-ShareAlike 3.0 Unported License, see LICENSE.rst
# ---
# datatype:
# - {name: shortname  , unit:  , datatype: string , description: experiment short name     }
# - {name: longname   , unit:  , datatype: string , description: experiment long name      }
# meta: !!omap
# - {comment:        'Legend for experiment names'}
# schema : astropy -2.0

shortname      longname

magic          MAGIC
hess           H.E.S.S.
veritas        VERITAS
whipple        WHIPPLE
cangaroo       CANGAROO
cta            CTA

lat            FERMI-LAT
agile          AGILE
dampe          DAMPE

lhaaso         LHAASO
hawc           HAWC
swgo           SWGO

collider       'Collider searches'
directsearches 'Direct detection'

multi-inst     Multi-Instrument
```

Figure 3.1: Legend of the analyzed instruments of `gDMbounds`.

points from these plots were collected into .ecsv extension files using the open-source WebPlotDigitizer tool. These files are primarily used in scientific fields and data analysis, especially for complex tabular data from scientific experiments or simulations. These .ecsv files are stored in the *bounds* sub-folder of *dmbounds* on the portal. They are organized within subfolders named after specific instruments of detection (telescopes and/or direct detection machines), listed in the Fig. 3.1.
On this page you can explore the list of the observed and stored target in the project, which will now be explained in detail. Generally speaking, as outlined in [43], current WIMPs search by IACTs include "classical target" as the central galactic region of Milky Way i.e. the **Galactic Center** (GC), the MW**Dwarf Spheroidal Galaxies** (dSphs) and **Galaxies Cluster**. However, they also include less conventional target like **Dark Satellites**. These are the same categories of targets included in `gDMbounds`:

- **Galactic Center** (GC): is one of the most important target for astronomers and astrophycisian firsly because it is located close to us (26000 ly from Earth) in the Sagittarius constellation; this proximity is also related to the DM halo of MW (having mass $M_{halo} \sim 10^{12} M_{\odot}$: the observed signal is significant for the ID of DM. It comes most likely from the innermost region of this target although, as well explained by the article [43] by M. Doro et. al, it could not be concluded the accurate density profile parametrization. The GC is more easily observable from the southern hemisphere because it is higher in the sky, resulting in less atmospheric absorption and better visibility. This optimal position allows telescopes to detect lower-energy γ-rays, as the reduced air mass leads to a lower energy threshold.

- **Dwarf Spheroidal Galaxies** (dSphs) are small (masses of the order of $10^7 - 10^9 M_{\odot}$), DM-dominated systems gravitationally bound to larger galaxies, including the MW. They are be-

lieved to play a crucial role in star formation, as they emerge from the gravitational collapse of gas and dust clouds. As these clouds condense, they can lead to the birth of new stars. Located within the MW's virial radius, they exhibit high mass-to-light ratios, indicating minimal visible matter. Their low stellar activity and minimal high-energy photon emission make them ideal candidates for indirect DM searches. However there are some mismatches between observations and expectations from N-body cosmological simulations, including the "missing satellite problem" and the "too big to fail" issue. dSphs are categorized into classical and ultra-faint groups, with nearly 50 ultra-faint candidates discovered recently via photometric surveys. Currently, the cross-section limits derived from dSph observations using IACTs are the most stringent, of the order of $10^{-24} cm^3/s$.

- **Galaxies Clusters**: are extragalactic structures (literally galaxies clump together) located at "cosmological distances". These distances are so large that they require considering the expansion of the Universe for accurate measurements. Essentially, we are observing these clusters as they were in the distant past, with their light having traveled billions of years to reach us. That is the reason for which any radiative signal would be diluted or attenuated by background light. Also, these objects have really large masses of the order of $10^{14} - 10^{15} M_{\odot}$, where approximately the 80% of their total virial mass is DM and therefore they represent the largest gravitationally bound systems of the Universe. Galaxies clusters are highly effective targets for decaying DM compared to dSphs, due to their enormous total mass concentrated within a small angular area. Identifying DM signatures in these clusters requires separating them from conventional astrophysical contributions but fortunately, the spatial distribution of γ-ray signals can help in distinguishing these sources, as highlighted by the article of [44]. The most detailed study of a galaxy cluster to date was conducted using the MAGIC telescopes on the Perseus cluster in the article [45], running observations for over 400 hours across several years, providing stringent constraints on DM decay lifetime.

- **Dark satellites**: in the standard cosmological model, small dense DM structures formed early in the Universe and later merged into larger halos. Among these, "dark clumps" or "dark subhalos" are regions within the interstellar medium (ISM) characterized by high DM density but very low or no intrinsic luminosity. Despite lacking detectable radiation, they exert gravitational influences on nearby objects. These subhalos could represent excellent targets for indirect DM detection due to their potentially strong γ-ray signals from DM annihilation or decay, especially given their lack of astrophysical background emissions. However, locating them is challenging, as they are not yet identified and are not well-suited for narrow-field telescopes, making wide-field instruments like Fermi-LAT (which continuously monitors the entire sky) more effective, by identifying signals in the GeV range. Nevertheless uncertainties remain due to incomplete knowledge of the subhalo populations structure and distribution.

3.2 Gammapy ($\gamma\pi$): a Python package for γ-ray astronomy

Throughout the entirety of my thesis, I conducted the analyses using Gammapy (in the version 1.2) [14], an open-source Python package specifically designed for γ-ray data analysis and simulations and in particular it is built upon Numpy and Astropy. It serves as the core library for the Science Analysis Tool of the CTA and is also compatible with data from existing gamma-ray observatories. It is an affiliated package under development within the Astropy ecosystem, leveraging the core scientific Python tools to provide analysis and simulation capabilities for gγ-ray telescopes. However, Gammapys scope is broader, offering tools for data handling, background modeling, source detection, statistical methods, and so many more.

In particular Gammapy provides several convenient methods for DM analyses within the **darkmatter** module. These include the computation of J-factors and the calculation of expected γ-ray flux for various annihilation channels. Specifically, I used the the so-called *γ-ray spectrum at production* method, supported by the attribute *PrimaryFlux*. The name "*spectrum at production*" refers to the initial spectrum of γ-rays produced directly from DM annihilation or decay, before any subsequent interactions like propagation through interstellar medium or absorption. This module allows users to simulate this production spectrum based on different DM models and annihilation channels. In the Fig. 3.2 it can be seen the reported example in tutorial for the spectrum at production. To date, the analysis relies on theoretical computations of M.Cirelli et al. (PPPC4DMID).

```
fluxes = PrimaryFlux(mDM="1 TeV", channel="eL")
print(fluxes.allowed_channels)

fig, axes = plt.subplots(4, 1, figsize=(4, 16))
mDMs = [0.01, 0.1, 1, 10] * u.TeV

for mDM, ax in zip(mDMs, axes):
    fluxes.mDM = mDM
    ax.set_title(rf"m$_{{\mathrm{{DM}}}}$ = {mDM}")
    ax.set_yscale("log")
    ax.set_ylabel("dN/dE")

    for channel in ["tau", "mu", "b", "Z"]:
        fluxes = PrimaryFlux(mDM=mDM, channel=channel)
        fluxes.channel = channel
        fluxes.plot(
            energy_bounds=[mDM / 100, mDM],
            ax=ax,
            label=channel,
            yunits=u.Unit("1/GeV"),
        )

axes[0].legend()
plt.subplots_adjust(hspace=0.9)
plt.show()
```

Figure 3.2: The γ-ray spectrum per annihilation example taken from gammapy tutorials.

3.3 PPPC4DMID vs CosmiXs

In section 2.3 I mentioned the PPPC4DMID (hereafter PPPC) recipes to compute the *spectra at source* (namely the $\frac{dN_i^\gamma}{dE_\gamma}$) for prompt emission from DM annihilation/decay. In this part we will go deeper in the discussion to see how I made use of these simulations. In particular we will examine the differences between PPPC and the generated CosmiXs' spectra at production by computing the quantity N_γ, i.e. the number of predicted photons.

Let's start by saying that both of the analysis are theoretical calculations of the flux messenger particles emitted from DM annihilation or decay. The final product is an ASCII file .dat, named "*AtProduction-gammas.dat*" (for PPPC), at which we refer equally as energy spectra at source. These simulations are both executed using codes for the generation of high-energy physics events (known as Monte Carlo event generators, such as `Pythia`) but while for PPPC it is used the `Pythia` version 8.135, CosmiXs uses the version 8.309 implemented by the VINCIA antenna shower algorithm and feeded by amplitudes generated by the MadDM code and this is the remarkable difference. This distinction introduces several notable advancements from the particle physics perspective, such as the inclusion of **off-shell contribution** for WW, ZZ, HZ DM annihiliation/decay channels and the integration of the **polarization of the gauge bosons**, resulting in a more accurate production spectrum. We will do a step backward in the next subsection in order to understand why these contributions are important to be reported.

Without exploring all the technical details, CosmiXs, through the integration of VINCIA, introduces further innovations compared to the standard `Pythia` showering process. First, VINCIA accounts for helicity throughout the shower evolution, decomposing the contributions for each set of helicities. Additionally, it includes trilinear gauge boson interactions such as $Z^0W^+W^-$, HW^+W^-, HZZ (shown in the Fig. 3.3) and γW^+W^-, which are neglected in the standard `Pythia` shower but can actually provide significant contributions at high DM masses. These differences result in a more coherent handling of electroweak and QCD emissions, where the decay of heavy resonances like W-bosons or top quarks is fully integrated within the shower machinery, affecting the kinematic distributions of the decay products. Moreover, CosmiXs's study [41] demonstrated that the photon yield in leptonic channels is better estimated at low energies, addressing a known underestimation in the version of `Pythia` used by PPPC.

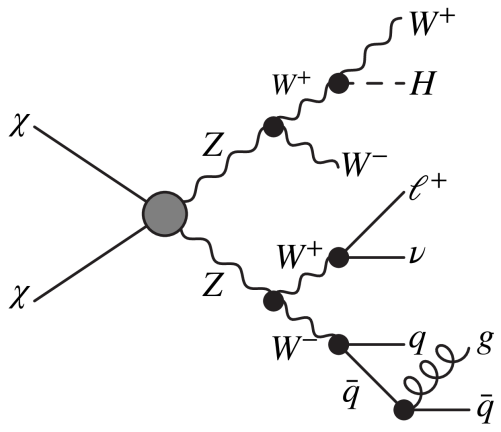

Figure 3.3: A Feynman diagram illustrating an event where two DM particles (χ) annihilate into two Z bosons. Subsequently, the Z bosons emit EW radiation, resulting in the production of additional bosons that later decay into fermions. This is an example of a process included in VINCIA. Credit: [41]

3.3.1 Phenomenological tools from particle physics

Let's consider a generic DM annihilation process:

$$\chi\chi \to [X_1 X_2 \dots X_N] \to \left(Y_{11} \dots Y_{1q}\right) \dots \left(Y_{N1} \dots Y_{Nq_N}\right).$$

The intermediate states X_i (quarks, gluons, leptons, heavy resonances like $W^{\pm}$, Z^0, H, or the top quark) decay into stable particles Y_{ij}, including photons, positrons, neutrinos, and antiprotons, which persist over astrophysical timescales. The physical modeling of stable particles depends on the nature of the intermediate particles X_i and/or decay products, Y_{ij}.

For electrically charged particles, QED bremsstrahlung (VIB) can occur, leading to additional photon emission, particularly in soft and quasi-collinear regions. High-energy photons ($E_\gamma \to M_\chi$) are emitted when the angle between the parent particle and photon is small. Furthermore, $\gamma \to \bar{f} f$ can occur with lower probabilities at low photon virtualities. If allowed by phase space, fermions emit $W^{\pm}$, Z^0, or H bosons. Similarly, QCD bremsstrahlung produces gluons ($X \to Xg$) and quark-antiquark pairs ($g \to \bar{q}q$). For all the associated Feynman diagrams have a look at the Appendix C.

Stable particle production primarily occurs through the hadronization via QCD bremsstrahlung, which accounts for most ($\sim 90\%$) of particle production. Electroweak boson radiation (EWBR) and QED final state radiation (FSR) contribute subleading effects. The relative contribution of these processes depends on the DM mass and the annihilation/decay channel. For example, for $M_\chi = 100\,\text{TeV}$ annihilating into $b\bar{b}$, γ-ray production mainly arises from neutral pion decays following hadronization, while at lower masses, FSR dominates in leptonic channels.

From a computational perspective, `Pythia` models an e^+e^- collision with a beam energy $E_{\text{beam}} = M_\chi$, producing a resonance $\mathscr{R}$ with energy $2M_\chi$, which decays into a $b\bar{b}$ pair. This pair undergoes QED and QCD showers, generating final-state particles.

For DM annihilation/decay into W^+W^- or Z^0, the standard "on-shell" treatment assumes production at the rest mass of the gauge boson, described by a Breit-Wigner distribution. However, for M_χ below the gauge boson mass, this resonance approach cannot account for off-shell production. Off-shell gauge bosons open additional decay channels, altering the resulting spectra. Moreover, gauge bosons, being spin-1 particles, have three polarization states: two transverse (± 1) and one longitudinal (0). Polarization effects impact the angular and momentum distribution of the decay products. For example, longitudinally polarized bosons may produce $b\bar{b}$ pairs with different angular distributions compared to transversely polarized ones, as one can conclude from Fig. 3.4.

3.3.2 Structure of spectra files

PPPC and CosmiXs generate spectra for each cosmic messenger (six in total for CosmiXs: antiprotons, positrons, γ rays, and the three neutrino species; whereas for PPPC, there is an additional one, the antideuteron)[1] in ASCII-format. The annihilation/decay spectra are provided in logarithmic scale

[1] Why they generated antiparticles? This is because their scarcity in the Universe reduces astrophysical background, making it easier to identify signals and relevant energy ranges.

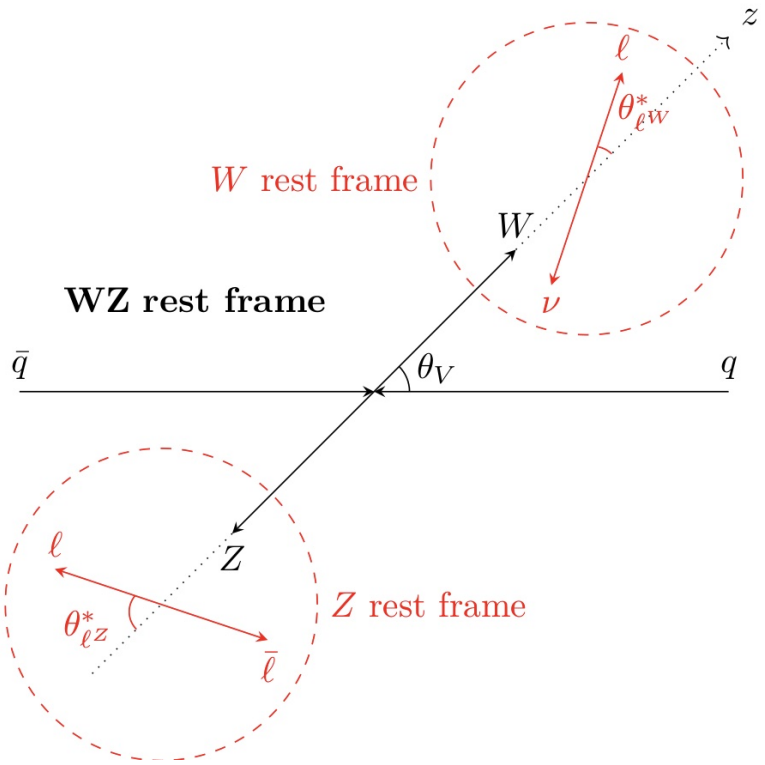

Figure 3.4: The polarization states of W and Z bosons affect the directions of decay product emission. Transversely polarized bosons emit decay products perpendicularly to the motion, while longitudinally polarized bosons emit them more aligned with the original direction. Source: ATLAS Collaboration/CERN, adapted from [46].

for DM masses between 5 GeV and 100 TeV. Hence, in the datafiles one can find a certain number of columns, where the first is the DM mass in GeV and the others include the spectrum in units of $dN/dlog_{10}(x)$ for each annihilation channel, for instance: $dN/dlog_{10}(x)[b]$, $dN/dlog_{10}(x)[W]$[2], etc., as one can see in the Fig. 3.5.

1	# DM	Log10[x]	dNdLog10x [eL]	dNdLog10x [eR]	dNdLog10x [e]
2	5	-8.9550	0.0000000	0.0000000	0.0000000	0.0000000	0.0000000
3	5	-8.8650	0.0000000	0.0000000	0.0000000	0.0000000	0.0000000
4	5	-8.7750	0.0000000	0.0000000	0.0000000	0.0000000	0.0000000
5	5	-8.6850	0.0000000	0.0000000	0.0000000	0.0000000	0.0000000
6	5	-8.5950	0.0000000	0.0000000	0.0000000	0.0000000	0.0000000
7	5	-8.5050	0.0000000	0.0000000	0.0000000	0.0000000	0.0000000
8	5	-8.4150	0.0000000	0.0000000	0.0000000	0.0000000	0.0000000
9	5	-8.3250	0.0000000	0.0000000	0.0000000	0.0000000	0.0000000
10	5	-8.2350	0.0000000	0.0000000	0.0000000	0.0000000	0.0000000
11	5	-8.1450	0.0000000	0.0000000	0.0000000	0.0000000	0.0000000
12	5	-8.0550	0.0000000	0.0000000	0.0000000	0.0000000	0.0000000
13	5	-7.9650	0.0000000	0.0000000	0.0000000	0.0000000	0.0000000
14	5	-7.8750	0.0000000	0.0000000	0.0000000	0.0000000	0.0000000
15	5	-7.7850	0.0000000	0.0000000	0.0000000	0.0000000	0.0000000
16	5	-7.6950	0.0000000	0.0000000	0.0000000	0.0000000	0.0000000
17	5	-7.6050	0.0000000	0.0000000	0.0000000	0.0000000	0.0000000

Figure 3.5: Example of the ASCII file "*AtProduction-Gamma.dat*" from CosmiXs.

There is a difference between the two spectra datafiles, due to the new implementations of CosmiXs. Specifically:

[2]The x stands for the fraction $x = \frac{E}{M_\chi}$ i.e. the kinetic energy divided by the DM mass.

- **PPPC** has 28 primary annihilation channels, namely
  - Fermionic channels:

$$\chi\chi \to e_L^+e_L^-, e_R^+e_R^-, e^+e^-, \mu_L^+\mu_L^-, \mu_R^+\mu_R^-, \mu^+\mu^-, \tau_L^+\tau_L^-, \tau_R^+\tau_R^-, \tau^+\tau^-, q\bar{q}(q=u,d,s), c\bar{c}, b\bar{b}, t\bar{t}.$$

  - Bosonic channels:

$$\chi\chi \to W_L^+W_L^-, W_T^+W_T^-, W^+W^-, Z_LZ_L, Z_TZ_T, ZZ, gg, \gamma\gamma, hh, \nu_e\nu_e, \nu_\mu\nu_\mu, \nu_\tau\nu_\tau,$$

$$VV \to 4e, VV \to 4\mu, VV \to 4\tau.$$

- **CosmiXs** also includes spectra for new channels that were not previously calculated, such as γZ and HZ, bringing the total number of annihilation channels to 29. Specifically they are:
  - Fermionic channels:

$$\chi\chi \to e_L^+e_L^-, e_R^+e_R^-, e^+e^-, \mu_L^+\mu_L^-, \mu_R^+\mu_R^-, \mu^+\mu^-, \tau_L^+\tau_L^-, \tau_R^+\tau_R^-, \tau^+\tau^-, \nu\bar{\nu},$$

$$u\bar{u}, d\bar{d}, s\bar{s}, c\bar{c}, b\bar{b}, t\bar{t}.$$

  - Bosonic channels:

$$\chi\chi \to \gamma\gamma, gg, W^+W^-, W_L^+W_L^-, W_T^+W_T^-, ZZ, Z_LZ_L, Z_TZ_T, HH, \gamma Z, HZ.$$

  From the list of the generated channels one can see that CosmiXs takes in account helicity of gauge bosons (thanks to the VINCIA shower plugin). In the latter it is integrated off-shell effects for WW, ZZ, HZ producing four fermions and covering DM masses from 5 GeV to M_X, with $X = W, Z$. Furthermore it is included the running quark masses for the quark annihilation channels and importantly, for the one-loop induced annihilation channels ($\gamma\gamma, gg, \gamma Z$), they used full one-loop form factors.

3.3.3 CosmiXs' influence on N_γ

In the field of VHE astrophysics, one of the most experimentally significant quantities is the number of the detected γ photons, N_γ, as it is crucial indicator of the underlying physical processes occuring in cosmic enviroments. In this part we will see how I calculated this quantity and what I expected to find in the difference between PPPC and CosmiXs' prediction, also exploring further CosmiXs' results.

The total photon yield N_γ can be derived from the differential spectral distribution by integrating it over energy:

$$N_\gamma = \int_{E_{\min}}^{E_{\max}} \frac{dN}{dE} dE. \tag{3.1}$$

In this context, firstly I read the ASCII datafiles with the `PrimaryFlux` model from **gammapy.astro.darkmatter** module, which is generically used to describe the expected photon flux for a specific DM mass m_χ and annihilation channel. Then, I plotted the spectrum with the mass (m_{DM}) in TeV on the x-axis and the quantity $x^2 \frac{dN}{dE}$ on the y-axis, (where $x = \frac{E}{m_{DM}}$ is the usual the dimensionless ratio). I selected three specific values of masses: 0.1 TeV, 1.0 TeV, and 100 TeV for the three most valuable annihilation channel I mentioned in the previous subsection, i.e. $b\bar{b}$, $\tau^+\tau^-$, and W^+W^-.
The integration was performed numerically using the related *integral* method of `PrimaryFlux` over the energy range defined by $E_{min} = 0.001$ TeV and $E_{max} = 100$ TeV for a set of DM masses $mDMs = [0.1, 0.3, 1.0, 10.0, 30.0, 60.0, 100.0]$ TeV and for the previous annihilation channels. I calculated the ratio between the integrated fluxes from CosmiXs and PPPC and then I created a plot with $m_{DM}[TeV]$ on x-axis and Ratio on y-axis, in order to better visualize the differences.
Lastly, I report here the Fig. 7 from [41]: this is important to understand why CosmiXs' spectra are more accurated than PPPC's one. The plot shows the effect of the polarization for a $M_\chi = 1$ TeV

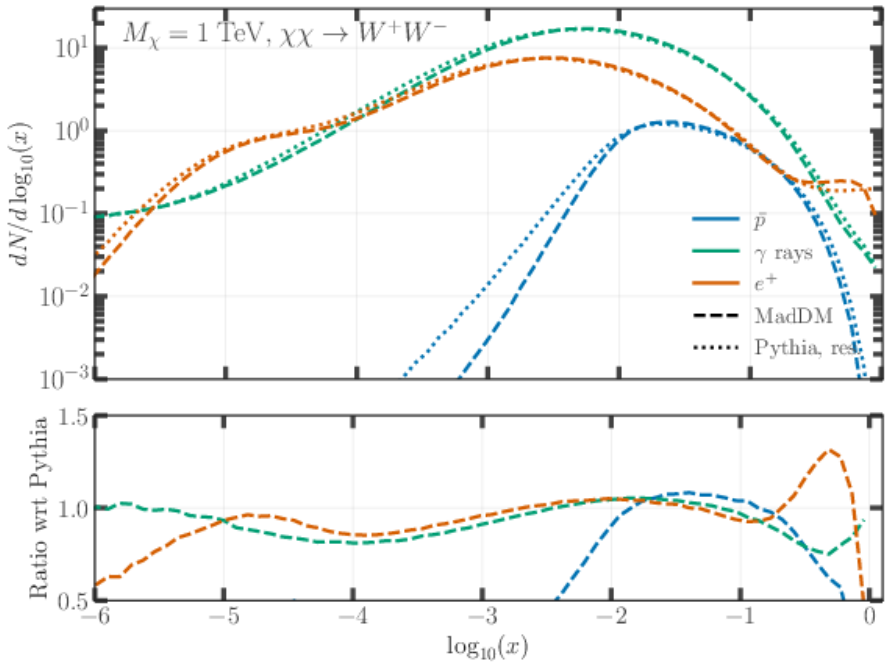

Figure 3.6: Comparison between the spectra generated with the `Pythia` resonance method (dotted curves) and with the MadDM code (dashed curves) for the W^+W^- channel for a $M_\chi = 1TeV$.

on the W^+W annihilation channel and calculate the spectrum for the production of γ-rays, $\bar{p}$ and e^+. The comparison between MadDM and PPPC's resonance method shows significant differences in the predicted spectra, especially around the peak at lower energy scales ($log_{10}(x) \sim$ -4 to -2), where discrepancies reach 20-30% for γ-rays, in particular. Clearly, the shape of the photon spectrum in 3.6 has a direct influence on the total photon yield because, as said, N_γ is the result of integrating these spectra over energy. Models like MadDM and Vincia, which account for EWBR more accurately, predict a higher N_γ compared to older models like PPPC.

3.4 Statistical tools from IACTs

In the section 2.4.2 I exploited the Hillas method, i.e. the technique used to do the event reconstruction of the image shower. This is just a piece of the typical workflow of an IACTs analysis. One can see the whole picture from the Fig. 3.7: starting from the shower images, the variable s (the expected number of signal events) is derived, which is then used for deducing the flux of γ-ray. The final

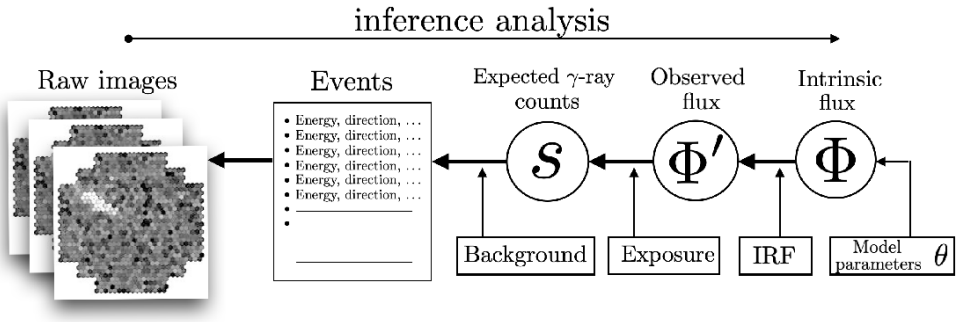

Figure 3.7: Schematic workflow of the inference analysis used to estimate the intrinsic γ-ray flux Φ and its parameters θ from the recorded images. The acronym IRF stands for Instrument Response Function, which is not considered in this thesis. The bold arrows (right to left) represent the cause-and-effect relationship, while the goal of the inference analysis (thin arrow, left to right) is to invert this relationship. Adapted from [47].

result of the statistical analysis using the Hillas method provides a list of candidate γ-ray events[3]. Assuming no background contamination, the total number n of events in the list follows a Poisson distribution but, realistically, the most observed events are caused by hadronic cosmic rays with only a small fraction attributed to γ rays (for a bright source is of the order of 10^{-3}). Hence, to infer the γ-ray flux from the event list, an accurate estimate of the remaining background contamination is necessary. The most common scenario is when the background is unknown. It requires defining two regions: the region of interest (ROI), also known as the target or ON region, and a background control region called the OFF region, which is assumed to contain no signal events. The ON and OFF regions provide independent counts, N_{ON} and N_{OFF}[4] respectively, where the latter is ideally free from any signal events. A normalization factor α is introduced to account for differences, such as acceptance and exposure time, between the ON and OFF regions.
The goal of background modeling is to determine α and N_{OFF}, which are then used to estimate the signal s and detection significance. There are two common methods used to obtain OFF counts:

- *On-Off background method*: OFF counts are collected from (typically consecutive) observations made under identical conditions, with $\alpha = t_{\mathrm{on}}/t_{\mathrm{off}}$, where t_{on} and t_{off} are the exposure times for the ON and OFF observations, respectively. The advantage of this method is that it makes no assumptions about acceptance, as long as it is identical for both ON and OFF regions. However, this technique has some disadvantage, for instance the time difference and the inefficiency since for half the time the source is not observed.

[3]This includes estimates of their energy E_{est} and arrival direction.
[4]Both N_{ON} and N_{OFF} are random variables that obey the Poisson statistics.

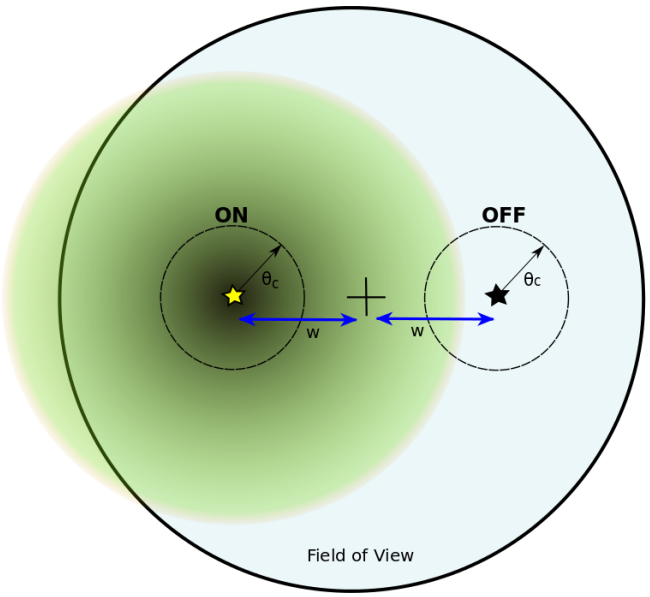

Figure 3.8: Schematic configuration of the FoV during wobble mode observations. The telescope pointing (black cross) has an offset distance w w.r.t. the center of the source under study (yellow star). Signal (ON) region is defined as a circle around the center of the source, with angular size θ_c. One background control region (circular region around OFF, black star) is defined with same angular size, symmetrically w.r.t. the signal region. The leakage effect is schematically shown where, for moderately extended source (green area), signal events are also expected to be reconstructed inside OFF. Credit: [48].

- *Wobble method*: OFF counts are taken from regions symmetrically positioned at the same distance from the center of the field of view on a run-by-run basis. Each OFF region is created by reflecting the ON region relative to the FoV center, indeed it is also known as reflected-region method. Hence, the ON and OFF data are taken simultaneously. The Fi 3.8 shows the configuration adopted by the telescope during this mode.

Operationally a new parameter, θ, is introduced and it is defined as the angular distance between the expected source position and the reconstructed position for each event. The distribution of θ^2 (referred to as the θ^2-plot) indicates the presence of a signal if it shows a peak near zero, suggesting that the events originate from the source direction. A signal region is defined by applying a cut on θ^2, creating a circle of radius θ around the source position, this is the ON region.
Given N_{ON} events in the ON region and N_{OFF} events in the OFF region (distributed over $1/\alpha$ OFF positions), the excess signal is calculated as:

$$N^{\gamma}_{\mathrm{exc}}(E) = N_{\mathrm{ON}} - \alpha N_{\mathrm{OFF}}. \tag{3.2}$$

The obtained quantity, $N^{\gamma}_{\mathrm{exc}}(E)$, estimates the excess of events that can be attributed to the signal after subtracting the expected contribution from background noise.
The final aim of this *interference analysis* is to estimate the strength of the signal s. This is done using a likelihood function that models both the ON region (which of course contains the signal plus background) and the OFF region (which contains only the background). This can be used for

hypothesis examination, in particular for testing the $s = 0$ hypothesis. The latter corresponds to the null hypothesis, where no signal is present in the data, i.e., any excess observed in the ON region is purely due to background fluctuations. By testing against this null hypothesis, we can derive the detection significance, which tells us whether there is enough evidence to reject the null hypothesis in favor of a non-zero signal s. The formula 3.3 provides a way to assess the significance of the detection based on this likelihood analysis.

$$S = \pm 2 \left[N_{\mathrm{ON}} \log \left(\frac{(1+\alpha) N_{\mathrm{ON}}}{\alpha (N_{\mathrm{ON}} + N_{\mathrm{OFF}})} \right) + N_{\mathrm{OFF}} \log \left(\frac{(1+\alpha) N_{\mathrm{OFF}}}{N_{\mathrm{ON}} + N_{\mathrm{OFF}}} \right) \right]^{\frac{1}{2}}, \tag{3.3}$$

where the sign is arbitrarily chosen to be positive when the excess $N_{\mathrm{ON}} - \alpha N_{\mathrm{OFF}}$ is positive. This expression is the well-known Li&Ma formula for computing the detection significance in ON/OFF measurements. The Li&Ma significance S quantifies how confidently we can claim a detection, based on the excess events observed in the ON region compared to the expected background from the OFF region, giving a reliable measure even when the number of events is small. In the formula, the normalization factor α accounts for differences in exposure and acceptance between the ON and OFF regions, ensuring a fair comparison. A significance of $S \geq 5\sigma$ is typically considered a strong detection, while smaller values may indicate evidence for a signal but not a conclusive discovery. Usually, in these cases, one can determine the upper limit (UL) for the number of γ-rays produced by DM annihilation, which corresponds to a 95% Confidence Level (C.L.). This means that in 95% of events, the non-null hypothesis (DM signal presence) is verified, while the null hypothesis (no DM signal or no observed excess) is verified in 5%of events. When no detection is observed, the UL on the number of signal events in the ROI can be translated into ULs on the expected $< \sigma v >$. Practically, the UL is a one-sided confidence interval, meaning it is a way to say: "*if there were a signal, its maximum compatible flux with the data would be this*".[5] Typically this is done at a certain confidence level (e.g., 95%), indicating a high probability that the true flux does not exceed this limit. By comparing this limit with the predicted flux from DM, one can decide whether the data support or exclude a particular theoretical model.

3.4.1 Effective Area

At first approximation, the geometrical area of an IACT can be described as the mirror surface of the telescope that images the shower. However, there is much more to consider: the effective collection area is related to the detection probability $P_\gamma(E, r, \theta)$, which depends on the energy E, the zenith angle θ of the γ-ray, and the impact parameter r, defined as the distance from the telescope to the center of the light pool. The flux observed by the telescope is a function of the detection probability and the flux of the γ source:

[5] IACTs operate in a regime of low statistics, where the number of observed events can be very low and, moreover, signals might be faint. In these cases, establishing UL is the best way to quantify the experiment's sensitivity.

$$\frac{dN_\gamma}{dE} = \int \phi \int r P_\gamma(E,r,\theta)\Phi(E,\theta)\,dr = 2\pi \int r P_\gamma(E,r,\theta)\Phi(E,\theta)\,dr.$$

Hence, the A_{eff} is the area of an equivalent instrument that can detect the same rate of γ-rays as the actual detector, assuming 100% efficiency. Essentially, it represents the area of an instrument that would detect all γ-rays perpendicular to its surface.

Practically, the A_{eff} is calculated through MC simulations. We can express the detection probability as follows:

$$P_\gamma(E,x,y,\theta) = \frac{N_{\gamma,\text{final}}(x,y)}{N_{\gamma,\text{sim}}(x,y)},$$

where $N_{\gamma,\text{sim}}(x,y)$ represents the number of γ-rays uniformly simulated in the simulated area A_{MC}: $N_{\gamma,\text{sim}}(x,y) = \frac{N_{\gamma,\text{sim}}}{A_{\text{MC}}}$. Substituting it into the previous expression one will get:

$$A_{\text{eff}} = \frac{N_{\gamma,\text{final}}}{N_{\gamma,\text{sim}}} A_{\text{MC}}, \tag{3.4}$$

where we identify the global efficiency ε as the ratio of the number of observed γ-rays to the number of simulated γ-rays.

However, due to the dependencies present in the probability $P_\gamma(E,x,y,\theta)$, the A_{eff} also depends on the energy of the γ-ray, its direction (in terms of zenith angle Z_d and azimuth A_z), and the angle between its direction and the telescope axis. The higher the energy, the greater the number of secondary particles produced, and thus the higher the probability of detection (increasing A_{eff}). The higher the zenith angle, the farther the γ-ray travels before producing a cascade detectable by the telescope, resulting in a wider Cherenkov cone.

It is important to clarify the difference between *intrinsic* and *real* flux. Intrinsic flux refers to the flux of energy emitted by a source without considering any external effects, such as absorption or scattering. It represents the "true" emission characteristics of the source (i.e. the definition I gave in Eq. (2.1)). Real flux takes into account the actual observed flux of particles or energy as it arrives at a detector or observer. This includes all effects such as absorption, scattering, and distance from the source. It is what is measured in experiments and in observations.

What I will test in this part is how the intrinsic flux from simulations, particularly for DM annihilation channels $b\bar{b}$ and $\tau^+\tau^-$, may be altered when rescaled by A_{eff} of each IACT, such as MAGIC, CTA, H.E.S.S., and Veritas. For the first three mentioned experiments I used the software *WebPlotDigitizer* on the plot 4 from [49] to extract the points of the curves, collecting them in a *.ecsv* file. For Veritas I used the solid black line from plot 3 (2012-today) from this link, which summarizes the sensitivity and the performance of the instrument. Therefore, these data files for A_{eff} are the same I will use in the next and most important part of this work.

In order to obtain these results I fixed two values of m_{DM}: 1.0 TeV and 10.0 TeV. The structure of the plots will be the following:

- on the top rows one will see the intrinsic flux from PPPC for the two values of mass and for the channels $b\bar{b}$ and $\tau^+\tau^-$ in dashed lines;
- on the bottom row there will be the comparison: in addition to the dashed lines one will find the same curves but in solid, which represents the real fluxes. To be more explicit I added the specific effective area in dashed black in the same plot.

The intrinsic flux from simulations represents the theoretical prediction of γ-ray emission from DM, but when rescaled by the A_{eff} of IACT telescopes, a reduction in flux is observed. This occurs because the A_{eff} reflects the physical limitations of the observatory, including factors such as energy, angle of incidence, and the telescope's specific characteristics. It highlights the instrument's reduced sensitivity at low and high energies, due to components like mirror size, detection electronics, and environmental effects.

3.5 Cross Section Ratio and DM Predictions

Suppose one has observed the target for an effective time of $T_{\rm obs}$ in seconds. After performing the analysis, the results are an optimal set of filters based on the Hillas parameters and the estimated energy $E_{\rm est}$. Hence, one has obtained a number of excess events $N_{\rm exc}$ with a significance that is below 5σ. The next step would be to estimate the UL on the flux $\Phi_\gamma^{UL}(E)$ corresponding to the observational data. For this purpose, one can apply the Rolke method, described in [50]. So that the corresponding number of excess events (which we can also refer as *signal counts* s_i), denoted as $N_{\rm EXC}^{\gamma,UL}$, is:

$$N_{\rm EXC}^{\gamma,UL} = \int_{\Delta E_i'} dE' \int_{\Delta E} dE \Phi_\gamma^{UL}(E) \cdot A_{\rm eff}(E) \cdot T_{obs} \cdot G(E,E'). \tag{3.5}$$

This is the integral of the expected flux over a given energy range, combined with the instrumental response. The expression $G(E,E')$, namely the *transfer (or response) function*, quantifies the probability that an event with true energy E will be reconstructed with a detected energy E'. It connects the true energy of the incoming γ-rays to the measured one, by modeling how well the instrument can detect it. The Eq. (3.5) represents a general formulation that incorporates the response of the instrument, through the inclusion of $G(E,E')$.
Thus I refer back to the first Eq. of 2.1 for the theoretical (or *intrinsic*) flux, as it can be substituted into the expression for $\Phi_\gamma^{UL}(E)$ of the Eq. (3.5). Moreover applying a *benchmark approach*, i.e. the $BR_i = 1$ for the i channel and zero for all the others. In this way I obtain:

$$N_{\rm EXC}^{\gamma,UL}[E_0, m_\chi] = \frac{T_{obs} J(\Omega) \langle\sigma v\rangle_i^{UL}}{8\pi m_\chi^2} \int_{\Delta E_i'} \int_{\Delta E} A_{eff}(E) \cdot G(E,E') \cdot \frac{dN_i^\gamma}{dE_\gamma}\, dE. \tag{3.6}$$

Since the terms T_{obs}, $J(\Omega)$, m_χ, $A_{eff}(E)$ are independent of the annihilation channel, what differentiates each channel is primarily the cross-section $\langle\sigma v\rangle_i^{UL}$ and the photon spectrum $\frac{dN_i^\gamma}{dE_\gamma}$. Thus, the quantity $N_{\rm EXC}^{\gamma,UL}[E_0, m_\chi]$ is designed to be consistent across different channels, meaning that the final

expected number of events should, in principle, be equal for all annihilation DM channels under the same observational conditions.

To determine the UL on the cross section, $\langle\sigma v\rangle_i^{UL}$, a likelihood analysis is performed. The analysis uses the observed counts n_i, the expected signal counts s_i (or $N_{\rm EXC}^{\gamma,UL}$), and the expected background counts b_i in each i-th energy bin. The log-likelihood function is expressed as follows:

$$-2\log\mathscr{L} = 2\sum_i (s_i + b_i - n_i \log(s_i + b_i)) + C,$$

where C is a constant independent of the model parameters. Since C does not vary with changes in the parameters of interest, such as the cross-section in this case, it can be omitted during the UL estimation.

At this point, the UL is obtained by imposing

$$-2\log\mathscr{L} = 2\sum_i (s_i + b_i - n_i \log(s_i + b_i)) = \lambda\,.$$

If the likelihood is properly *profiled*, i.e., its maximum value is subtracted, ensuring that $-2\log\mathscr{L}$ is always positive, a one-sided 95% confidence level UL is obtained with $\lambda = 2.71$.

Recalling the integral in (3.6) as:

$$A_i = \frac{T_{obs} J(\Omega)}{8\pi m_\chi^2} \int_{\Delta E_i'} \int_{E_0}^{m_\chi} A_{eff}(E) \cdot G(E,E') \cdot \frac{dN_i^\gamma}{dE_\gamma}\, dE, \tag{3.7}$$

one can see:

$$N_{\rm EXC}^{\gamma,UL} \equiv s_i = \langle\sigma v\rangle \int_{\Delta E_i'} dE' \int dE\, A_{eff}(E) \cdot G(E,E') \cdot \frac{dN^\gamma}{dE_\gamma} \cdot \frac{T_{obs} J}{8\pi m_\chi^2} \equiv \langle\sigma v\rangle A_i, \tag{3.8}$$

so that the UL on $\langle\sigma v\rangle$ is obtained by imposing

$$2\sum_i (\langle\sigma v\rangle A_i + b_i - n_i \log(\langle\sigma v\rangle A_i + b_i)) = \lambda\,.$$

For simplicity, we will denote the velocity-averaged cross-section using the variable σ, and use $\hat{\sigma}$ to represent the cross-section that maximizes the likelihood, which is found by imposing that the first derivative of the log-likelihood is zero, i.e.,

$$\sum_i A_i \left(1 - \frac{n_i}{A_i\hat{\sigma} + b_i}\right) = 0 \tag{3.9}$$

By performing a Taylor expansion till the second order of the expression in Eq. 3.8 around $\hat{\sigma}$, we have

$$-2\log\mathscr{L} \simeq \sum_i A_i^2 \frac{n_i}{(b_i + A_i\hat{\sigma})^2} (\sigma - \hat{\sigma})^2 + C = \lambda, \tag{3.10}$$

where again C is a constant independent of the model parameter σ, which can be set to zero to ensure that $-2\log\mathscr{L}$ is zero when $\sigma = \hat{\sigma}$. We found therefore that the UL on σ is given by

$$\sigma^{UL} \simeq \hat{\sigma} \pm \sqrt{\frac{\lambda}{\sum_i A_i^2 \frac{n_i}{(b_i + A_i\hat{\sigma})^2}}}, \tag{3.11}$$

where the '+' sign must be taken to ensure the cross section to be positive.
It is worth noticing that for one bin in energy we have from Eq. 3.9

$$\hat{\sigma} = (n-b)/A, \tag{3.12}$$

and therefore

$$\sigma^{UL} \simeq \frac{n-b}{A} + \sqrt{\lambda}\frac{\sqrt{n}}{A} = \frac{n + \sqrt{\lambda}\sqrt{n} - b}{A} \propto \frac{1}{A}. \tag{3.13}$$

For one energy bin, we have analytically proven the expression :

$$\frac{\langle\sigma v\rangle_i^{UL}}{\langle\sigma v\rangle_j^{UL}} = \frac{A_j}{A_i}. \tag{3.14}$$

It suggests a proportional relationship between the ULs of the velocity-averaged annihilation cross sections $\langle\sigma v\rangle^{UL}$ for two different annihilation channels i and j, based on the ratio of their expected number of photons after scaling by the effective area (what I denoted by A_i).
A straightforward application of this formula would be to predict other annihilation channels based on existing data. But more specifically the Eq. 3.14 could have other applications:

- **put constraints on DM models**, i.e., having a model where DM annihilates into various channels (e.g., $\chi\chi \to b\bar{b}, \tau^+\tau^-, W^+W^-$, this relation helps adjust the branching ratios based on experimental limits, ensuring that predicted cross sections align with experimental constraints for different channels;

- **text mixed-channel hypotheses** i.e. helps verify if the predicted mix of annihilation into different channels (e.g., leptonic vs hadronic) is consistent with observational ULs.

I aim to test if I can predict one annihilation channel from another using γ-rays as cosmic messengers, relying on the PPPC4DMID predictions for the spectra. Following the definition for A_i, I multiplied the $A_{eff}(E)$ by $\frac{dN}{dE}$ and performed an integral from $E_0 = 0.01TeV$ to m_{DM}. Once obtained the expected N_γ for the two channels, the ratio of these areas should, in principle, match the inverse ratio of the cross sections:

$$\langle\sigma v\rangle^{UL}_{\tau^+\tau^-} = \frac{A_{b\bar{b}}}{A_{\tau^+\tau^-}} \cdot \langle\sigma v\rangle^{UL}_{b\bar{b}}, \tag{3.15}$$

for instance if one wants to predict $\tau^+\tau^-$ mode from $b\bar{b}$ channel. The projection is considered successful if the estimated curve falls within the bounds of the experimental confidence level (CL).

This process can be broken down into two stages[6]:

- initially, I performed an instrument comparison using data from several telescopes (MAGIC, CTA, H.E.S.S., VERITAS) to predict the $\tau^+\tau^-$ annihilation channel from $b\bar{b}$. The Python code is designed to allow users to input general data (for the two mentioned channels) from the four telescopes, which then automatically associates the corresponding A_{eff}. This process facilitates the estimation of the DM. Afterward, CL data from the experiment should be added. This was accomplished using the following data sources:
  - CTA: Perseus Cluster (2023) prospects [51].
  - MAGIC: Observation of Segue 1 (2022) [52].
  - H.E.S.S.: MultidSphs study (2020) [53].
  - VERITAS: MultidSphs observation (2017) [54].
- for the second part, I experimented by plotting various channels for different experiments for instance for the MAGIC observation of Segue 1, I performed an inverse process, predicting the $b\bar{b}$ annihilation channel starting from the $\tau^+\tau^-$ channel. Additionally, I utilized the same dataset to predict W^+W^- annihilation both from the $b\bar{b}$ channel and directly from $\tau^+\tau^-$. In the analysis of the CTA data for the Perseus Cluster, I similarly predicted the $b\bar{b}$ channel from $\tau^+\tau^-$ annihilation.

In all cases, the original curve is depicted in solid red, the comparison curve in solid black, and the predicted curve in dashed black. The general structure of the plots will be the so-called *Brazilian plot*, where I will display $m_{DM}[TeV]$ against $\langle\sigma v\rangle\,[cm^{-3}s^{-1}]$ while incorporating the 68% and 95% CL bands as shaded regions (green for the first, yellow for the second). Sometimes it could be present also a central line, named H_0: it represents the median of the expected sensitivity in the absence of a signal (null hypothesis). Each Brazilian plot is accompanied by a second plot on the right, that displays and quantifies the two ratios from equation (3.14).

[6] All the mentioned data files are taken from `gDMbounds`.

Chapter 4
RESULTS

In this chapter, I will present the outcomes of the methodologies and analyses detailed in the previous chapter, focusing on the contributions made to the `gDMbounds` project. I will follow the very same structure outlined in the previous chapter. Hence, I will first discuss the results of the γ-ray spectrum calculations derived from the *CosmiXs* model, emphasizing the predicted photon counts N_γ. A comparative analysis will be provided, juxtaposing these findings with those generated by the earlier *PPPC* model, highlighting significant differences and improvements. Finally, I will showcase the methodology employed to predict the $\tau^+\tau^-$ DM channel, utilizing observations from the $b\bar{b}$ channel as a basis for projection and for the project. This segment will detail the computational techniques used to broaden the study across various annihilation channels and experiments, demonstrating the versatility of the `gDMbounds` portal.

4.1 PPPC4DMID vs CosmiXs

As already stated, I firstly derived the PPPC and CosmiXs spectra by using the `PrimaryFlux` module from *Gammapy* for three DM annihilation channels, $b\bar{b}$, $\tau^+\tau^-$, and W^+W^-. I report the PPPC simulations in the Fig. 4.1a. One can see that going higher in DM mass, m_{DM}, the predicted differential fluxes are more prominent from the W^+W^- channel, while at lower masses $b\bar{b}$ and $\tau^+\tau^-$ dominates. Another important thing to notice from these spectra is that the peak of the energy shifts to higher energy as the m_{DM} increases. This is expected since heavier DM particles produce higher-energy final states upon annihilation/decay. The $b\bar{b}$ channel (**solid blue line**) generally has a softer spectrum compared to the other channels. This means that, after DM annihilation into $b\bar{b}$, more energy is distributed at lower energy. The $\tau^+\tau^-$ channel (**orange dashed line**) has a harder spectrum, peaking at higher energy compared to the $b\bar{b}$. One could expect this because the τ, being lighter than quarks, tends to produce more energetic photons and secondary particles. Finally, the W^+W^- channel (**black dotted lines**) becomes significant for larger DM masses, due to its higher mass compared to the others annihilation modes.

The Fig. 4.1b refers to CosmiXs' results. This second plot highlights a model where the DM annihilation spectra exhibit sharper energy cutoffs, higher overall amplitudes, and relatively flatter spectra compared to the previous graph. These differences, particularly the sharp cutoff at $E = m_{DM}$, suggest a stricter constraint on the maximum energy of annihilation products, which could have significant implications for experimental searches for DM annihilation signals. If we focus on the $m_{DM} = 100TeV$ subplot, the $b\bar{b}$ channel shows a peak an order of magnitude larger than in the previous simulations. The very same pattern holds for the other channels, though the amplitude differences are less pronounced for the $\tau^+\tau^-$. Generically, the shape of the spectrum for the selected channels is relatively flat before the cutoff, suggesting a more uniform energy distribution compared to the previous, where

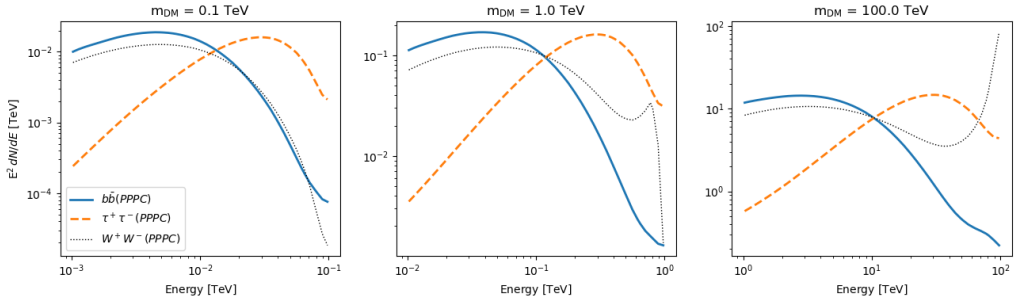

(a) PPPC spectra.

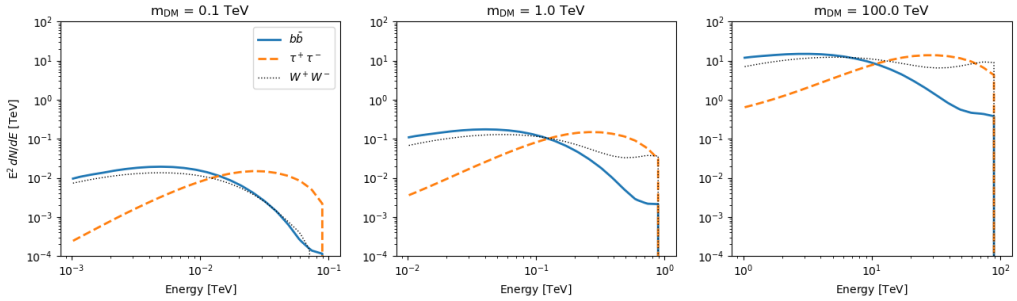

(b) CosmiXs spectra.

Figure 4.1: Predicted energy spectrum in units of TeV as a function of the energy for three different DM particle masses in logarithmic scale. Masses are set to be 0.1 TeV, 1.0 TeV, and 100.0 TeV, as indicated at the top of each subplot

they exhibit a more sharp decrease. As happened in the previous plot, the relative contribution of the different channels changes with DM mass.

To illustrate these differences more clearly, I overlaid the spectra on a single plot for direct comparison and you can see it in the Fig. 4.2. For the $b\bar{b}$ channel, the CosmiXs curves (dashed) are consistently lower than the PPPC ones (solid), especially at lower energies, indicating a different prediction for the annihilation spectrum. However, at higher energies, the two models tend to converge, particularly for larger DM masses. This convergence may imply that both models predict similar behavior in this regime, where the influence of particle annihilation is less significant. The $\tau^+\tau^-$ and W^+W^- channels follow a similar trend, with CosmiXs slightly underestimating the PPPC model at the spectrum's peak, but the discrepancy diminishes for increasing mass.

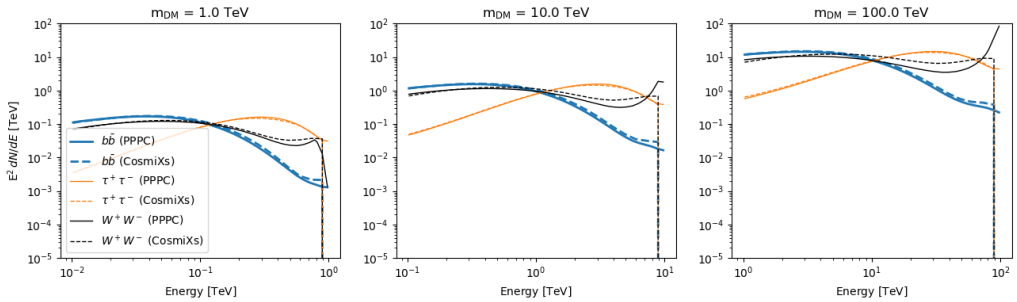

Figure 4.2: Overlaid predicted energy spectrum, where solid lines indicate the PPPC simulations and dashed lines are for CosmiXs.

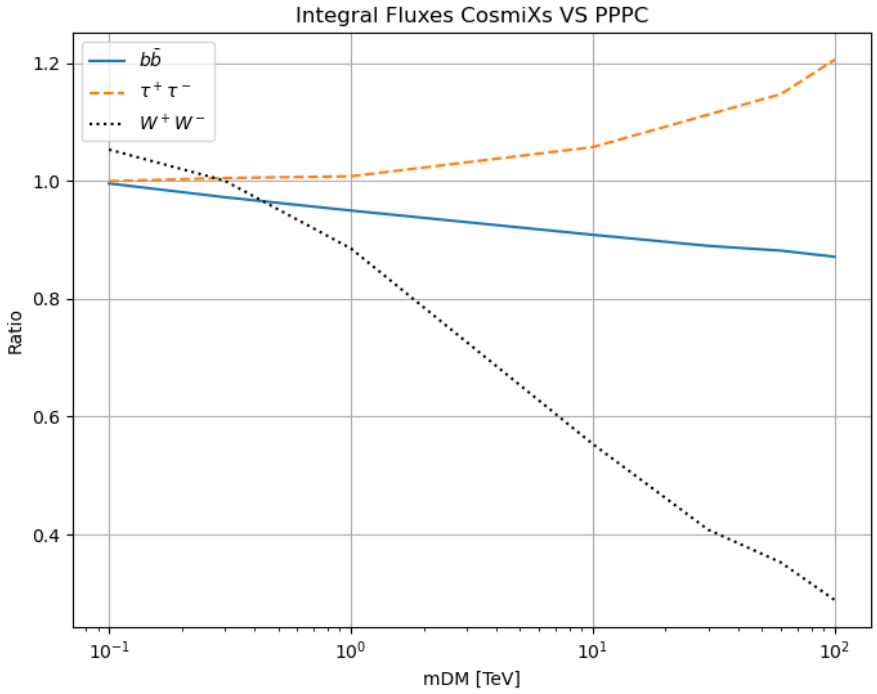

Figure 4.3: Comparison of integral fluxes between CosmiXs and PPPC across different annihilation channels.

Interestingly, for the highest DM mass $\sim m_{\mathrm{DM}} = 100$ TeV, the agreement between the models becomes more pronounced across all channels, suggesting that both models are dominated by similar physical processes, while at lower energies, different assumptions in the modeling lead to noticeable deviations.

4.1.1 Estimation of N_γ

The plot 4.3 shows that the CosmiXs and PPPC predictions are in relatively close agreement for lower m_{DM} ($m_{DM} \leq 10TeV$), particularly in the $b\bar{b}$ and $\tau^+\tau^-$ channels. However, as the mass increases, significant deviations become evident, particularly in the W^+W^- channel, where the ratio shows a marked decline as m_{DM} increases, suggesting that PPPC overestimates the flux at higher DM masses. This effect is less pronounced for the $b\bar{b}$ channel, where the ratio gradually decreases but remains above 0.7, indicating more consistency between the two models in this channel. Interestingly, for the $\tau^+\tau^-$ channel, the ratio exceeds 1 for most m_{DM} values, particularly above 10 TeV, indicating that CosmiXs predicts slightly higher fluxes than PPPC. This happens because CosmiXs incorporates EWBR corrections, that have impact this specific channel more strongly.
For $m_{DM} = 1$ TeV I expected discrepancies to reach 20-30%. In particular, for the W^+W^- channel, the ratio between CosmiXs and PPPC drops to around 0.3 for m_{DM} = 100 TeV. This means that CosmiXs predicts approximately 30% of the flux predicted by PPPC, implying a crucial 70% of difference for this specific case. The $b\bar{b}$ annihilation mode leads to a smaller difference of the predicted flux of about 13%. Finally, for the $\tau^+\tau^-$ channel the ratio at m_{DM} = 100 TeV exceeds 1.2, i.e. CosmiXs predicts

20% more flux than PPPC. For the specific case $m_{\mathrm{DM}} = 1\,\mathrm{TeV}$, the predicted N_γ for $b\bar{b}$ from CosmiXs is approximately 5% lower than PPPC, for $\tau^+\tau^-$ channel it can be demonstrated that CosmiXs' value for N_γ is slightly 1% higher than PPPC; the worst difference is for the W^+W^- channel, being CosmiXs' predictions roughly 15.76% lower than PPPC's predictions, showing an overestimation in the expected flux.

4.2 Intrinsic VS real flux

In this part I outline the results achieved from the subsection 3.4.1: testing the the instrument's sensitivity to specific DM annihilation channels.
The Fig. 4.4 shows the explicit A_{eff} I found in literature. As one can see, all telescopes exhibit their best performance at different energy ranges, suggesting complementary roles in DM studies, where a broad energy spectrum is essential to probe different annihilation channels and spectra. Clearly, a higher effective area means better sensitivity to low fluxes, which is critical for indirect DM detection. Specifically, CTA's coverage surpasses the other telescopes, reflecting its larger array and optimized

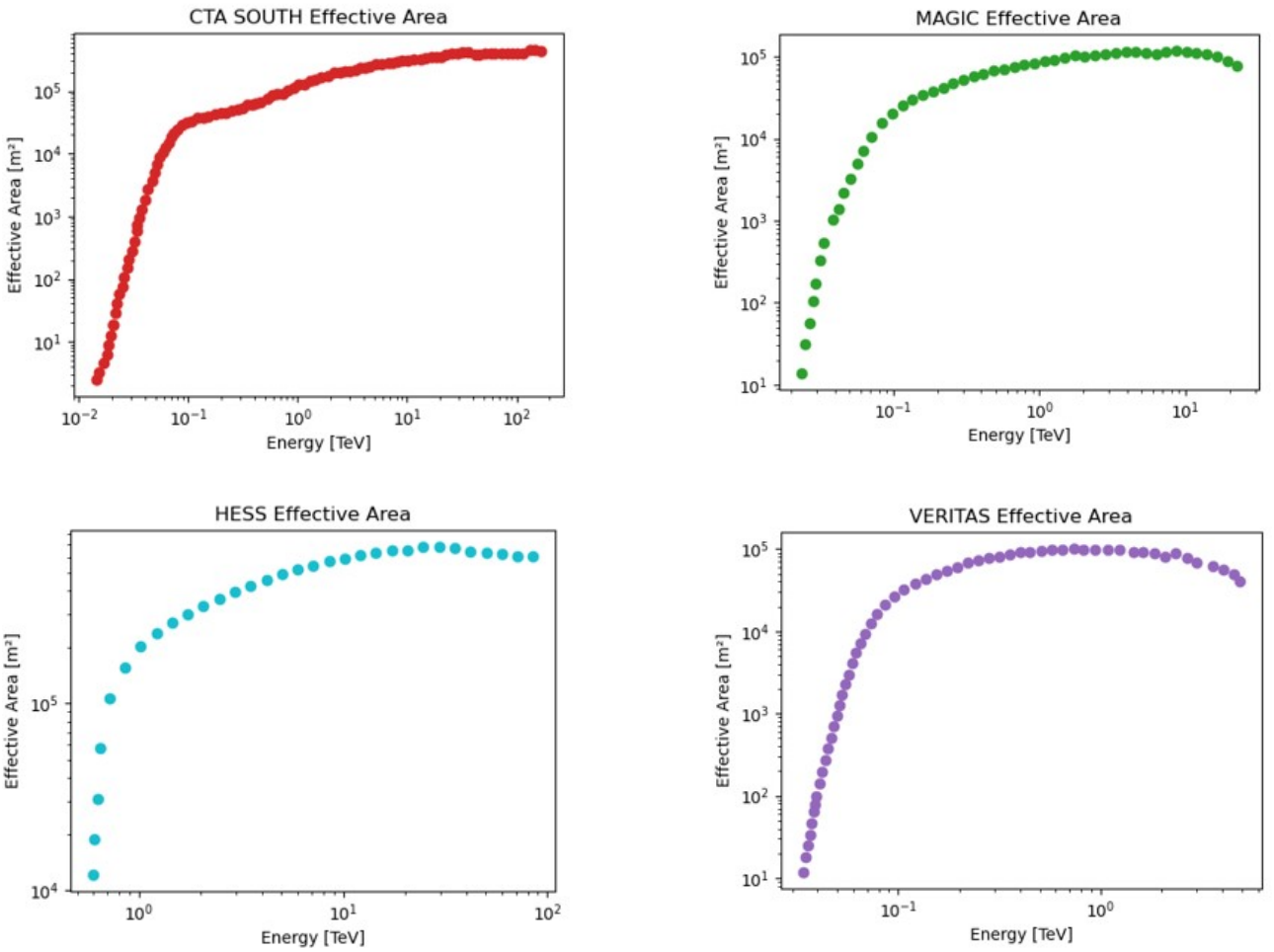

Figure 4.4: The different values of A_{eff} for each telescope. CTA, MAGIC and H.E.S.S. obtained from [49] and Veritas from here.

detection capabilities. Its A_{eff} outperforms others at both low and high energies, indicating its key role in detecting faint signals and extending sensitivity to higher energy ranges. MAGIC shows a

significant rise in its A_{eff} between 100 GeV to 1 TeV, which is typical for its sensitivity in the sub-TeV energy range. H.E.S.S. has a broader coverage in terms of A_{eff} at higher energies, particularly beyond 1 TeV, which aligns with its known sensitivity in the multi-TeV range. VERITAS also shows an increasing trend in effective area with energy, although it peaks at a slightly lower value compared to CTA and H.E.S.S. This is reflected in Fig. 4.5 where a comparison between the intrinsic and the observed (i.e., after taking into account the instrument effective area) flux is shown.

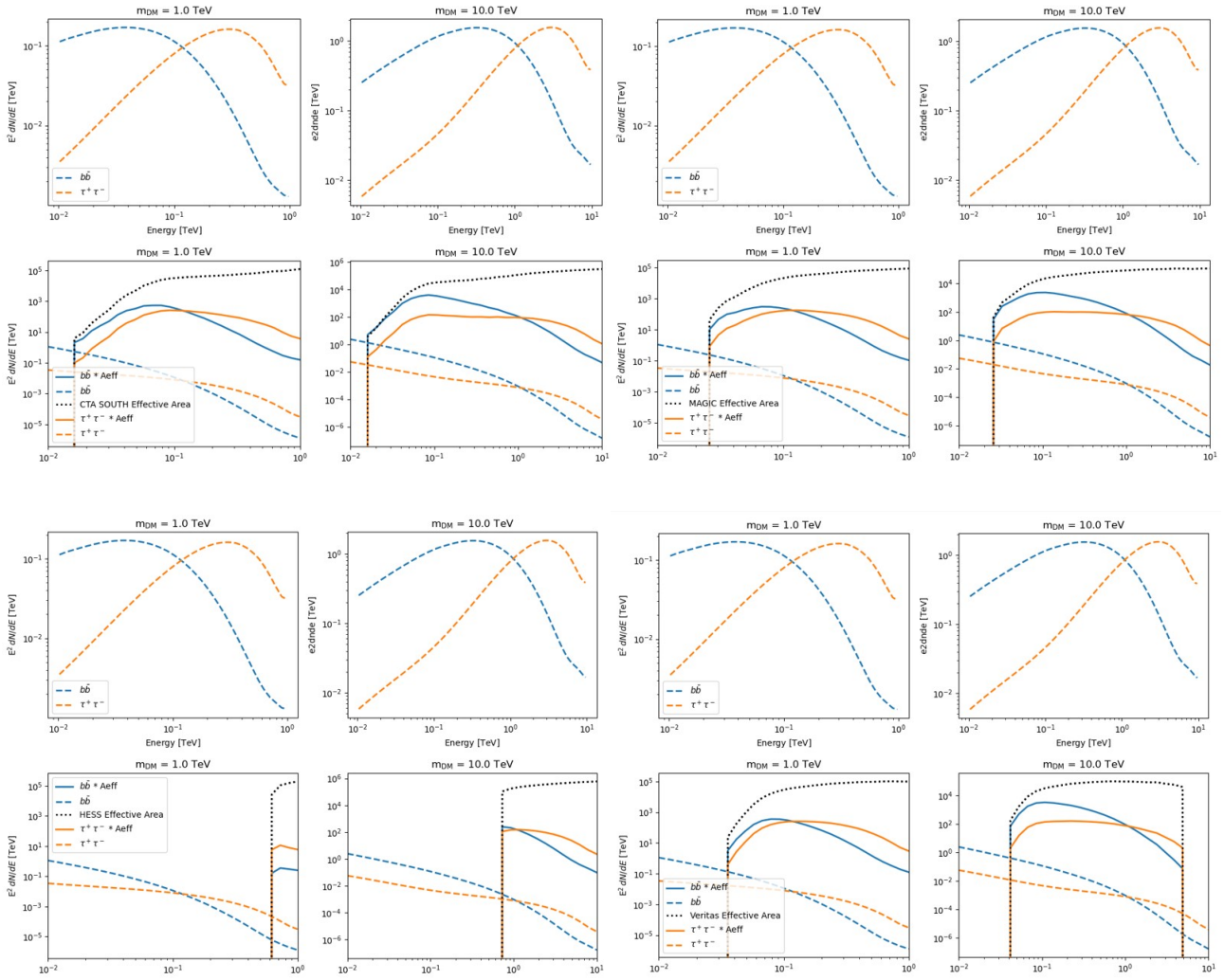

Figure 4.5: Plot of the results for the comparison between intrinsic (**upper row**) and real fluxes (**lower row**). It is reported the specific effective area in dashed black line.

In particular, for the $b\bar{b}$ annihilation channel CTA shows the highest predicted flux across the energy range, thanks to its large A_{eff} and wide energy coverage. This makes it the most sensitive to detecting γ-rays from DM annihilation. MAGIC performs well at lower energies (sub-TeV range), but its sensitivity drops off at higher energies. H.E.S.S. and VERITAS exhibit comparable performance in the mid- to high-energy range (hundreds of GeV to TeV), with H.E.S.S. slightly outperforming VERITAS at the highest energies.

For the $\tau^+\tau^-$ channel, which produces higher-energy γ-rays CTA again provides the highest sensitivity, especially for energies above 1 TeV, indicating its advantage in detecting heavier DM particles. H.E.S.S. and VERITAS both show strong sensitivity in the TeV range, with VERITAS peaking

slightly earlier than H.E.S.S. due to its narrower energy range focus. MAGIC is less sensitive in this channel compared to the others, as its A_{eff} is optimized for lower-energy γ-rays, which are less abundant in this annihilation mode.
These predictions highlight and confirm that CTA is the most versatile telescope for DM searches, while H.E.S.S. and VERITAS excel in detecting high-energy γ-rays, and MAGIC offers unique advantages in the low-energy spectrum.

4.3 Cross Section Ratio and DM Predictions

In this section, I will present the most important results of this thesis work. As outlined in the Methodology chapter, the ultimate goal is to determine whether the simple yet meaningful relation (3.14) holds and, more importantly, if it can effectively *predict* cross-section limits for one DM annihilation channel based on experimental data from another channel. This test was carried out through a series of carefully designed steps, each addressing different aspects of the prediction method. Additionally, I will assess how well the predicted values align with experimental constraints and whether this approach can be generalized to a broader range of channels. Lets now explore these steps in full detail.

4.3.1 $\tau^+\tau^-$ from $b\bar{b}$ for different telescopes

- CTA - Perseus Clustes (2023), [51]:

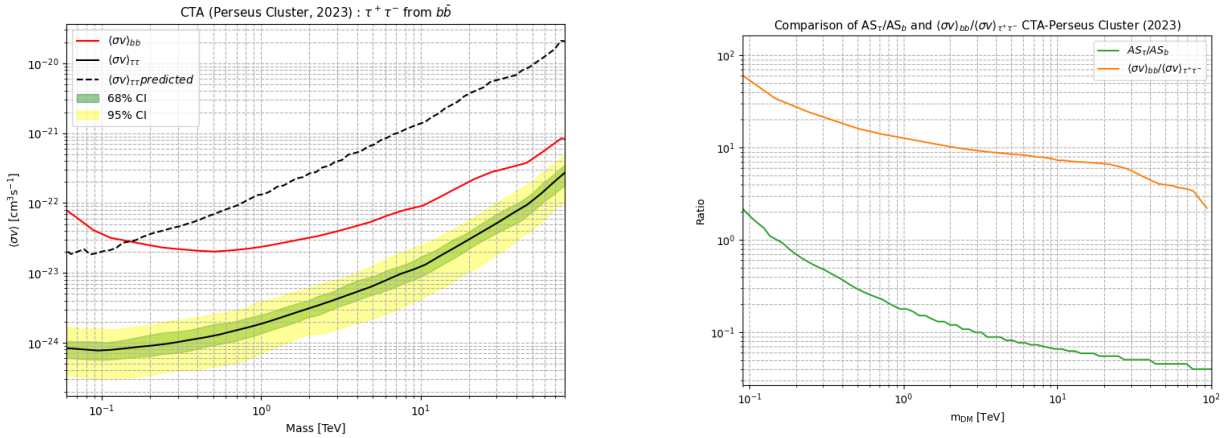

Figure 4.6: Brazilian plot, (**on the left**) with the predicted channel in dashed black line. Such a prediction was done using the $b\bar{b}$ channel, whose upper limits on the cross section are shown in red. **On the right** the comparison between ratios, as highlighted from eq. (3.14). Both plots show the *gap* between the model and the experimental curves, a systematic effect that was found in other analyses too (see next figures) .

- MAGIC - Segue 1 (2022), [52]:

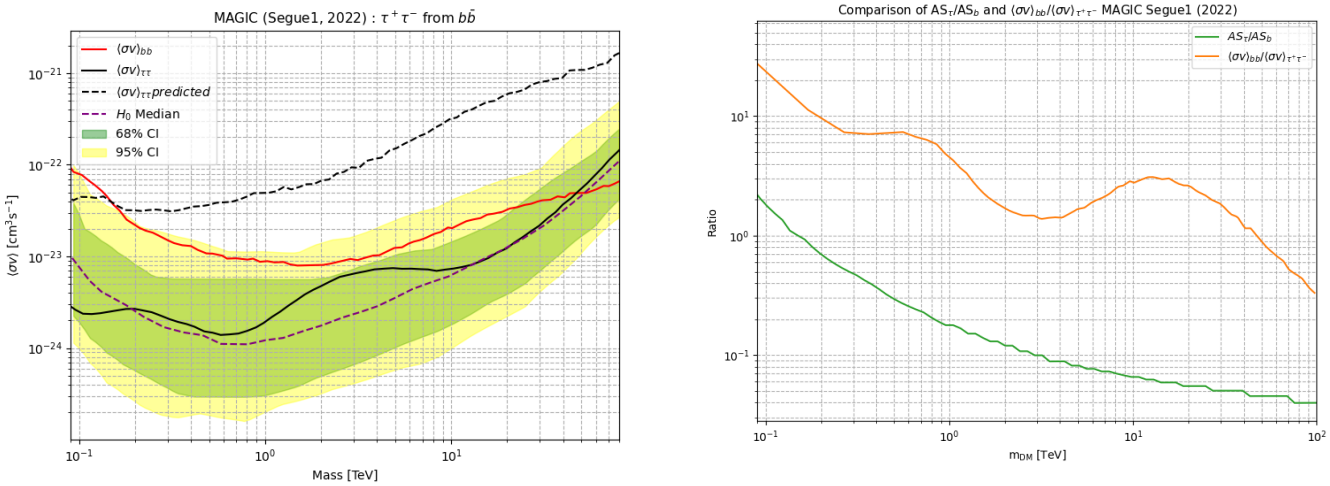

Figure 4.7: Same as for Fig. 4.6, but using the results from MAGIC on Segue 1.

- H.E.S.S - MultidSphs (2020), [53]:

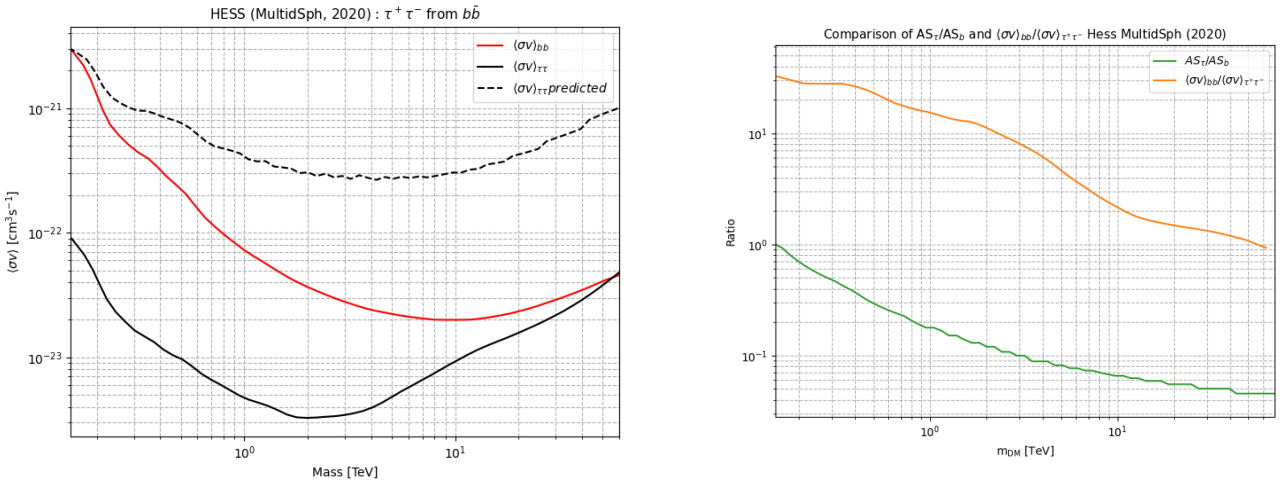

Figure 4.8: Same as for Fig. 4.6, but using the results from HESS on MultidSphs.

- VERITAS - MultidSphs (2017), [54]:

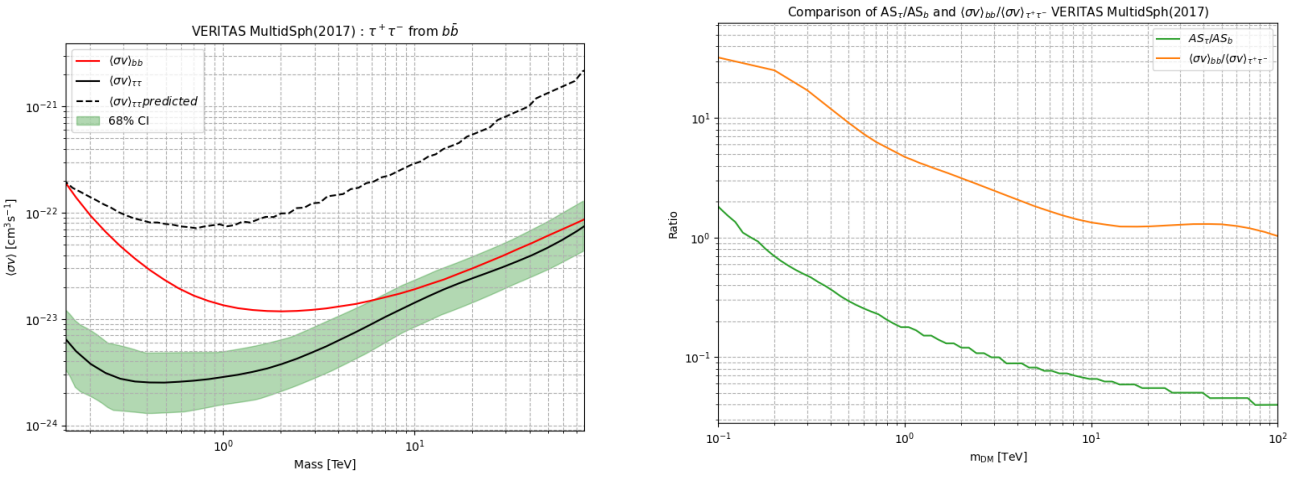

Figure 4.9: Same as for Fig. 4.6, but using the results from VERITAS on MultidSphs.

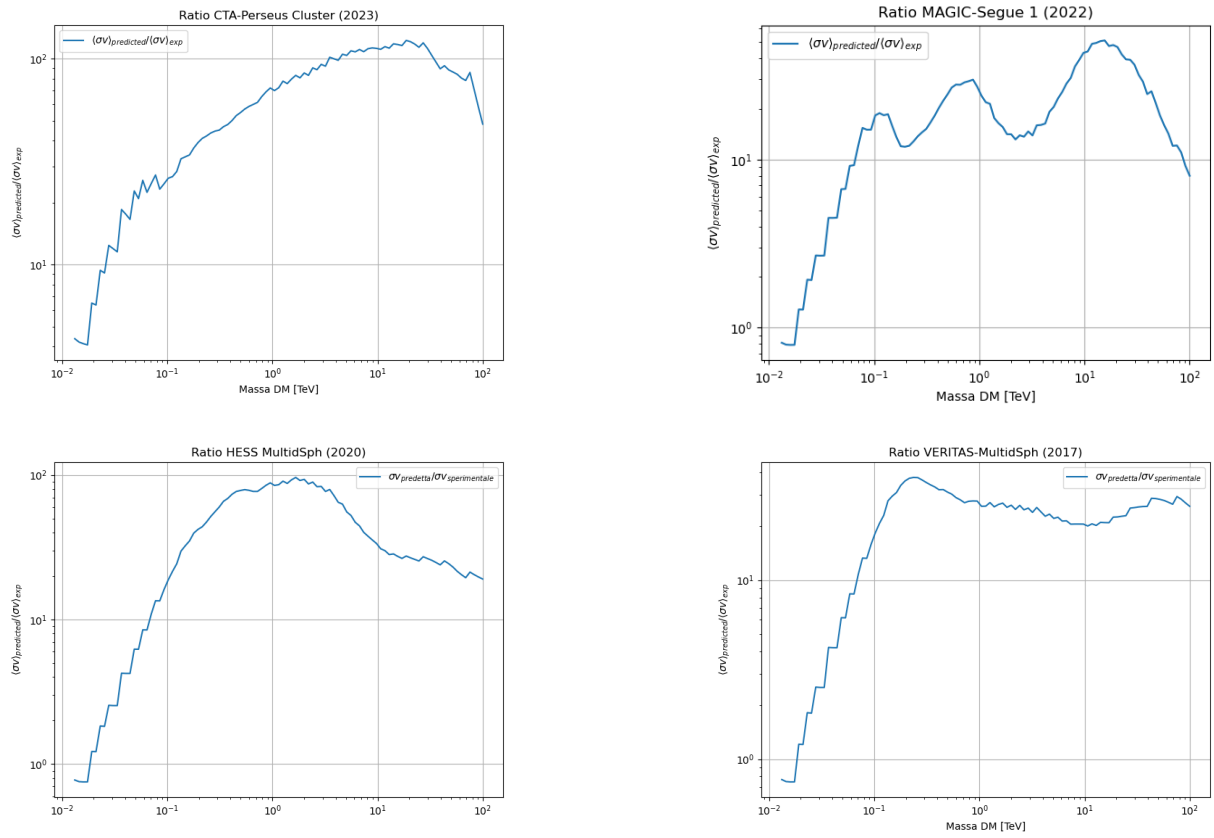

Figure 4.10: Plot in log-log scale of the *gap* between the predicted and the experimental $\tau^+\tau^-$ cross sections for all of the experiments shown in the previous figures.

The general trend of the predicted curve (dashed black) aligns with the experimental results (solid black), confirming the expected behavior. However there is a visible discrepancy, or *gap*, between the two cross sections. This *gap* persists across the mass range showing, in particular, that the model-constructed $\tau^+\tau^-$ DM annihilation mode lies slightly above the experimental bounds, especially at

higher masses. Nonetheless, the overall shape is well captured, supporting the validity of the approach but indicating that refinements are needed to explain the residual discrepancies, which are shown in Fig. 4.10. It is evident that the difference in the curves is more prominent at higher masses in each plots. For instance, in the one from MAGIC, the predicted cross section for $\tau^+\tau^-$ is consistently higher than the experimental bounds for masses greater than 1 TeV, indicating a systematic shift. In the H.E.S.S. plot, the gap is still visible across the mass range, with the predicted values remaining above the experimental ones, suggesting a similar deviation but spread more evenly across the masses. For CTA, from around 10 TeV onwards, the ratio begins to increase significantly, reaching values around 50-100 and higher. Unlike CTA, where the deviation is prominent only at very high masses, the discrepancy in VERITAS appears more gradually, suggesting a progressive misalignment between the model and observations. Additionally, the relatively narrow confidence interval in the VERITAS data highlights how significant this discrepancy becomes, even at intermediate masses.

4.3.2 Various channels for different experiments

In this chapter, I present results of a series of tests conducted to explore the relationships between various DM annihilation channels using data from different observatories. Throughout these tests, it is visible the systematic gap present in previous results. Such a gap is quantified for each curve in Appendix D, in particular the Fig. D.3.

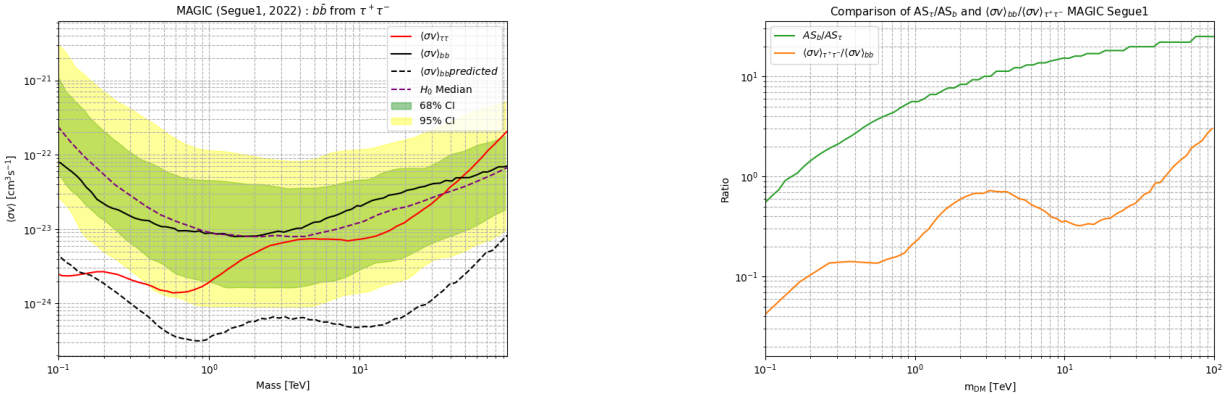

Figure 4.11: MAGIC - Segue 1 ($b\bar{b}$ from $\tau^+\tau^-$).
In the brazilian plot on the left, the predicted $b\bar{b}$ mode (**dashed black line**) is derived from the $\tau^+\tau^-$ channel. One can observe the validity of the applied method, as the general trend of the predicted cross section aligns with the measured one. However, there are some fluctuations, and the usual *gap* effect is noticeable. I suggest taking a quick look at the plot on the right from 4.7, where the inverse correspondence between the orange and green curves is more apparent, with their order now reversed.

Generally speaking, the plots show the same characteristics as the ones discussed in the previous section. Reflecting on the various reasons that may have led to the gap and fluctuations observed in the data, we discovered that one important factor is the effective area I used in the analysis. Specifically, this area does not perfectly correspond to the one specific to each individual observation. This discrepancy arises because telescopes operate under varying conditionssuch as weather, calibration,

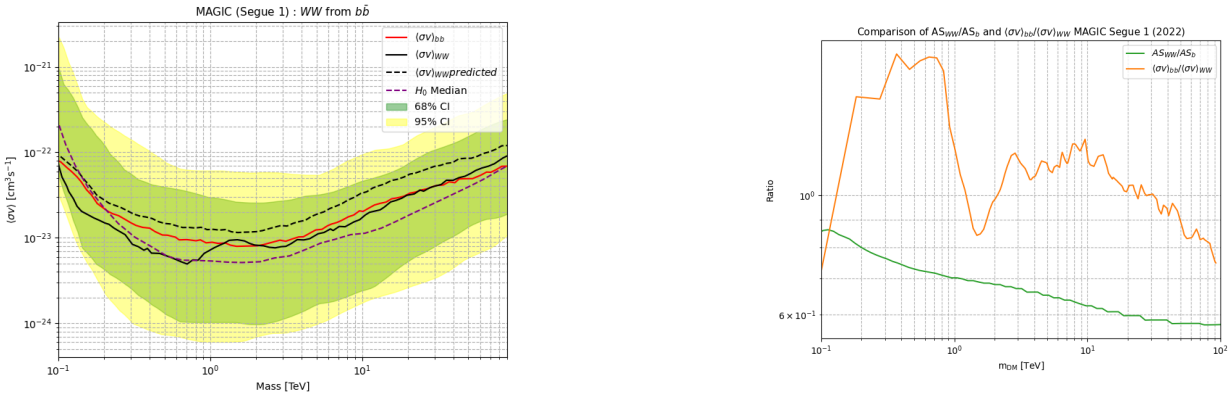

Figure 4.12: MAGIC - Segue 1 (W^+W^- from $b\bar{b}$).
The predicted W^+W^- cross section (**dashed black line**) aligns well with the experimental curve, perfectly falling within the CL regions. This brazilian plot represents one of the most accurate results obtained. In contrast, the right plot reveals the highly fluctuating **orange** ratio.

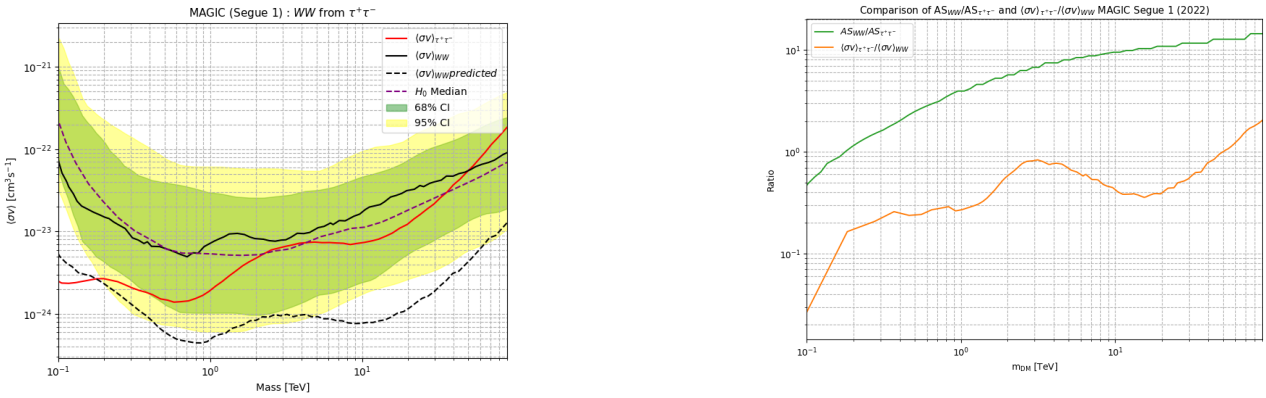

Figure 4.13: MAGIC - Segue 1 (W^+W^- from $\tau^+\tau^-$).
The predicted curve for the W^+W^- confirms the trend of the median H_0 (**magenta dashed line**) of the experimental signal as it lies within the 68% CL, indicating a reliable prediction. On the right, the usual gap is observed.

and atmospheric effects which inevitably influence the results. Moreover, through further investigation, we found that it is possible to interpolate the effective area used to derive the experimental cross-section. This can be achieved by leveraging the ratio between the cross-sections and tuning some parameters, allowing us to establish a more accurate comparison.

Another reason for the differences is that I am assuming a single energy bin for comupting the upper limit on the cross-section. This assumption works under certain conditions, but the upper limit on cross-sections (shown by the solid black and solid red lines) obtained from literature is actually calculated using multiple energy bins to improve accuracy. As a result, I am comparing an upper limit computed from several energy bins with one derived from a method that works under the assumption of one single bin. This is what causes the orange curve on the left-hand plot to fluctuate. In an attempt to mitigate these fluctuations, I explored applying an energy smearing. This technique was meant to account for the spread of energy within each bin, but in practice, it did not produce any significant

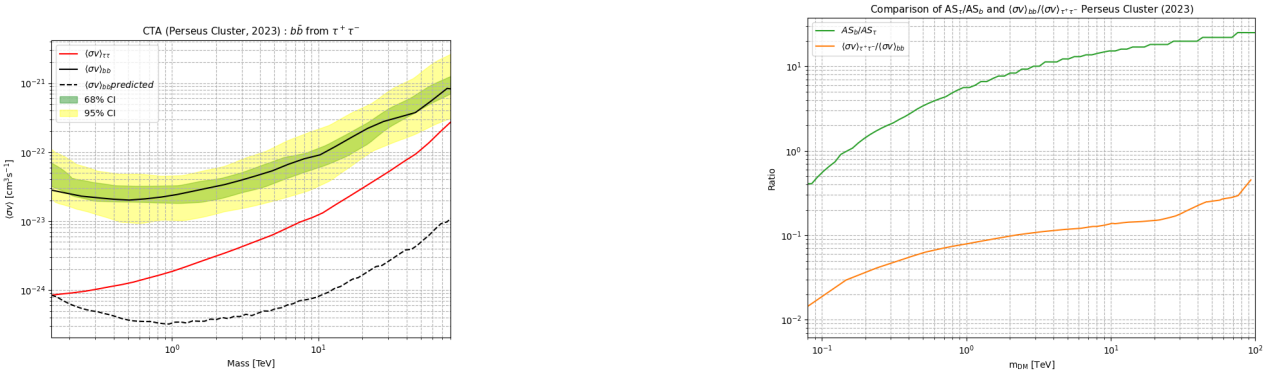

Figure 4.14: CTA - Perseus Cluster ($b\bar{b}$ from $\tau^+\tau^-$).
This brazilian plot shows the worst difference between the cross sections, here depicted in **dashed black**: the *gap* effect is more pronounced although the trend between the two curves is perfectly equal. On the right, one can appreciate the inverse correspondence in contrast to the previous test in the plot 4.6.

improvement, leaving the systematic error largely unaffected.

Chapter 5
CONCLUSION AND FUTURE WORKS

In this thesis I focused on advancing the `gDMbounds` project, a platform aimed at collecting specific limit on DM annihilation and decay. My work centered on refining the predictive tools used in DM research, comparing theoretical models, and enhancing the methodologies for analyzing observational data.

Particularly through the comparative analysis between the *CosmiXs* and *PPPC* models, I highlighted similarities in their generated spectra for DM masses below 10 TeV. However, they present significant differences at higher masses especially in the W^+W^- channel, where the CosmiXs predictions are around 70% lower than those of PPPC for $m_{DM} = 100$ TeV. For the $b\bar{b}$ channel, the discrepancy is about 13%, while for the $\tau^+\tau^-$ DM annihilation mode, CosmiXs predicts 20% more flux than PPPC. These differences likely stem from the improved treatment of QCD showers in CosmiXs, especially thanks to the integration of the Vincia algorithm. The ability to manage QCD effects more effectively allows CosmiXs to provide a more accurate representation of the energy distribution in such annihilation channels, making it a crucial tool for better understanding DM phenomenology, especially at higher masses. This advanced handling of parton showers is particularly advantageous for studying DM candidates like the Higgsino, which predominantly annihilates into W^+W^- pairs.

In the second part of the analysis, I presented several statistical tools from γ-ray astronomy to better understand the working principles of IACTs. The primary objective of this section was to investigate how the effective area would modify the *intrinsic* flux expected from MC simulations, such as those provided by CosmiXs and PPPC. The results demonstrated that the CTA, H.E.S.S., VERITAS, and MAGIC telescopes exhibit different capabilities in terms of sensitivity and energy coverage. The plots confirmed that CTA is the most versatile instrument for DM searches, given its broad energy range and superior sensitivity across multiple mass scales. On the other hand, H.E.S.S. and VERITAS were shown to excel in the detection of high-energy γ-rays, particularly suited for DM scenarios involving heavy particles. MAGIC, with its strong performance at lower energies, proves especially advantageous for probing DM candidates with lower masses or annihilation channels that favor softer energy spectra. These complementary strengths make each telescope essential for a comprehensive study of DM across different mass ranges and annihilation channels.

Finally, the main important part of this analysis was driven together with G. D'Amico and M. Doro. Starting from the simple one-bin energy relation:

$$\frac{\langle \sigma v \rangle_i^{UL}}{\langle \sigma v \rangle_j^{UL}} = \frac{A_j}{A_i}, \tag{5.1}$$

our first ambitious goal was to understand if we would be able to predict other annihilation channels based on existing data cross sections. This way of proceeding could be extremely useful to put con-

straints on DM models, helping adjust the branching ratios based on experimental limits and ensuring that predicted cross sections align with experimental constraints for different channels; moreover, it could be important to test mixed-channel hypotheses, i.e. to verify if the predicted mix of annihilation into different channels (e.g., leptonic vs hadronic) is consistent with observational ULs.

I stress the fact that these curves were generated using a simple interpolation based on cross-section ratios and effective areas extracted from literature studies. The fact that the curves are so similar, despite differences in instruments and observation periods, suggests that the interpolation method works with reasonable accuracy, within a factor of 10-100. This result confirms that the predicted flux for one channel can be estimated from another channel with a good degree of precision, making this method useful for future predictions or comparative analysis.

However, the study revealed some systematic errors (*gap effect*, fluctuations) between theoretical predictions and experimental data, partly due to the use of an interpolated effective area that does not exactly reflect the observational conditions of each individual telescope. Another source of fluctuations in the analysis arises from the decision to utilize a single energy bin. While this approach simplifies the analysis, it imposes limitations when comparing the results to experimental data. The experimental cross-sections, represented by the solid black and red lines, are calculated using multiple energy bins, enhancing their accuracy and reliability. Consequently, the $\frac{A_j}{A_i}$ curve in the plot exhibits more erratic behavior, reflecting the variability introduced by the single-bin approach.

Hence, we suggest that telescopes publish the number of excess counts $N_{\mathrm{EXC}}^{\gamma,UL}[E_0, m_\chi]$ from their experiments, as this would be particularly beneficial for the goal of predicting the DM annihilation cross-section signal using the formula (5.1). It would allow in managing statistical fluctuations and refining annihilation models, facilitating a deeper understanding of the underlying physical processes.

This work presents significant findings that contribute to our understanding of DM annihilation processes and their implications for current observational data. Given the relevance of these results and their potential impact on the field, we believe that this research could be published in a journal, providing an opportunity for further discussion and exploration among the scientific community.

Appendix A
The Collisional Boltzmann Equation (CBE)

The Boltzmann equation[1] describes the evolution of the distribution function $f(x,p,t)$ of a particle species in phase space (which includes both position and momentum). The equation is crucial in statistical mechanics and cosmology, particularly for understanding how particles interact and evolve in the early Universe. Hence to characterize a relic density in a precise way, calculations must be based on the solution of the Boltzmann equation, which can be written in the following schematic way:

$$\hat{L}[f] = \hat{C}[f], \tag{A.1}$$

where:

- $C[f]$ is the collision operator, taking care of the interactions between DM and other particles (including itself) and can take a complicated form;
- $\hat{L}[f]$ is the Liouville operator, given by:

$$\hat{L}_{\rm NR} = \frac{d}{dt} + \frac{dx}{dt}\cdot\nabla_x + \frac{dv}{dt}\cdot\nabla_v, \tag{A.2}$$

$$\hat{L}_{\rm cov} = p_\alpha \frac{\partial}{\partial x^\alpha} - \Gamma^\alpha_{\beta\gamma} p^\beta p^\gamma \frac{\partial}{\partial p_\alpha}, \tag{A.3}$$

the first form A.2 is written in a non-relativistic limit, while the A.3 is the covariant realization of the operator.

To model the MW DM halo today, we can notice that it appears non-relativistic and collisionless. In this case the probability density depends only on energy and time and the covariant form of Liouville operator A.3 will become:

$$\hat{L}[f] = E\frac{\partial f}{\partial t} - H|p|^2\frac{\partial f}{\partial E}. \tag{A.4}$$

Using the definition of the number density of a given species (from thermodynamics), defined as the the integral over the proper momentum volume:

$$n(t) = g\int \frac{d^3p}{(2\pi)^3} f(E,t),^2 \tag{A.5}$$

in the expression A.4, we can obtain the left-hand side of the Boltzmann equation 1.19:

[1] The references for this argument are [15] and [17].

[2] g is the number of spin (or helicities, for a massless species) states.

$$g\int \frac{d^3p}{(2\pi)^3}\hat{L}[f] = \frac{dn}{dt} + 3Hn. \tag{A.6}$$

where $H = \dot{a}/a$ is the expansion rate of the Universe and a is the scale factor. We will evaluate the evolution of the DM number density considering interactions of the form $1+2 \leftrightarrow 3+4$. The collision term for particle 1 is:

$$g_1 \int \frac{d^3p_1}{(2\pi)^3}\hat{C}[f_1] = -\sum_{\text{spins}} \int \left[f_1 f_2 (1 \pm f_3)(1 \pm f_4)|M_{12\to 34}|^2 - f_3 f_4 (1 \pm f_1)(1 \pm f_2)|M_{34\to 12}|^2\right] \times (2\pi)^4 \delta^4(p_1 + p_2 - p_3 - p_4)\, d\Pi_1\, d\Pi_2\, d\Pi_3\, d\Pi_4 \tag{A.7}$$

where g_i and f_i are the spin degrees of freedom and phase-space densities, respectively, for particle i, and $M_{x\to y}$ is the matrix element for the reaction $x \to y$. Factors of the form $(1 \pm f)$ represent Pauli blocking and Bose enhancement; the minus sign applies to fermions and the plus sign to bosons. The delta function enforces energy and momentum conservation, and the phase-space integration factors are given by:

$$d\Pi_i = \frac{d^3p_i}{(2\pi)^3 2E_i}. \tag{A.8}$$

To simplify the (A.7) let's make the following assumptions:

1. Kinetic equilibrium is maintained, and so the phase-space distributions take on the Fermi-Dirac or Bose-Einstein forms.

2. The temperature of each species satisfies $T_i \ll E_i - \mu_i$, where μ_i is its chemical potential, so that they follow the Maxwell-Boltzmann distribution. In this case, the statistical mechanical factors in the calculation can be ignored and $(1 \pm f) \sim 1$.

3. The SM particles in the interaction are in thermal equilibrium with the photon bath.

Using the standard definition relating the cross-section to the matrix element, we get:

$$\sum_{\text{spins}} \int |M_{ij\to kl}|^2 \times (2\pi)^4 \delta^4(p_i + p_j - p_k - p_l)\, d\Pi_k\, d\Pi_l = 4 g_i g_j \sigma_{ij} v_{\text{Møller}} \left(\frac{p_i \cdot p_j}{2} - (m_i m_j)^2\right), \tag{A.9}$$

where σ_{ij} is the cross-section for the scattering process. Substituting this back into the collision term gives:

$$g_1 \int \frac{d^3p_1}{(2\pi)^3}\hat{C}[f_1] = -\int \left[(\sigma v_{\text{Møller}})_{12}\, n_1 n_2 - (\sigma v_{\text{Møller}})_{34}\, n_3 n_4\right], \tag{A.10}$$

and the Møller velocity is defined as:

$$(v_{\text{Møller}})_{ij} = \frac{\sqrt{(p_i \cdot p_j)^2 - (m_i m_j)^2}}{E_i E_j} \tag{A.11}$$

for the $ij \to kl$ process. Because $\sigma v_{\text{Møller}}$ varies slowly with changes in the number density of the initial and final-state particles, it can be factored out of the integrand to give:

$$\dot{n}_1 + 3Hn_1 = -\langle \sigma v_{\text{Møller}} \rangle_{12} n_1 n_2 + \langle \sigma v_{\text{Møller}} \rangle_{34} n_3 n_4. \tag{A.12}$$

If the particle 1 and 2 are the same, i.e. the interaction under investigation is an annihilation process and furthermore have identical with number density n, and particles 3 and 4 are SM particles in thermal equilibrium with the photon bath, we have:

$$\langle \sigma v \rangle_{12} n_{\text{eq}}^2 = \langle \sigma v \rangle_{34} n_{\text{eq}}^3 n_{\text{eq}}^4, \tag{A.13}$$

which can be used to rewrite the second term of (A.12) in terms of the DM number density and the cross-section for the forward reaction. The Boltzmann equation reduces to:

$$\dot{n} + 3Hn = \langle \sigma v \rangle (n_{eq}^2 - n^2). \tag{A.14}$$

This equation must be solved numerically. Typically one expands $\langle \sigma v \rangle$ in powers of the relative velocity v assuming a constant $\langle \sigma v \rangle$ and it is usually called the s-wave approximation.

Appendix B
Development of atmospheric showers

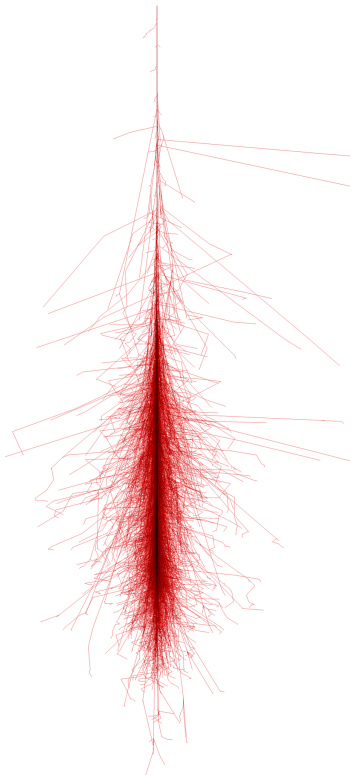

(a) Simulated electromagnetic shower produced by a primary particle with 100 GeV energy. This process appears narrow and at lowest approximation axially symmetric along the direction of the primary gamma rays.

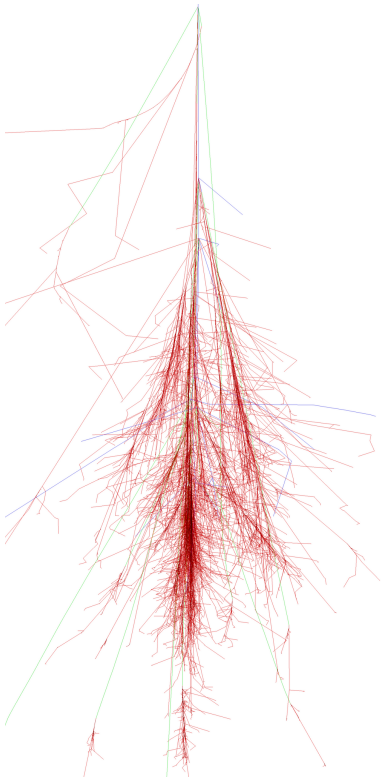

(b) Simulated hadronic shower produced by a primary particle with 100 GeV energy. The cascade appears irregular and might contain EM subshowers.

Figure B.1: Side view simulation of atmospheric showers driven with `CORSIKA` [55]. The red lines show the tracks produced by electrons, positrons and gammas while the green and the blue show the tracks produced by muon and hadrons respectively.

Cosmic ray particles impinging on Earths atmosphere, starting from energies of the order of ~ 1 GeV, trigger a whole cascade of secondary particles after their first interaction with air-molecules and atoms. The type of the primary particle has large influence on the development of such Extended Air-Showers (EAS), i.e. swarms of secondary particles keeping the identity of the primary cascade. In particular, if the shower is generated by a γ-ray, it is called an electromagnetic cascade, while if it is produced by a hadron, it is called a hadronic cascade. In details:

- **Electromagnetic shower**: they are initiated when a high-energy γ-ray interacts with the electric field of atmospheric atoms and molecules, primarily through the process of pair production ($\gamma \to e^+e^-$). The threshold energy for this process is $E_{\text{th}} \approx 1$ MeV, which makes it relevant

for very high-energy VHE γ-rays. The resulting electron and positron then radiate additional photons via bremsstrahlung ($e^{\pm} \rightarrow e^{\pm}\gamma$), leading to a cascading effect characterized by the continuous production of particles through these two reactions. During the shower development, the number of particles increases while their individual energies decrease. The shower reaches its maximum when the average particle energy equals the critical energy $E_c \approx 84$ MeV in air. At this point, energy losses due to ionization become dominant, leading to a gradual decline in the number of particles as the shower dissipates due to atmospheric absorption.

The longitudinal development of electromagnetic cascades can be described using a simple model first proposed by Heitler (1954)[56]. The primary assumption is that after one radiation length X_0, a gamma-ray creates an $e^+ + e^-$ pair, and the e^+ or e^- emits a bremsstrahlung photon. The energy of a particle (whether e^+, e^-, or γ) is equally distributed between the two outgoing particles ($e^+ + \gamma$, $e^- + \gamma$, or $e^+ + e^-$). This process continues until the energy of the particles drops to a critical value where ionization losses of the electrons become comparable to the radiation losses ($E_{e^-} = \mathcal{O}(100\,\text{MeV})$). At this stage, the shower starts to die out. A more detailed description of this phenomenon was given by Rossi and Greisen [57]. For γ-rays with energies between 20 GeV and 20 TeV, the shower maximum occurs at depths of 250 to 450 g/cm^2, corresponding to an atmospheric height of 7 to 12 km above sea level. Showers from γ-rays with energies below 200 GeV may dissipate before reaching ground-based telescopes like MAGIC, which are situated at around 2200 m above sea level. A schematic view could be given by the figure B.1a.

- **Hadronic shower**: they result from the interaction of protons, helium constituting cosmic rays with the atmospheric nuclei via strong interactions. The interaction produces secondary particles, mainly pions ($\sim 89\%$) and kaons ($\sim 10\%$). They exhibit broader lateral spreads and greater asymmetry compared to EM showers due to the variety of secondary particles and subshowers involved, as it can be seen in the figure B.1b.

  Hadronic showers are characterized by three key components:

  - A hadronic core composed of secondary nucleons and charged pions, which perpetuate nuclear collisions until the energy drops below the pion production threshold (~ 1 GeV).
  - A muonic component formed from pion and kaon decays:

    $$\pi^{\pm} \rightarrow \mu^{\pm} + \nu_{\mu}(\bar{\nu}_{\mu})$$

    High-energy muons can reach the Earth's surface with minimal energy loss, distinguishing hadronic showers from electromagnetic showers.
  - An electromagnetic component resulting from neutral pion decays ($\pi^0 \rightarrow \gamma + \gamma$) leading to secondary electromagnetic showers. About one-third of the energy is channeled into this component.

Appendix C
Feynman diagrams

In this part I report the Feynman diagrams related to the different processes which produce cosmic messengers. In particular, as previously explained in the section 2.3, when a DM particle (χ) annihilate or decay quarks and gluons can be produced. These are high-energy partons that subsequently generate a shower of particles, through a continuous gluon emission and quark-antiquark pair production. It stops when the particles'energy is low enough to start the hadronization. The hadronization (which happens at about $10^{-15}m$ timescale) is the process in which showers' particles collide into mesons (π^0, $\pi^{\pm}$) and baryons. Afterwards, because of their unstability, mesons decay into γ-rays, ν, e^+ or e^-: our cosmic rays. Other relevant processes, in addition to the hadronization, are electronweak decays (EWBR), which account for decays involving weak interactions (as the decay of τ and μ leptons or gauge bosons, W and Z). They are mainly responsible for the generation of $e^{\pm}$ cosmic messengers. Diagrams C.7 and C.8 are the colored particles produced through QCD internal bremsstrahlung.

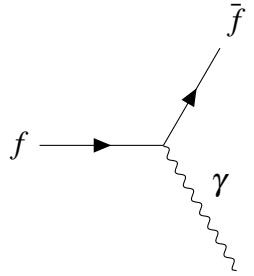

Figure C.1: QED emissions of gauge boson off fermion lines γ.

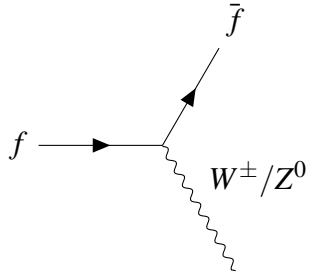

Figure C.2: EW emissions of gauge bosons off fermion lines $W^{\pm}/Z^0$.

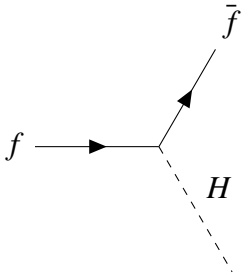

Figure C.3: Higgs emission off fermion lines.

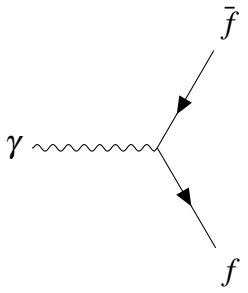

Figure C.4: Photon splitting into $f\bar{f}$.

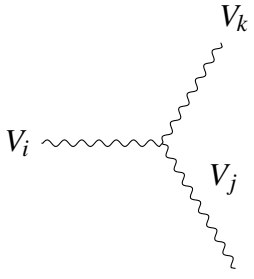

Figure C.5: Gauge bosons emission off bosonic lines (EWBR).

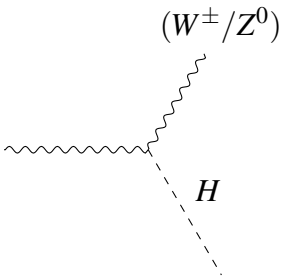

Figure C.6: Higgs emission off bosonic lines (EWBR).

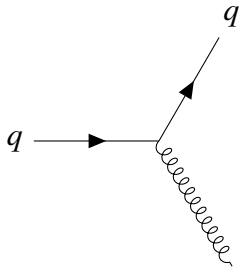

Figure C.7: Gluon emission from quark lines.

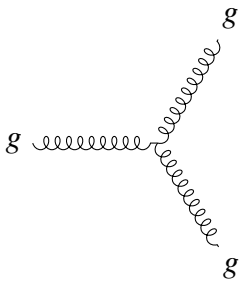

Figure C.8: Gluon splitting into gg.

Appendix D
Backup plots

Other tests

In this part one can find two other tests, to explore the possibility to predict other channels as well as to use other sources.

- MAGIC - Segue 1 ($\tau^+\tau^-$ from $\mu^+\mu^-$), [52]:

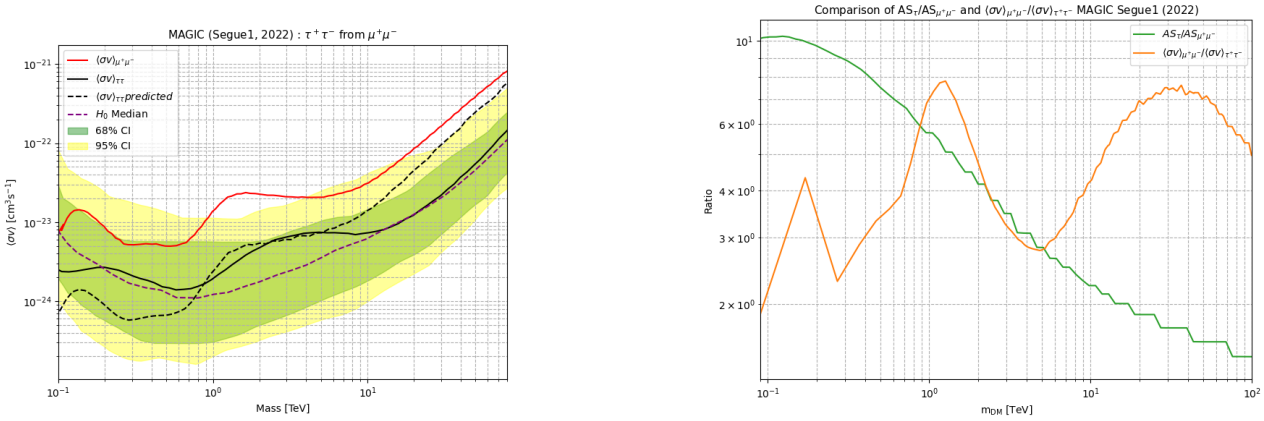

Figure D.1: In the brazilian plot you one can observe a better agreement between both of the predicted and experimental curves. It might be explained by the fact that both $\tau^+\tau^-$ and $\mu^+\mu^-$ are leptonic channels. Except for the lower energies ($\leq 10^0$ TeV) side of the graph, one can notice the agreement with the median curve (**dashed magenta line**). One the right there is the usual

- H.E.S.S. - GC (W^+W^- from $b\bar{b}$), [53]:

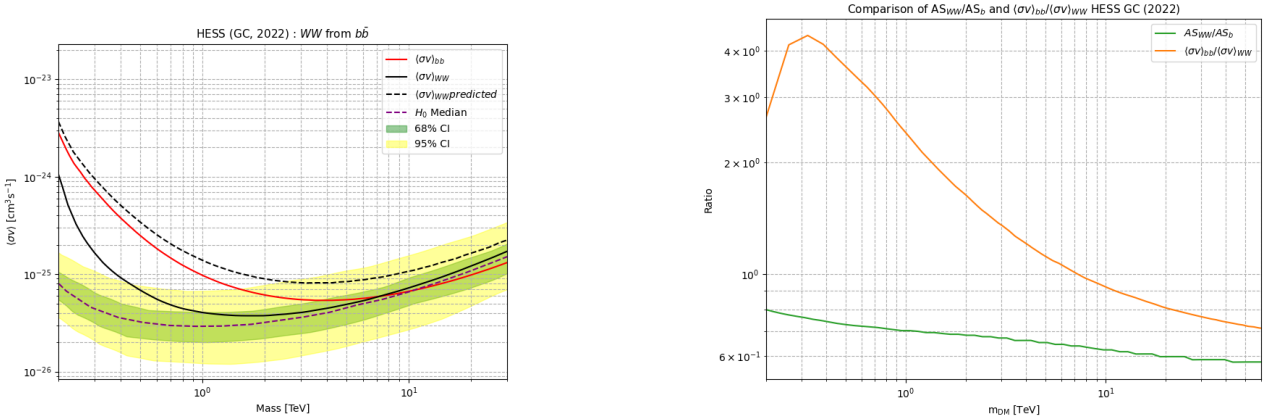

Figure D.2: One can see a good agreement between the two $W+W^-$ cross sections, especially from $\sim 2\times 10^0$ TeV, being the precticted one fully included in the CL bands. The trend entirely recontruct the median curve. The next plot shows few difference between the two ratios, however the systematic error is still present.

Quatify gaps

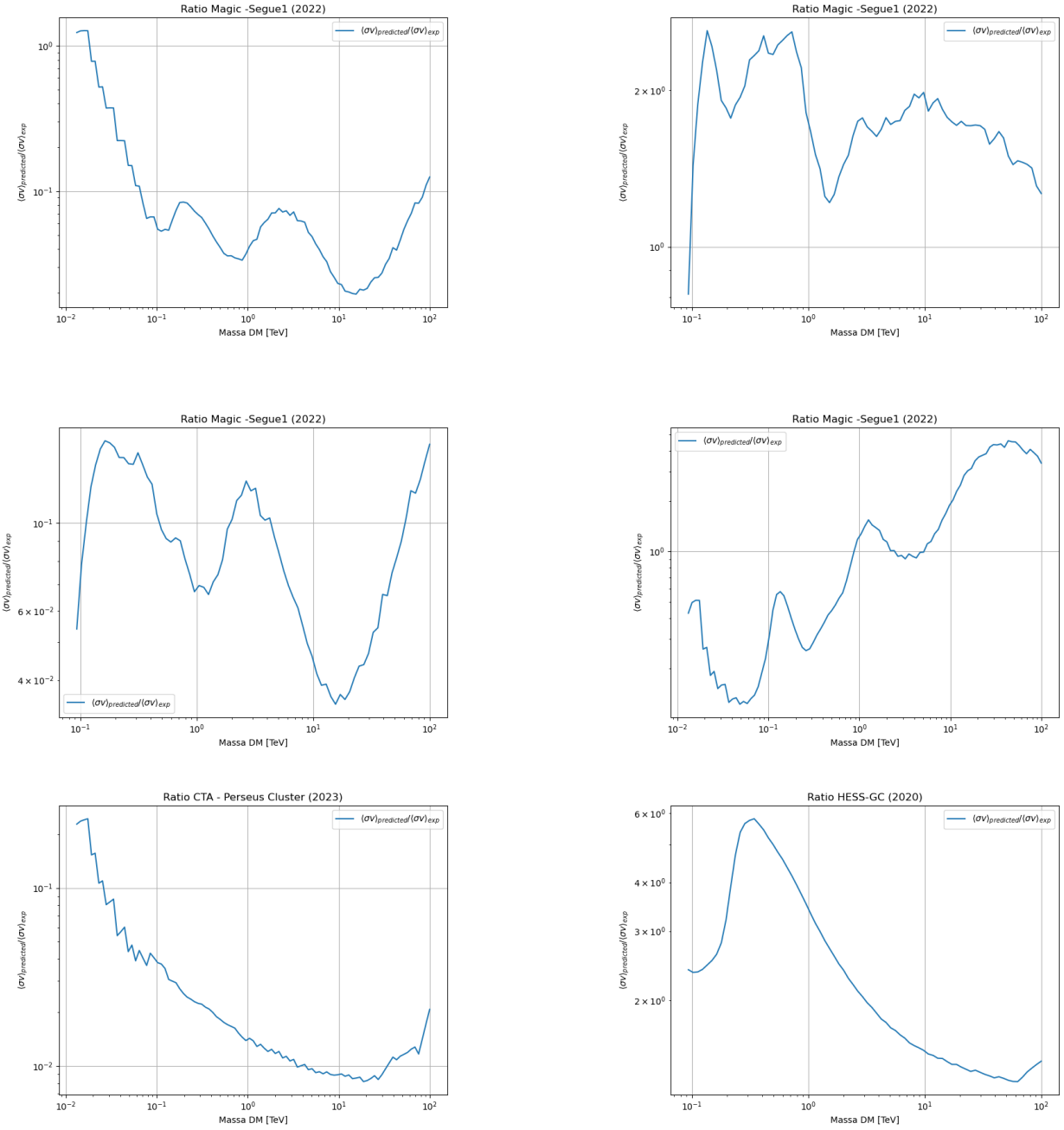

Figure D.3: log-log plot of the gap between the predicted cross sections.

REFERENCES

[1] A. et. al, "Planck 2018 results. vi. cosmological parameters," 2020. DOI: 10.1051/0004-6361/201833910. [Online]. Available: https://doi.org/10.1051/0004-6361/201833910.

[2] F. Zwicky, "Die rotverschiebung von extragalaktischen nebeln," *Helv.Phys.Acta 6*, vol. 6, pp. 110–127, 1933. DOI: 10.1007/s10714-008-0707-4.

[3] V. C. R. W. F. Jr, "Rotation of the andromeda nebula from a spectroscopic survey of emission regions," *Astrophys. J.*, vol. 159, pp. 379–403, Feb. 1970. DOI: 10.1086/150317.

[4] A. Bosma, "21-cm line studies of spiral galaxies. II. The distribution and kinematics of neutral hydrogen in spiral galaxies of various morphological types.," *Astronomy Journal*, vol. 86, pp. 1825–1846, Dec. 1981. DOI: 10.1086/113063. [Online]. Available: https://ui.adsabs.harvard.edu/abs/1981AJ.....86.1825B.

[5] J. B. Tyldesley, "Gilbert White and the aurora.," *Journal of the British Astronomical Association*, vol. 86, pp. 214–218, Apr. 1976.

[6] S. M. Kent and J. E. Gunn, "The dynamics of rich clusters of galaxies. I. The Coma cluster.,", vol. 87, pp. 945–960, Jul. 1982. DOI: 10.1086/113178.

[7] S. M. Kent and W. L. W. Sargent, "The dynamics of rich clusters of galaxies. II. The Perseus cluster.,", vol. 88, pp. 697–708, Jun. 1983. DOI: 10.1086/113362.

[8] G. Bertone and D. Hooper, "A history of dark matter," *Rev. Mod. Phys.*, vol. 90, 4 Jul. 2016. DOI: 10.1103/RevModPhys.90.045002. [Online]. Available: https://doi.org/10.1103/RevModPhys.90.045002.

[9] N. Vera C. Rubin; W.Kent Ford Jr; Thonnard, "Rotational properties of 21 sc galaxies with a large range of luminosities and radii, from ngc 4605 (r=4kpc) to ugc 2885 (r=122kpc)," *Astrophys. J.*., vol. 238, p. 471, Jun. 1980. DOI: 10.1086/158003.

[10] J. van Albada T.S.; Bahcall and e. a. Begeman, "Distribution of dark matter in the spiral galaxy ngc 3198," *The Astrophysical Journal*, vol. 295, pp. 305–313, Aug. 1985. DOI: 10.1086/163375. [Online]. Available: https://ui.adsabs.harvard.edu/abs/1985ApJ...295..305V.

[11] B. Fuchs, "Dynamics of the disks of nearby galaxies," *Astronomische Nachrichten*, vol. 329, pp. 916–921, 2008. [Online]. Available: https://api.semanticscholar.org/CorpusID:17196648.

[12] D. e. a. Clowe, "A direct empirical proof of the existence of dark matter," *Astroph. J.*, vol. 648, pp. 109–113, 2 II Sep. 2006. DOI: 10.1086/508162. [Online]. Available: https://doi.org/10.1086/508162.

[13] D. Fixsen, "The temperature of the cosmic microwave background," *Astrophys. J.*, vol. 707, pp. 916–920, 2009. [Online]. Available: https://doi.org/10.48550/arXiv.0911.1955.

[14] F. e. a. Acero, *Gammapy: Python toolbox for gamma-ray astronomy*, version v1.2, Feb. 2024. DOI: 10.5281/zenodo.10726484. [Online]. Available: https://doi.org/10.5281/zenodo.10726484.

[15] M. Lisanti, "Lectures on dark matter physics," *TASI Lecture Notes*, Mar. 2016. DOI: 10.48550/arXiv.1603.03797. [Online]. Available: https://doi.org/10.48550/arXiv.1603.03797.

[16] S. Tremaine and J. E. Gunn, "Dynamical role of light neutral leptons in cosmology," *Physical Review Letters*, pp. 407–410, 6 Feb. 1979. DOI: 10.1103/physrevlett.42.407.

[17] *An introduction to particle dark matter*. DOI: https://doi.org/10.48550/arXiv.1910.05610.

[18] R. Cowsik and J. McClelland, "An upper limit on the neutrino rest mass," *Phys. Rev. Lett.*, vol. 29, pp. 669–670, 10 1972. DOI: 10.1103/PhysRevLett.29.669. [Online]. Available: https://link.aps.org/doi/10.1103/PhysRevLett.29.669.

[19] T. Marco, B. Gianfranco, and M. Antonio, "Dark matter candidates: A ten-point test," *Journal of Cosmology and Astroparticle Physics*, vol. 2008, no. 3, p. 46, Mar. 2008. DOI: 10.1088/1475-7516/2008/03/022. [Online]. Available: https://ui.adsabs.harvard.edu/abs/2008JCAP...03..022T.

[20] J. B. et al, "Direct detection of dark matterappec committee report," *Reports on Progress in Physics*, p. 56 201, 5 May 2022. DOI: doi:10.1088/1361-6633/ac5754.

[21] T. Lin, "Dark matter models and direct detection," in *Conference: Theoretical Advanced Study Institute Summer School 2018 "Theory in an Era of Data"*, Jul. 2019, p. 009. DOI: 10.22323/1.333.0009.

[22] J. Conrad and O. Reimer, "Indirect dark matter searches in gamma and cosmic rays," *Nature Physics*, vol. 13, no. 3, pp. 224–231, 2017. DOI: 10.1038/nphys4049. [Online]. Available: https://doi.org/10.1038/nphys4049.

[23] J. Feng, "Dark matter candidates from particle physics and methods of detection," *Ann. Rev. Astron. Astrophys*, pp. 495–545, 48 May 2010. [Online]. Available: https://doi.org/10.1146/annurev-astro-082708-101659.

[24] D. H. G. Bertone and J. Silk, "Particle dark matter: Evidence, candidates and constraints," *Phys.Rept.405:279-390,2005*, vol. 405, pp. 279–390, Aug. 2005. DOI: https://doi.org/10.1016/j.physrep.2004.08.031.

[25] Y. A. Golfand and E. P. Likhtman, "Extension of the algebra of poincare group generators and violation of p invariance," *JETP Lett.*, vol. 13, pp. 323–326, 1971. DOI: 10.1142/9789814542340_0001.

[26] T. Kaluza, "Zum unitätsproblem der physik," *Sitzungsber. Preuss. Akad. Wiss. Berlin (Math. Phys.)*, vol. 1921, pp. 966–972, 1921. DOI: 10.1142/S0218271818700017.

[27] B. S. DeWitt, "Quantum theory of gravity. ii. the manifestly covariant theory," *Phys. Rev.*, vol. 162, pp. 1195–1239, 5 Oct. 1967. DOI: 10.1103/PhysRev.162.1195. [Online]. Available: https://link.aps.org/doi/10.1103/PhysRev.162.1195.

[28] C. Weinheimer, "Proceedings of 10th international workshop on neutrino telescopes," in *10th International Workshop on Neutrino Telescopes*, arXiv:hep-ex/0306057, Venice, Italy, 2003.

[29] S. F. et al., "Determination of solar neutrino oscillation parameters using 1496 days of super-kamiokande-i data," *Physics Letters B*, vol. 539, no. 3, pp. 179–187, 2002, ISSN: 0370-2693. DOI: https://doi.org/10.1016/S0370-2693(02)02090-7. [Online]. Available: https://www.sciencedirect.com/science/article/pii/S0370269302020907.

[30] O. Buchmueller, C. Doglioni, and L.-T. Wang, "Search for dark matter at colliders," *Nature Physics*, vol. 13, no. 3, pp. 217–223, 2017. DOI: 10.1038/nphys4054. [Online]. Available: https://doi.org/10.1038/nphys4054.

[31] T. A. et al., "Lhc dark matter working group: Next-generation spin-0 dark matter models," *Physics of the Dark Universe*, vol. 27, p. 100 351, 2020. DOI: https://doi.org/10.1016/j.dark.2019.100351. [Online]. Available: https://www.sciencedirect.com/science/article/pii/S221268641930161X.

[32] E. Bonamente, "Search for gamma-ray emission from dark matter annihilation in galactic satellites with fermi," Ph.D. dissertation, Università degli Studi di Perugia, Dec. 2010. DOI: 10.13140/2.1.4085.2800.

[33] R. K. Leane, "Indirect detection of dark matter in the galaxy," *arXiv: High Energy Physics - Phenomenology*, 2020. [Online]. Available: https://api.semanticscholar.org/CorpusID:219177254.

[34] M. Hütten and D. Kerszberg, "Tev dark matter searches in the extragalactic gamma-ray sky," *Galaxies*, vol. 10, no. 5, 2022. DOI: 10.3390/galaxies10050092. [Online]. Available: https://www.mdpi.com/2075-4434/10/5/92.

[35] S. Profumo, "Tasi 2012 lectures on astrophysical probes of dark matter," *arXiv: High Energy Physics - Phenomenology*, 2013. [Online]. Available: https://api.semanticscholar.org/CorpusID:119196534.

[36] M. Kuhlen, "The dark matter annihilation signal from dwarf galaxies and subhalos," *Advances in Astronomy*, vol. 2010, Jan. 2010. DOI: 10.1155/2010/162083.

[37] T. Bringmann and C. Weniger, "Gamma ray signals from dark matter: Concepts, status and prospects," *Physics of the Dark Universe*, vol. 1, no. 1, pp. 194–217, 2012. DOI: https://doi.org/10.1016/j.dark.2012.10.005. [Online]. Available: https://www.sciencedirect.com/science/article/pii/S221268641200009X.

[38] T. Sjöstrand and S. Prestel, *PYTHIA 8.3: Physics and Manual*, Available at https://pythia.org/pythia83_manual.pdf, 2015. [Online]. Available: https://arxiv.org/abs/1507.02199.

[39] e. a. Cirelli M. Corcella G., "Pppc4dmid: A poor particle physicist cookbook for dark matter indirect detection," *Journal of Cosmology and Astroparticle Physics*, p. 51, 3 Mar. 2011. DOI: doi:10.1088/1475-7516/2011/03/051.

[40] J. M. Gaskins, "A review of indirect searches for particle dark matter," *Contemp. Phys.*, vol. 57, no. 4, pp. 496–525, 2016. DOI: 10.1080/00107514.2016.1175160.

[41] F. N. e. a. Arina C. Di Mauro M., "Cosmixs: Cosmic messenger spectra for indirect dark matter searches," *Journal of Cosmology and Astroparticle Physics*, p. 35, 3 Mar. 2024. DOI: doi:10.1088/1475-7516/2024/03/035.

[42] H. J. Völk and K. Bernlöhr, "Imaging very high energy gamma-ray telescopes," *Experimental Astronomy*, vol. 25, Mar. 2009. DOI: 10.1007/s10686-009-9151-z. [Online]. Available: http://dx.doi.org/10.1007/s10686-009-9151-z.

[43] M. A. S.-C. Michele Doro and M. Hütten, "Fundamental physics searches with iacts," *Advances in Very High Energy Astrophysics, 2024*, 2022. DOI: https://doi.org/10.48550/arXiv.2111.01198.

[44] M. e. a. Doro, "Dark matter and fundamental physics with the cherenkov telescope array," *Astroparticle Physics*, vol. 43, pp. 189214, Mar. 2013. DOI: 10.1016/j.astropartphys.2012.08.002. [Online]. Available: http://dx.doi.org/10.1016/j.astropartphys.2012.08.002.

[45] V. A. et al., "Constraining dark matter lifetime with a deep gamma-ray survey of the perseus galaxy cluster with magic," *Physics of the Dark Universe*, vol. 22, pp. 38–47, 2018, ISSN: 2212-6864. DOI: https://doi.org/10.1016/j.dark.2018.08.002. [Online]. Available: https://www.sciencedirect.com/science/article/pii/S2212686418300621.

[46] G. e. a. Aad, "Observation of gauge boson joint-polarisation states in wśz production from pp collisions at <mml:math xmlns:mml="http://www.w3.org/1998/math/mathml" altimg="si1.svg"><mml:msqrt><mml:mrow><mml:mi>s</mml:mi></mml:mrow></mml:msqrt><mml:mo linebreak="goodbreak" linebreakstyle="after">=</mml:mo><mml:mn>13</mml:mn></mml:math> tev with the atlas detector," *Physics Letters B*, vol. 843, p. 137 895, Aug. 2023, ISSN: 0370-2693. DOI: 10.1016/j.physletb.2023.137895. [Online]. Available: http://dx.doi.org/10.1016/j.physletb.2023.137895.

[47] D. Giacomo, "Statistical tools for imaging atmospheric cherenkov telescopes," *Universe*, vol. 8, no. 2, 2022. DOI: 10.3390/universe8020090. [Online]. Available: https://www.mdpi.com/2218-1997/8/2/90.

[48] J. Palacio, D. Navarro-Girones, and J. Rico, "Pointing optimization for iacts on indirect dark matter searches," *Astroparticle Physics*, vol. 104, pp. 8490, Jan. 2019. DOI:

10.1016/j.astropartphys.2018.09.002. [Online]. Available: http://dx.doi.org/10.1016/j.astropartphys.2018.09.002.

[49] D. A. et. al, "Gammapy: A python package for gamma-ray astronomy," *Astronomy & Astrophysics*, vol. 678, A157, Oct. 2023. DOI: 10.1051/0004-6361/202346488. [Online]. Available: http://dx.doi.org/10.1051/0004-6361/202346488.

[50] W. A. Rolke, A. M. López, and J. Conrad, "Limits and confidence intervals in the presence of nuisance parameters," *Nuclear Instruments and Methods in Physics Research Section A: Accelerators, Spectrometers, Detectors and Associated Equipment*, vol. 551, no. 2, pp. 493–503, 2005. DOI: https://doi.org/10.1016/j.nima.2005.05.068. [Online]. Available: https://www.sciencedirect.com/science/article/pii/S016890020501291X.

[51] T. C. T. A. Consortium, : and K. A. et al., *Prospects for γ-ray observations of the perseus galaxy cluster with the cherenkov telescope array*, 2023. [Online]. Available: https://arxiv.org/abs/2309.03712.

[52] V. e. a. Acciari, "Combined searches for dark matter in dwarf spheroidal galaxies observed with the magic telescopes, including new data from coma berenices and draco," *Physics of the Dark Universe*, vol. 35, p. 100 912, Mar. 2022, ISSN: 2212-6864. DOI: 10.1016/j.dark.2021.100912. [Online]. Available: http://dx.doi.org/10.1016/j.dark.2021.100912.

[53] H. e. a. Abdallah, "Search for dark matter signals towards a selection of recently detected des dwarf galaxy satellites of the milkyăway with h.e.s.s.," *Physical Review D*, vol. 102, no. 6, Sep. 2020, ISSN: 2470-0029. DOI: 10.1103/physrevd.102.062001. [Online]. Available: http://dx.doi.org/10.1103/PhysRevD.102.062001.

[54] S. e. a. Archambault, "Dark matter constraints from a joint analysis of dwarf spheroidal galaxy observations with veritas," *Physical Review D*, vol. 95, no. 8, Apr. 2017, ISSN: 2470-0029. DOI: 10.1103/physrevd.95.082001. [Online]. Available: http://dx.doi.org/10.1103/PhysRevD.95.082001.

[55] K. I. of Technology, *Corsika: An air shower simulation program*, 2015. [Online]. Available: http://www.ikp.kit.edu/corsika/.

[56] J. Matthews, "A heitler model of extensive air showers," *Astroparticle Physics*, vol. 22, no. 5, pp. 387–397, 2005, ISSN: 0927-6505. DOI: https://doi.org/10.1016/j.astropartphys.2004.09.003. [Online]. Available: https://www.sciencedirect.com/science/article/pii/S0927650504001598.

[57] B. Rossi and K. Greisen, "Cosmic-ray theory," *Rev. Mod. Phys.*, vol. 13, pp. 240–309, 4 1941. DOI: 10.1103/RevModPhys.13.240. [Online]. Available: https://link.aps.org/doi/10.1103/RevModPhys.13.240.

[58] C. L. Sarazin, "X-ray emission from clusters of galaxies," *Reviews of Modern Physics*, vol. 58, pp. 1–115, 8 Jan. 1986. DOI: 10.1103/RevModPhys.58.1.

[59] B. Gianfranco, *Particle Dark Matter: Observations, Models and Searches*. Cambridge University Press, 2010, ISBN: 9780521763684. DOI: 10.1017/CBO9780511770739. [Online]. Available: https://www.cambridge.org/core/product/B03C934EAB188884EFC6B02432632496.

[60] S. Funk, "Indirect detection of dark matter with γ rays," *Proceedings of the National Academy of Sciences*, vol. 112, pp. 12264 –12 271, 2013. [Online]. Available: https://api.semanticscholar.org/CorpusID:5729051.

[61] R. Workman and others (Particle Data Group), "Review of particle physics: Dark matter," *Prog. Theor. Exp. Phys.*, vol. 2022, p. 083C01, 2023. DOI: 10.1093/ptep/ptac097. [Online]. Available: https://pdg.lbl.gov/2023/reviews/rpp2022-rev-dark-matter.pdf.

[62] R. A. B. et al., "Eucapt white paper: Opportunities and challenges for theoretical astroparticle physics in the next decade," *arXiv: High Energy Astrophysical Phenomena*, 2021. [Online]. Available: https://api.semanticscholar.org/CorpusID:239024557.

[63] T. C. Weekes, "Very high energy gamma-ray astronomy," *Physics Reports*, vol. 160, no. 1, pp. 1–121, 1988. DOI: https://doi.org/10.1016/0370-1573(88)90177-9. [Online]. Available: https://www.sciencedirect.com/science/article/pii/0370157388901779.

[64] M. de Naurois and D. Mazin, "Ground-based detectors in very-high-energy gamma-ray astronomy," *Comptes Rendus Physique*, vol. 16, no. 6, pp. 610–627, 2015. DOI: https://doi.org/10.1016/j.crhy.2015.08.011. [Online]. Available: https://www.sciencedirect.com/science/article/pii/S1631070515001462.

[65] M. Doro, "Novel Reflective Elements and Indirect Dark Matter Searches for MAGIC II and Future IACTs.," Ph.D. dissertation, Padua U., 2009.

[66] J. Hinton, "Ground-based gamma-ray astronomy with cherenkov telescopes," *New Journal of Physics*, vol. 11, no. 5, p. 055 005, May 2009. DOI: 10.1088/1367-2630/11/5/055005. [Online]. Available: https://dx.doi.org/10.1088/1367-2630/11/5/055005.

[67] W. A. Rolke and A. M. López, "Confidence intervals and upper bounds for small signals in the presence of background noise," *Nuclear Instruments and Methods in Physics Research Section A: Accelerators, Spectrometers, Detectors and Associated Equipment*, vol. 458, no. 3, pp. 745–758, 2001. DOI: https://doi.org/10.1016/S0168-9002(00)00935-9. [Online]. Available: https://www.sciencedirect.com/science/article/pii/S0168900200009359.

[68] L. Bergström, "Dark matter evidence, particle physics candidates and detection methods," *Annalen der Physik*, vol. 524, no. 9-10, pp. 479–496, 2012. DOI: https://doi.org/10.1002/andp.201200116. [Online]. Available: https://onlinelibrary.wiley.com/doi/abs/10.1002/andp.201200116.

[69] T. R. Slatyer, "Indirect detection of dark matter," in *Theoretical Advanced Study Institute in Elementary Particle Physics: Anticipating the Next Discoveries in Particle Physics*, 2018, pp. 297–353. DOI: 10.1142/9789813233348_0005.

[70] e. a. Cherenkov Telescope Array Consortium: B.S. Acharya, *Science with the Cherenkov Telescope Array*. WORLD SCIENTIFIC, Feb. 2018, ISBN: 9789813270091. DOI: 10.1142/10986. [Online]. Available: http://dx.doi.org/10.1142/10986.

[71] C. Fruck, "The galactic center resolved with magic and a new technique for atmospheric calibration," Ph.D. dissertation, Max-Planck-Institut für Physik (Werner-Heisenberg-Institut), 2015. [Online]. Available: https://api.semanticscholar.org/CorpusID:125111425.

[72] V. Scapin, "Observations of gamma-ray burst afterglows with the magic telescope," Ph.D. dissertation, Udine U., 2010.

[73] P. Dario Serpico and D. Hooper, "Gamma rays from dark matter annihilation in the central region of the galaxy," *New Journal of Physics*, vol. 11, no. 10, p. 105 010, Oct. 2009, ISSN: 1367-2630. DOI: 10.1088/1367-2630/11/10/105010. [Online]. Available: http://dx.doi.org/10.1088/1367-2630/11/10/105010.

[74] H. e. a. Abdalla, "Search for dark matter annihilation signals in the h.e.s.s. inner galaxy survey," *Physical Review Letters*, vol. 129, no. 11, Sep. 2022, ISSN: 1079-7114. DOI: 10.1103/physrevlett.129.111101. [Online]. Available: http://dx.doi.org/10.1103/PhysRevLett.129.111101.

List of Figures

List of Tables